Vortex Formation and Decay:
The Scaling of Vortex-Wall Interaction

Zur Erlangung des akademischen Grades eines
Doktors der Ingenieurwissenschaften (Dr.-Ing.)
von der KIT-Fakultät für Maschinenbau des
Karlsruher Instituts für Technologie (KIT)

angenommene
Dissertation
von

M.Sc. Frieder Kaiser

Abstract

The present work aims to characterise the influence of turbulence and in particular the influence of the Reynolds number (Re) on the dynamic processes of vortex formation and decay. Inspired by vortex wakes in bio-propulsion, three characteristic features of vortex formation and decay are identified, each resulting from the interaction of a vortex with a solid structure (e.g. a propulsor): a curved free shear layer, the vortex core and a boundary layer between vortex and propulsor. Multiple studies are presented that isolate the characteristic flow features in simplified configurations and study the influence of turbulence on vortex evolution. In the first study, the interaction of a generic vortex with a wall is investigated by impulsively-stopping the walls of a rotating cylinder containing a fluid in solid-body rotation (SBR). The decay of the initial SBR is characterised by means of direct numerical simulations (DNS) in a limited Re range ($Re \leq 2.8 \cdot 10^4$). Based on the underlying flow structures, five stages of the decay process are identified. The evaluation of the DNS results provides empirical scaling laws for various stages of the decay, which are subsequently validated in two experimental campaigns covering the moderate Re range ($Re \leq 5.6 \cdot 10^5$) and the high Re range ($Re \leq 4 \cdot 10^6$), respectively. Here, the spin-down from SBR is captured by means of particle-image velocimetry (PIV). Furthermore, the free shear layer and the vortex core are investigated in the wake of accelerated low-aspect ratio propulsors. In PIV experiments, performed in a large towing-tank facility, a wide range of Re is investigated. In addition, the turbulent structures in the wake are modified through bio-inspired undulations at the circumferential edge of the propulsor. The introduction of turbulent structures larger than the thickness of the free shear layer is shown to influence the vortex growth and thus the propulsion force.

Kurzfassung

Das Ziel der vorliegenden Arbeit ist es den Einfluss von Turbulenz und im speziellen der Reynoldszahl (*Re*) auf die Prozesse der Wirbelformation und des Wirbelzerfalls zu untersuchen. Inspiriert von Wirbeln, die bei der Fortbewegung von schwimmenden und fliegenden Tieren auftreten, werden drei charakteristische Merkmale identifiziert, die durch das Zusammenspiel eines Wirbels mit einem beschleunigten Festkörper (z.B. einem Flügel oder einer Flosse) entstehen: eine gekrümmte freie Scherschicht, der Wirbelkern und die Grenzschicht zwischen dem Wirbel und dem beschleunigten Körper. Im Rahmen der Arbeit werden mehrere Experimente und Simulationen vorgestellt, welche diese Merkmale der Wirbel in vereinfachten Konfigurationen reproduzieren und von anderen Effekten isolieren. Dies ermöglicht es den Einfluss der Turbulenz auf besagte Wirbelmerkmale zu quantifizieren. Zunächst wird die Interaktion eines generischen Wirbels mit einer Wand betrachtet. Hierzu wird ein Zylinder, welcher ein Fluid in Starrkörperrotation enthält, schlagartig angehalten. Das Abklingen und der Zerfall der des Starrkörperwirbels wird mithilfe einer direkten numerischen Simulation (DNS) für Reynoldszahlen im Bereich $Re \leq 2.8 \cdot 10^4$ analysiert. Fünf Stufen des Wirbelzerfalls können aufgrund der zugrundeliegenden Strukturen der Strömung charakterisiert werden. Darüber hinaus liefern die Ergebnisse der DNS empirische Skalierungsgesetze, die verschiedene Stufen den Wirbelzerfalls beschreiben. Die Skalierungsgesetze werden anschließend anhand von zwei experimentellen Kampagnen im moderaten ($Re \leq 5.6 \cdot 10^5$) und hohen ($Re \leq 4 \cdot 10^6$) Reynoldszahlbereich validiert. Anschließend wird die gekrümmte Scherschicht und der Wirbelkern genauer betrachtet. In Experimenten in einem großskaligen Schleppkanal wird eine runde Platte aus der Ruhe beschleunigt. Hier-

bei liefern Experimente in einem großen Reynoldszahlbereich Erkenntnisse über die Auswirkungen von kleinskaligen Strukturen auf die Wirbelformation. Weiterhin wird die Turbulenz im Wirbel durch Modifikationen der umlaufenden Plattenkante beeinflusst. Inspiriert von in der Natur auftretenden Flossenformen werden wellenartige Strukturen aufgeprägt, welche Strukturen im Bereich ihrer eigenen Wellenlänge in die Strömung einbringen. Sind diese Wellenlängen größer als die Dicke der gekrümmten Scherschicht, wird das Wirbelwachstum beeinflusst und damit die Kraft, die auf die Platte wirkt, modifiziert.

Table of Contents

1 Introduction

Vortical structures are ubiquitous in nature as well as in engineering applications. On the one hand, the effects of vortices are sometimes unwanted or even dangerous. Popular examples include vortex shedding off buildings, buffeting in transonic flow, tip vortices off of wings, and extreme weather phenomena such as hurricanes. On the other hand, however, the material and momentum transport of vortical structures can also be fundamental for the working principle of a functional engineering system. Technical applications utilise vortical structures in: swirl cooling systems; mixing devices; process engineering and biotechnology; tank draining; and engine injection, to name but a few. In nature, vortices might play an even more significant role. Both, the atmosphere as well as the ocean (in particular the global conveyor belt) are dominated by vortices, which eventually determine the climate we are living in. Another – if not the most prominent – example of vortices found in nature is associated with animal locomotion. A large variety of swimmers and flyers utilises vortices to produce their lift and thrust.

The present work addresses the above phenomena by means of investigations into the physics of vortex formation and decay. Hereby, the locomotion of swimmers and flyers is selected as the guiding example. Note, however, that due to the high degree of abstraction, many of the fundamental results presented in this thesis apply for a wide variety of vortical structures, such as among others, the above-mentioned examples.

(a) Roll-up of shear layer   (b) Formation of LEV   (c) Detachment of LEV
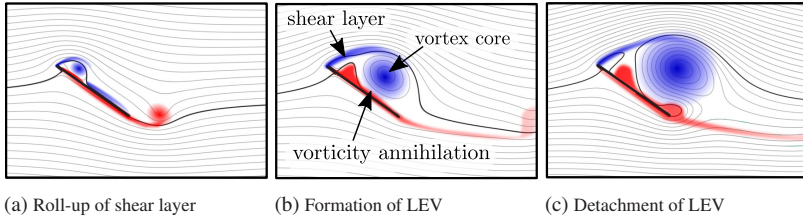
Figure 1.1: Formation and detachment of a two-dimensional leading-edge vortex (LEV). Blue and red contours show positive and negative vorticity, respectively. Streamlines adapted from Eldredge & Jones [25].

1.1 Motivation

A sudden change of the angle of attack over a propulsor (e.g. wings or flippers) leads to dynamic flow separation. A free shear layer is formed that subsequently rolls up into a vortex. The interaction of the pressure minimum in the vortex with the propulsor itself produces thrust and/or lift while maintaining a high degree of manoeuvrability. As an example, figure 1.1 presents the formation of a leading-edge vortex (LEV) in a quasi two-dimensional flow. Once the propulsor accelerates, a free shear layer is formed, rolls up and results in an LEV (figure 1.1a), which then grows (figure 1.1b) and eventually detaches (figure 1.1c). Pitt Ford and Babinsky [105] point out that most of the bound circulation of the propulsor is contained in the LEV and thus its influence on lift and thrust is maintained while the vortex remains attached to the propulsor. As such, vortex stability and the evolution of circulation are crucial to assess the forces acting on propulsors. The influencing factors on stability and circulation have been extensively addressed in recent research. Often inspired by observations on the shape and kinematics of animal propulsors, a large variety of influencing factors have been investigated. For example, swept wings [141] and spanwise wing curvature [48, 127] were found to influence the three-dimensional vortex structure. Concerning the kinematics, the reduced frequency of pitching [40], the wake mechanics [129, 131] and the influence

of rotational accelerations was investigated [70]. Chin & Lentink [18] provide a comprehensive overview of the evolutionary convergence of propulsor kinematics. Interestingly, similar kinematics are observable in a wide range of Reynolds numbers (*Re*) reaching from small insects to large mammals: Both the wake kinematics (described by the Strouhal number, *St*) as well as the influence of rotational accelerations (described by the Rossby number, *Ro*) remain in a small range ($Ro < 4$ [70] and $0.2 < St < 0.4$ [129, 131]).

While *St* and *Ro* influence the three-dimensional vortex structure on a macro scale, *Re* scaling comes along with a varying range of flow structure sizes in a turbulent flow. At first glance, the wide range of *Re*, at which vortices are formed in nature, suggests an insensitivity of vortical flows towards turbulence. However, as a vortex in bio-propulsion is a separated flow with shear and boundary layers, the influence of turbulence on vortex driven locomotion is apparent and remains yet to be fully understood. A very limited amount of studies focusses on the interplay of vortical structures with turbulence as the three-dimensional and unsteady flow during vortex formation makes an quantitative assessment of turbulence an extremely challenging endeavour. The present thesis aims to close this gap in the literature.

1.2 Objectives and Procedure

The major objective of the present thesis is to explore the influence of turbulence on vortex formation and vortex stability. In particular, the influence of turbulence on the mass, momentum and circulation budget of a generic vortex are of interest. The main challenge of these investigations into the impact of turbulence on vortex formation is to derive a deeper understanding of the interplay between a unsteady and three-dimensional large-scale vortical structures and local small-scale effects due to turbulence.

The investigation of such a complex problem is tackled through identification and subsequent isolation of varying aspects of the vortex by designing suitable
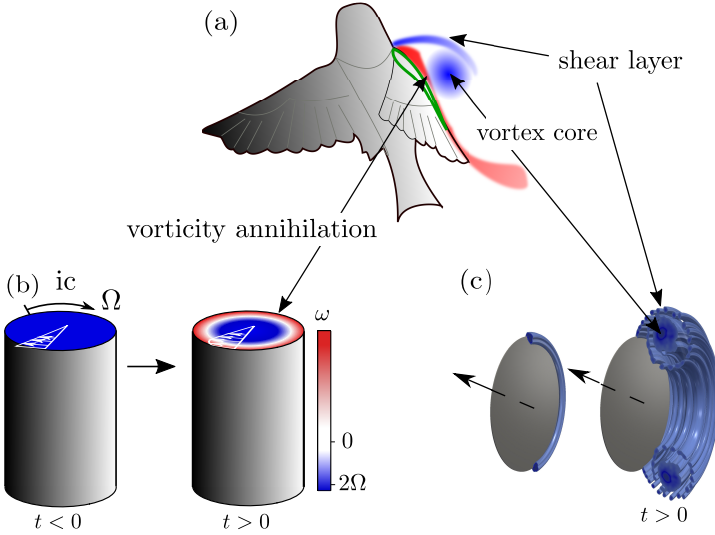
Figure 1.2: (a) Drawing of a LEV on a bird's wing. (b) Schematic describing the vorticity distribution (colour coded) and azimuthal velocity profile (vectors) before (initial condition (ic)) and after the start of the decay of a vortex in solid-body rotation. (c) Shear layer and vortex core during vortex formation in the wake of a circular plate.

experiments, which focus on a detailed analysis of the respective feature. In particular, the present manuscript focuses on three aspects of vortex-driven locomotion highlighted in figure 1.2(a), where turbulence and its scaling modify the flow through:

- the vorticity-annihilating boundary layer between the vortex and the suction side of the propulsor;
- the free shear layer, which rolls up into the vortex; and
- the vortex core and its pressure minimum.

The first flow investigated in this manuscript focuses on the *Re* scaling of the suction-side boundary layer, which is unique in the sense that the vorticity inside the vortex interacts with opposite-signed vorticity of the boundary layer. Thus, boundary-layer growth is basically a cross-annihilation process between

the vorticity in the vortex itself and the opposite-signed vorticity of the boundary layer. Eslam Panah *et al.* [26] and Akkala & Buchholz [1] investigated the role of the suction-side boundary layer on the circulation budget of an LEV and found that the cross-annihilated vorticity compensates for up to 50% of the vorticity fed into the vortex through the shear layer. As such, this process strongly influences the evolution of circulation and thus affects both the forces as well as vortex stability.

To allow for statistical analysis of this dynamic and transitional problem, a relatively simple experiment has been conceived, which quantifies the influence of the cross-annihilating vorticity on the boundary-layer formation.

An infinitely long vortex in solid body rotation (SBR), with angular speed Ω and radius R, is placed inside a cylinder that is impulsively stopped at $t = 0$ (see figure 1.2b). Eventually, all vorticity inside the SBR is annihilated by the opposite-signed vorticity of the boundary layer and the flow becomes quiescent. However, during its spin-down to rest the flow undergoes multiple transitions to various flow stages. Each of the stages contains flow features that result from the interaction of opposite-signed vorticity. In order to explore these phenomena, the flow is first analysed in detail by means of direct numerical simulations. The well-resolved data allow elaborate statistical evaluation in a moderate range of *Re*; see chapter 3. Subsequently, in chapter 4 the *Re* scaling for very high-*Re* is investigated by means of particle image velocimetry (PIV) measurements at the large-scale CORIOLIS II experimental platform in Grenoble, France.

The second flow condition investigated in the present thesis is designed in order to further study the impact of turbulence on the separated shear layer, the vortex core and vortex stability. Therefore, a simplified propulsor of circular shape is accelerated perpendicular to its orientation (see figure 1.2c and chapter 5), where the influence of small-scale structures in the shear layer is assessed by conducting experiments over a wide range of *Re*. Additional three-dimensionality of the flow is enforced by modifying the circumferential

edge of the propulsor with undulations of various wavelengths. The impact of *Re* and the edge undulations is addressed by means of PIV and force measurements at Queen's University in Kingston, Canada.

The present thesis contains results which were previously published by the author in [Kaiser et al., 2020a] and [Kaiser et al., 2020b]. All quotations from those publications are highlighted.

2   Fundamentals

In the present chapter an overview of the theoretical background for the following studies is provided. First, the fundamental equations of hydrodynamics are outlined in § 2.1. Subsequently, the properties of vortices are discussed and methods for their identification are provided in § 2.2. Eventually, as various instabilities occur during vortex formation and decay, an overview of the most important instability mechanisms is provided in § 2.3.1 (centrifugal instabilities) and § 2.3.2 (Kelvin-Helmholtz instabilities).

2.1   Governing equations of hydrodynamics

The fundamental equations utilised throughout this work are based on multiple assumptions [4, 125]. In particular, the fluid is described as a incompressible Newtonian continuum. First of all, the continuum hypothesis implies that the fluid volume under consideration consists of an infinite number of infinitesimally small fluid elements and that thereby all quantities inside the fluid are a continuous function in time and space. The fluid is further considered to be Newtonian. As such, all viscous stresses relate linearly to the rate-of-strain (cf. § 2.1.2) by a constant factor μ, called the dynamic viscosity. Finally, the fluid is assumed to be incompressible. In contrast to aerodynamics and thermodynamics where compressibility effects are significant, the field of hydrodynamics covers flows where the material derivative of the density ρ vanishes such that

$$\frac{\mathrm{D}\rho}{\mathrm{D}t} = \frac{\partial \rho}{\partial t} + u \cdot \nabla \rho = 0 \,. \tag{2.1}$$

Equation (2.1) implies that a fluid element convecting with velocity u conserves its density at all times t. The present chapter details the fundamental equations of hydrodynamics.

2.1.1 Conservation of mass and momentum

Utilising the assumptions outlined above, the motion of a fluid can be described by the incompressible continuity equation

$$\nabla \cdot u = 0, \tag{2.2}$$

and the incompressible Navier-Stokes equation as

$$\rho \underbrace{\left[\frac{\partial u}{\partial t} + (u \cdot \nabla)u \right]}_{\text{I}} = - \underbrace{\nabla p}_{\text{II}} + \underbrace{\mu \nabla^2 u}_{\text{III}} + \underbrace{\rho G}_{\text{IV}}, \tag{2.3}$$

where I is the material derivative consisting of the temporal velocity change $\frac{\partial u}{\partial t}$ and the convection $(u \cdot \nabla)u$, II is the gradient of the pressure p, III are the viscous forces acting in the Newtonian fluid and IV is a body force G (e.g. gravity).

To generalise findings and to transfer insights into physics between different flows, the equations are often written in their dimensionless representation. As a first step dimensionless quantities are defined

$$u_i^* = \frac{u_i}{U_0}; \quad t^* = t/T_0; \quad x_i^* = \frac{x_i}{L_0}; \quad p^* = \frac{p - P_\infty}{P_0 - P_\infty}; \quad G^* = \frac{G}{g} \tag{2.4}$$

utilising the scaling parameters U_0, L_0, T_0, $P_0 - P_\infty$ (reference pressure difference) and g. The index i denotes the respective direction in the chosen coordinate system.

The dimensionless quantities of (2.4) are inserted into (2.2) and (2.3), leading to the dimensionless continuity equation

$$\nabla^* \cdot u^* = 0 \tag{2.5}$$

and the dimensionless Navier-Stokes equation

$$\frac{\rho U_0}{T_0}\frac{\partial u^*}{\partial t^*} + \frac{\rho U_0^2}{L_0}(u^* \cdot \nabla^*)u^* = \frac{P_0 - P_\infty}{L_0}\nabla^* p^* + \rho g G^* + \frac{\mu U_0}{L_0^2}\nabla^{*2}u^*. \tag{2.6}$$

Equation (2.6) multiplied by the constant $L_0/(\rho U_0^2)$ results in

$$\frac{L_0}{T_0 U_0}\frac{\partial u^*}{\partial t^*} + (u^* \cdot \nabla^*)u^* = \frac{P_0 - P_\infty}{\rho U_0^2}\nabla^* p^* + \frac{g L_0}{U_0^2}G^* + \frac{\nu}{U_0 L_0}\nabla^{*2}u^*, \tag{2.7}$$

where $\nabla^* = L_0\nabla$ and $\nu = \mu/\rho$ is the kinematic viscosity. Note that the scaling parameters U_0, L_0, T_0, $P_0 - P_\infty$ and g can be defined to be characteristic quantities of the flow under consideration. Thereby, the dimensionless parameters occurring before the distinct terms of the normalised Navier-Stokes equation (2.7) provide an estimate of the magnitude of the terms, which they multiply. The Strouhal number ($St = L_0/(T_0 U_0)$) describes the temporal dynamics of the system and scales inverse to the time scale T_0. Furthermore, the Froude number $Fr = U_0^2/(g L_0)$ is an estimate of the ratio between inertial and body forces (relevant in chapter 4) while the Euler number ($Eu = (P_0 - P_\infty)/(\rho U_0^2)$) provides the ratio between the influence of pressure and inertial forces. Finally, the viscous term is scaled by $1/Re$, where

$$Re = \frac{U_0 L_0}{\nu} \tag{2.8}$$

is the Reynolds number that represents the ratio between inertial and viscous forces. Generally speaking high Re implicate a higher probability for a flow to transition to turbulence, and in the case that turbulence is established, a higher ratio between the size of the largest and the smallest structures in the flow.

The spin-down problem in an infinite cylinder (chapter 3) of radius R and initial angular velocity Ω only has a very limited amount of characteristic physical quantities influencing the problem. The simplicity of the geometry and the kinematics allows for a normalisation with a reduced number of scaling parameters, such as

$$u_i^* = \frac{u_i}{\Omega R}; \quad x_i^* = \frac{x_i}{R}; \quad t^* = \Omega t; \quad p^* = \frac{p}{\rho \Omega^2 R^2} \, . \tag{2.9}$$

If the influence of gravity is neglected, the dimensionless Navier-Stokes equation simplifies to

$$\frac{\partial u^*}{\partial t^*} + (u^* \cdot \nabla^*) u^* = -\nabla^* p^* + \frac{\nu}{\Omega R^2} (\nabla^*)^2 u^* , \tag{2.10}$$

with the Reynolds number $Re = \Omega R^2 / \nu$ and $St = Eu = 1$.

In the present thesis, the Navier-Stokes equation is often used in a cylindrical coordinate system. Appendix A.1 provides the detailed equations.

2.1.2 Vorticity equation and circulation

The velocity gradient tensor ∇u can be divided into an symmetric and antisymmetric contribution

$$\nabla u = E + \Omega_R = \frac{1}{2} \left[(\nabla u) + (\nabla u)^{\mathrm{T}} \right] + \frac{1}{2} \left[(\nabla u) - (\nabla u)^{\mathrm{T}} \right] . \tag{2.11}$$

The symmetric contribution E (rate-of-strain tensor) describes the speed of local deformation and is coupled with the viscous stresses in the fluid. In contrast, the antisymmetric part Ω_R (spin tensor) only provides information about the local rigid body rotation of the fluid element. Hereby, the elements

in the upper triangular of the spin tensor Ω_R are equivalent to the elements of the vorticity vector

$$\omega = \nabla \times u. \tag{2.12}$$

The viscous term III in (2.3) can be rewritten by means of a vector identity

$$\mu \nabla^2 u = \mu \left(\underbrace{\nabla \cdot u}_{=0\,;\,\text{see eq. 2.2}} - \nabla \times \underbrace{(\nabla \times u)}_{\omega} \right). \tag{2.13}$$

Equation (2.13) implies that if the vorticity is zero or homogeneous the fluid can be considered to be frictionless. As such, the transport of vorticity is of interest. A transport equation for ω can be derived by taking the curl of the Navier-Stokes equation (2.3) such that:

$$\underbrace{\frac{\partial \omega}{\partial t}}_{I} + \underbrace{(u \cdot \nabla)\omega}_{II} = \underbrace{(\omega \cdot \nabla)u}_{III} + \underbrace{\nu \nabla^2 \omega}_{IV}. \tag{2.14}$$

Conservative body forces G are assumed. The detailed derivation of (2.14) is given in A.4. Terms I, II, and IV are similar to the terms in the Navier-Stokes equation (2.3). The additional term III describes the amplification of vorticity due to stretching and/or reorientation. The continuum equation and the Navier-Stokes equation suffice to find a solution for any incompressible flow. Therefore, a solution of the vorticity equation is not required. However, according to Morton [94], the equation has interesting properties that provide additional possibilities to interpret the underlying physics of the flow in question.

1. The pressure term as well as the body forces are eliminated. Therefore, the propagation of vorticity in the inner flow (away from the boundaries), does not (directly) depend on the pressure nor conservative body forces.

2. There is no source term in the vorticity equation. Thus, in a homogeneous fluid with no (or only conservative) body forces the generation of vorticity is limited to the boundaries of the flow. The only possibility for vorticity to decay is through cross-annihilation (or cross-diffusion) with opposite-signed vorticity.

3. The production of vorticity at the boundaries can either result from a boundary acceleration [4] or from tangential pressure gradients [73].

4. The generation of vorticity is instantaneous and inviscid. It does not depend on the prior existence of vorticity in the flow. While wall shear stress indicates the presence of vorticity it does not directly imply its generation.

The accumulated vorticity normal to closed surface S is defined as the circulation

$$\Gamma = \iint_S \omega \cdot \mathrm{d}A = \oint u \cdot \mathrm{d}l, \qquad (2.15)$$

which by means of Stokes' theorem can also be computed by a line integral of the velocity along a closed curve around S. This implies, that through integrating (2.14) over a closed surface S, the budget of circulation Γ can be computed.

2.2 Vortices and their identification

Various definitions of a vortex exist. However, none of them are particularly conclusive nor satisfactory. Green [42] labels the term vortex as *fuzzy*, which is an accurate description, as attempts of definitions in literature [2, 10, 145] can be easily refuted by simple examples [42]. Green suggests a general and quite subjective definition, where he defines a vortex as a flow structure that "a majority of fluid dynamicists would label as such" [42]. However, the subjective definition is not particularly applicable for objective data evaluation. Despite their limitations, multiple criteria in the literature have proven to be useful in studies on vortex dynamics. Therefore, after a brief review of the Eulerian and

Lagrangian frames of reference in § 2.2.1, selected Eulerian methods (§ 2.2.2) and a Lagrangian method (§ 2.2.3) are outlined in the present section and later applied throughout the manuscript.

2.2.1 Eulerian versus Lagrangian frames of reference

The position of a moving particle in a fluid or solid can be described by the vector

$$x = x(b,t),\qquad(2.16)$$

where b is a reference vector and t is the instance in time. Often the position x_0 of the particle at a time t_0 is chosen as the reference vector

$$b = x_0.\qquad(2.17)$$

The Lagrangian perspective is most commonly applied in solid mechanics, where the deformation is often small, and the strain and stress are coupled by a Young's modulus [7]. In fluid mechanics, historically the Eulerian frame of reference is preferred. Modification of (2.16) implies that every reference vector can be described by a position x and a time t such that

$$b = b(x,t).\qquad(2.18)$$

The combination of (2.18) and the Lagrangian description of the velocity $u = u(b,t)$ leads to the Eulerian description where

$$u = u(b(x,t),t) = u(x,t),\qquad(2.19)$$

that provides the temporal development of a quantity (such as u) at a fixed location x. The Eulerian frame of reference is well suited for the description of most fluids, as stress is only coupled to the strain rate (by the viscosity μ) and not to the local strain. Thus, only the local velocity gradients and not

13

the deformation of the fluid volume are of interest. However, in contrast to the Lagrangian frame of reference, the Eulerian description does not directly provide the information of material transport. Therefore, in addition to the classical Eulerian flow description, wich are often based on the velocity gradient tensor (see § 2.2.2), several studies proposed Lagrangian methods [47], where the relation of material transports of neighboured particles are utilised to identify regions of coherent movement. The regions of coherent movement often are vortical structures.

2.2.2 Eulerian vortex identification

Jeong & Hussain [57] review and compare the most common Eulerian methods, which are based on the velocity gradient tensor: the Δ-criterion [19], the Q-criterion [55] and the λ_2-criterion [57]. As all criteria show similar results for the detection of a vortex in the present manuscript, the Q-criterion is chosen. The Q-criterion is easy to implement and provides a straight-forward interpretation of its value as it compares the magnitude of the rate-of-strain tensor E to the magnitude of the spin tensor Ω_R (2.11). Hunt *et al.* [55] define the second invariant of ∇u as Q, which provides

$$Q = \frac{1}{2} \left(||\Omega_R||^2 - ||E||^2 \right) , \qquad (2.20)$$

where $||\Omega_R||$ is the trace of $\Omega_R \Omega_R^{\mathrm{T}}$. If $Q > 0$, the rotation of the fluid element dominates over its stretching. Therefore, while still being an arbitrary threshold, $Q = 0$ at least provides a physical interpretation why it could be regarded as an instantaneous border of a vortex. The local maximum of Q, where $||\Omega_R|| \gg ||E||$ is defined as the vortex core.

As the criterion is evaluated locally and is gradient-based, it is highly sensitive towards local fluctuations due to small-scale turbulence and/or measurement errors. The Γ_1 and Γ_2 criteria introduced by Graftieaux [39] are similar yet more robust methods than the Q-criterion to identify the core and the bound-

aries of a vortex, respectively. For the non-Galilean invariant $\Gamma_1(x_c)$ at a location x_c is defined as

$$\Gamma_1(x_c,t) = \frac{1}{A_g} \int_{x_m \in A_g} \frac{[(x_m - x_c) \times u(x_m,t)] \cdot n}{||x_m - x_c|| \cdot ||u(x_m,t)||} \mathrm{d}A, \qquad (2.21)$$

where A_g is the surface of which the Γ_1 is evaluated, n is the normal to the surface of evaluation. The magnitude $|\Gamma_1|$ is bound by 1 and its local maximum provides an estimate of the vortex centre, which (due to the integration over A) is more robust towards local fluctuations and/or measurement errors. In contrast to Γ_1, Γ_2 is indeed Galilean invariant by accounting for the convection velocity $u(x_c,t)$, which leads to

$$\Gamma_2(x_c,t) = \frac{1}{A_g} \int_{x_m \in A_g} \frac{[(x_m - x_c) \times (u(x_m,t) - u(x_c,t))] \cdot n}{||x_m - x_c|| \cdot ||u(x_m,t) - u(x_c,t)||} \mathrm{d}A. \qquad (2.22)$$

For small A_g it can be shown that $\Gamma_2 > 2/\pi$ corresponds to $Q > 0$ and thus a dominant influence of rotation over shear [39]. As such $\Gamma_2 = 2/\pi$ provides a vortex boundary, which is similar to the vortex boundary from the Q-criterion. However, Γ_2 is more robust, as the integration over A_g limits the influence of local fluctuations.

2.2.3 Lagrangian vortex identification

"The identification of Lagrangian coherent structures (LCS) can provide deeper insight into the material transport of complex flows [47]. LCS separate flow regions of coherent movement. A classical method to calculate attracting LCS is the backward finite-time Lyapunov exponent (FTLE) $\sigma_{T_{int}}^b(t)$, which determines the local attraction rate of particle tracks over a finite time span. The first step to determine the backward FTLE is seeding massless tracers in the computational domain and tracking them backward in time over the timespan T_{int}. In the present work, flow-map interpolation, as suggested by Brunton &

Rowley [13], is applied to reduce the computational effort. The resulting flow map $\Psi_t^{t-T_{int}}$ is used to determine the right Cauchy-Green tensor

$$C = (\nabla \Psi_t^{t-T_{int}})^{\mathrm{T}} \nabla \Psi_t^{t-T_{int}}. \tag{2.23}$$

The terms of the deformation gradient $\nabla \Psi_t^{t-T_{int}}$ are obtained by the numerical schemes described in § 3.1. By evaluating and normalising the maximum eigenvalue $\Lambda_{\max}(C)$, the backward FTLE

$$\sigma_{T_{int}}^b(t) = \frac{1}{T_{int}} \ln(\Lambda_{max}(C)) \tag{2.24}$$

is determined. Shadden *et al.* [122] define thin ridges of the FTLE as LCS. For the present flow [see chapter 3], the FTLE provides a clear visualisation of the complex three-dimensional interface between the boundary layer and the vortex core. The FTLE is particularly useful during the onset of three-dimensionality in the flow, as it captures the location and evolution of the secondary instability through an alternative visualisation of the flow field." [Kaiser et al., 2020a]

2.3 Important instability mechanisms of vortical flows

2.3.1 Centrifugal instabilities

Centrifugal instabilities are observable in various flows. Examples include the flow over curved walls, parallel shear flows in a rotating frame of reference, and the vortex-wall interaction in vortices on the suction side of propulsors [14]. As a result of centrifugal instabilities, elongated vortices in the streamwise direction are formed, which often act as the nucleus of transition to turbulence. Rayleigh [107] provides a criterion for the appearance of centrifugal instabilities in axisymmetric two-dimensional flows. The equilibrium between

centrifugal forces and the pressure is unstable, if the magnitude of the circulation ($|\Gamma(r)|$) does decrease with increasing radius r such that

$$\frac{\partial |\Gamma(r)|}{\partial r} < 0. \tag{2.25}$$

This implies that a change of sign of the vorticity leads to an unstable flow. Kloosterziel & van Heijst [65] extended the criterion to axisymmetric flows in rotating frames of references and Bayly [5] found a general criterion for non-symmetric flows in inertial systems. Eventually, Sipp & Jacquin [124] formulated a general criterion for centrifugal instabilities along a two-dimensional streamline, allowing a non-axisymmetric flow as well as a rotating frame of reference. A streamline is considered as unstable when at each point

$$2\left(\frac{|u|}{\mathscr{R}} + \Omega_C\right)(\omega + 2\Omega_C) < 0 \tag{2.26}$$

is fulfilled, where $|u|$ is the magnitude of the velocity, $\mathscr{R} = |u|^3/((\nabla\Psi) \cdot [u \cdot \nabla u])$ is the local curvature of the streamline, Ψ is the streamfunction and Ω_C is the angular velocity of the coordinate system.

Buchner *et al.* [14] applied the criterion of Sipp & Jacquin [124] to the vortex formation on a pitching propulsor and identified regions affected by centrifugal instabilities. The unstable regions spatially correlate with the interface between the vorticity in the vortex and the opposite-signed vorticity contained in or advected from the boundary layer (see figure 1.1). The interface between the opposite-signed vortical layers and its scaling with *Re* is analysed in detail in chapters 3 and 4. As mentioned in chapter 1, the problem is simplified to allow statistical analysis of the eventual turbulent flow. The interface of opposite-signed vorticity is analysed during the spin-down process of a vortex in SBR that interacts with the walls of a resting cylinder; see figure 2.1. This vortex decay is enclosed by a curved boundary layer with a temporally growing boundary-layer thickness δ. A broad body of literature deals with
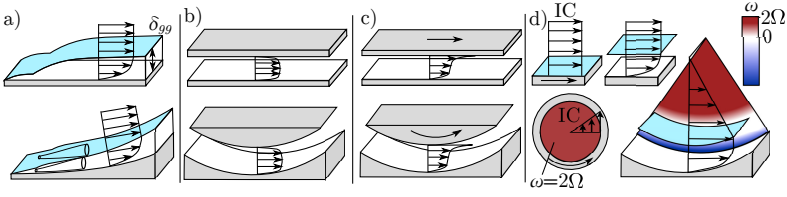
Figure 2.1: Overview of distinct boundary-layer types and their concave counterpart: (a) spatially developing boundary layers (b) fully developed channel flow (c) Couette and Taylor-Couette flow (d) temporally-developing boundary layers, with the respective initial condition (ic). Figure adapted from [Kaiser et al., 2020a].

the effects of wall curvature in various flow scenarios. The spin-down process addressed in the present manuscript (chapters 3 and 4) embodies aspects of those curved-wall flows. As such, a brief review on concave boundary layers is adapted from [Kaiser et al., 2020a] and provided in the following.

"By identifying the inviscid centrifugal instability mechanism Rayleigh [107] paved the way for research on the influence of curvature on wall-bounded flows. Subsequently, canonical flows with flat boundaries in the streamwise direction w were also assessed in their respective curved counterpart (figure 2.1). Examples include the spatially developing boundary layer (figure 2.1(a), statistically steady, no streamwise pressure gradient $\frac{\partial p}{\partial w} = 0$, spatially developing boundary-layer thickness $\frac{\partial \delta}{\partial w} \neq 0$), the fully developed channel flow (figure 2.1(b), statistically steady, $\frac{\partial p}{\partial w} \neq 0$, $\frac{\partial \delta}{\partial w} = 0$), the Couette flow (figure 2.1(c), statistically steady, $\frac{\partial p}{\partial w} = 0$, $\frac{\partial \delta}{\partial w} = 0$) and the temporally-developing boundary layer (figure 2.1(d), statistically unsteady, $\frac{\partial p}{\partial w} = 0$, $\frac{\partial \delta}{\partial w} = 0$ after a sudden change of boundary conditions. In the following, we briefly review studies that modify these canonical flow scenarios to a similar flow over concave walls.

[...] Modifying the classic stability problem of a flat, spatially developing boundary layer to account for concave wall curvature (figure 2.1(a)) significantly changes its stability properties, as described by Floryan [35] and Saric [112]. In flows above concave walls, pairs of streamwise vortices, i.e. Görtler vortices [38], are formed, which get corrupted further downstream by sec-

ondary instabilities. Experiments by Bippes [9] and Swearingen & Black-welder [126] provide visualisations of two distinct secondary instability mechanisms: a sinuous mode, leading to spanwise meandering of the streamwise vortices and a varicose mode, resulting in hairpin-like structures. Linear stability theory was applied to assess the primary instability [34] and the secondary instabilities [46, 72]. Due to its high relevance in turbomachinery, recent work focuses on the receptivity of Görtler vortices towards roughness and freestream turbulence [120, 144], compressibility effects [108] as well as the control of these instabilities [121].

The canonical, spatially developing boundary layer over flat plates has been extensively studied both in laboratory experiments and in recent numerical simulations [118, 143, 123]. The sizeable computational cost limits the value of Re that can be achieved in numerical investigations. This limitation is shared also by studies of boundary layers over concave walls, which consist almost exclusively by laboratory experiments. Meroney & Bradshaw [92], Hoffmann *et al.* [51] and Barlow & Johnston [3] allow transition to turbulence in a straight channel section and, before the flow becomes fully developed, a boundary layer of finite thickness enters a curved section of the channel. The studies revealed persistence of streamwise rolls with wavelengths similar to the boundary-layer thickness even in the turbulent stage, which result in enhanced Reynolds stresses.

Significantly lower computational effort and experimental complexity than in spatially developing boundary layers is required when turbulence is characterised in spatially confined, fully developed and pressure-driven flows such as channels and pipes (see figure 2.1(b) and amongst others [60]). Experimental [54] and numerical [95] investigations on fully developed curved channel flows also showed deviations in Reynolds stresses due to large-scale, streamwise and wall-parallel vortices with scales similar to the channel height (the so-called Dean instability [22]).

Applying curvature to the classical Couette flow leads to a shear flow between two coaxial cylinders: the TC flow, first addressed by Taylor [128] (figure 2.1(c)). As the system can be easily controlled, statistically steady, closed, and symmetric, it allows accurate measurements with moderate complexity of the experimental apparatus as well as affordable numerical simulations even for large values of *Re*. Depending upon the relative and absolute rotational speeds, the radii of the two cylinders and fluid properties, a large variety of different flow structures can be produced. A broad body of literature deals with TC thanks to its simple set-up, the variety of competing physical phenomena occurring in the flow and the similarity with the Rayleigh-Bénard convection. Recent reviews are given by Fardin *et al.* [30] and Grossmann *et al.* [45].

The temporal evolution of a turbulent incompressible boundary layer after an impulsive acceleration of a flat wall – the so-called Stokes' first problem (figure 2.1(d)) – is the flat plate counterpart of the problem investigated here in the present study [chapters 3 and 4], at least during the first phases of the spin-down process. While the linear stability of the flow was already analysed by Luchini & Bottaro [81] almost two decades ago, Kozul *et al.* [66] recently identified and closed a gap in the literature concerning the in-depth analysis of the turbulent state of such flows. Transferring Stokes' first problem to a flow with concave wall curvature, results in an azimuthally accelerated cylinder. According to the Rayleigh criterion the effects of centrifugal instabilities are only present in the case of a cylinder deceleration, which corresponds to the spin-down case investigated in the present study [chapters 3 and 4]." [Kaiser et al., 2020a].

2.3.2 Free shear layers

As mentioned in § 2.3.1, the suction-side boundary layer and its vorticity annihilation introduce centrifugal instabilities into the flow. However, simultaneously with the suction-side boundary layer, another shear flow develops when a propulsor is accelerated: a separated free shear layer. A sheet of high

vorticity separates from the propulsor at a separation point, which is subsequently referred to as the vortex-forming edge (VFE). Before the separated shear layer rolls up into the vortex, it inherits its own instabilities, which in turn influence the entrainment of non-vortical fluid into the shear layer (and thus the vortex). In the present section, an overview of previous studies on free shear layers is given. In particular, the influence of shear-layer curvature and Re on entrainment is discussed.

The dominant instability mechanism for a planar free shear layer is the Kelvin–Helmholtz instability (KHI) [74, 93]. Both, inviscid linear spatial [93] and temporal [74] stability theory provide good agreement with experimental results concerning the early evolution of the instabilities. During the linear stage, viscous effects are minor and mainly damp the evolution of the dominant wavelengths, while not significantly influencing their wavenumber [74]. However, viscous effects become more relevant once the non-linear regime is entered. Vortices start to merge [50] and additional small scale structures emerge as visualised in Schaal *et al.* [116]. Inside those structures, non-vortical and vorticity-containing fluid are separated by a sharp interface, which is often referred to as the turbulent non-turbulent interface (TNTI). Along the TNTI vorticity is transferred at scales on the order of the Kolmogorov length scale [20], leading to entrainment of non-vortical fluid into the shear layer. While viscous effects (and thus Re) intrinsically influence vorticity diffusion and thereby the entrainment process at the interface [139, 17], also the evolution and size of the vortical structures in the shear layer impact the entrainment process. Vortical structures engulf areas of non-vortical fluid [12] and thereby increase the surface of the TNTI and the entrainment rate.

In the case of curved free shear layers, the curvature influences the linear instability mechanisms [77]. Dependent on the boundary conditions, the curvature effects can decrease the spatial growth rate of the dominant KHI wavelength due to centrifugal forces or even introduce additional structures resulting from centrifugal instabilities [77].

3 Wall-bounded vortex decay – numerical approach

This chapter is based on the publication *On the stages of vortex decay in an impulsively stopped, rotating cylinder* [Kaiser et al., 2020a]. The chapter is supplemented by additional discussions, which go beyond the scope of the publication and relate the fundamental results to the guiding example of the present thesis, i.e. vortex formation in bio-propulsion.

"An infinitely long cylinder of radius R has its axis aligned with the axial direction of a cylindrical coordinate system with radial, azimuthal and axial coordinates denoted respectively (r, φ, z). The cylinder is filled with an incompressible Newtonian fluid of kinematic viscosity ν and rotated with angular velocity Ω (see figure 3.1) until solid-body rotation (SBR) of constant axial vorticity $\omega = 2\Omega$ is achieved. This flow is characterised by the following velocity field

$$u_\varphi(r) = \Omega r, \quad u_r = u_z = 0.$$
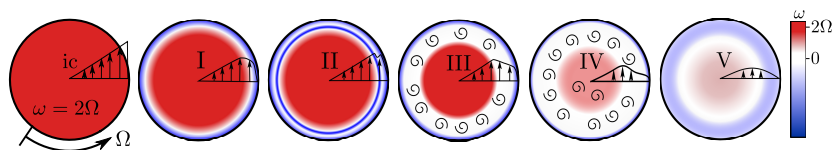
Figure 3.1: Schematic describing the evolution of vorticity (colour coded) and azimuthal velocity profile (vectors) during the distinct stages of the spin-down process: initial condition (ic), laminar stage (I), instabilities and transition to turbulence (II), sustained turbulence with intact vortex core (III), corruption of vortex core and decay of turbulence (IV), and relaminarisation (V). Spirals illustrate the existence of turbulent fluctuations in stages III and IV. Figure adapted from [Kaiser et al., 2020a].

The numerical experiment begins at the temporal instant $t = 0$ when, starting from the condition of SBR, the rotation of the cylinder wall is suddenly stopped. Following this event, a transient unsteady flow develops, referred to here as *spin-down*.

Figure 3.1 presents the different stages of the spin-down process. Each stage is characterised by unique flow features, which are strongly influenced by the boundary conditions – specifically the concave walls of the cylinder. After the laminar boundary layer formation (stage I), centrifugal instabilities emerge as addressed experimentally by Euteneuer [28] and Mathis & Neitzel [86]. These instabilities have also been studied analytically by Neitzel [96] and Kim *et al.*[62]. However, only Euteneuer [28] extended their work up to the nonlinear saturation of the primary instability (in stage II). Yet the subsequent stages of the spin-down process have not been investigated: the secondary instability (end of stage II), a stage of sustained turbulence (stage III), the decay of turbulence (stage IV) and the relaminarisation (stage V) itself.

These later stages (stages II-V) are characterised by centrifugal instabilities and the onset of turbulence. The kinetic energy initially present in the SBR is not only dissipated through the viscous dissipation associated with a time-varying velocity profile of laminar spin-down, but also converted to turbulent fluctuations and eventually dissipated via turbulent viscous dissipation. When a large fraction of the total energy has been dissipated, turbulence does not self-sustain and a stage of viscous decay occurs yielding relaminarisation. As mentioned in studies on decaying Taylor-Couette (TC) flow by Verschoof *et al.* [134] and Ostilla-Mónico *et al.* [102], the rate at which energy is dissipated during the sustained and decaying turbulent regimes is not known *a priori*. In a similar manner, the details of production and dissipation of energy associated with turbulent fluctuations are also poorly understood. The statistical properties of the turbulent flow and the turbulence production and decay processes depend on the Reynolds number (*Re*) in at least two instances. On the one hand, there is the obvious impact of *Re* on the relative importance

of viscous and inertial stresses, and thus on turbulent statistics. On the other hand, the value of *Re* determines the stability properties of the laminar boundary layer forming at the initial stages of spin-down, thereby determining the boundary-layer properties at the instant in which instability and transition to turbulence occur.

The objective of the present work is to describe the spin-down process throughout all of its phases from onset of centrifugal instabilities to the decay of turbulence. Particular focus lies on the flow stages that have not been discussed previously and on the analysis of the turbulent properties and the effect of *Re*. This study by no means strives to completely cover all aspects of the spin-down process. Rather the paper provides an initial overview of this complex transient flow and its phenomena. Each stage on its own has significant potential for further investigations and therefore makes the spin-down problem an interesting canonical flow to assess unsteady turbulence in the presence of concave walls." [Kaiser et al., 2020a].

The present chapter is structured as follows. "Section § 3.1 contains a detailed description of the numerical method and the flow cases considered in the following. Particularly relevant are the description of the adopted Reynolds decomposition and the budget equations utilised to describe the temporal behaviour of the kinetic energy as described in § 3.2 and the definition energy spectra (see § 3.4). Starting with an overview over the temporal flow development in § 3.5, the different stages of the spin-down are discussed in detail for one of the simulated *Re* in § 3.5.1- § 3.5.5. Finally, in § 3.6 the *Re*-influence is addressed by evaluating four simulations at different *Re*, ranging over almost one order of magnitude." [Kaiser et al., 2020a]

3.1 Numerical methods and parameter space

"A newly created database of the turbulent spin-down process in cylinders is produced via direct numerical simulation (DNS). The code used in the present

Re	$u_\tau^{\max}/\Omega R$	L_{cyl}/R	$N_\varphi^{\max} \times N_r \times N_z$	$R^+\Delta\varphi$	Δr^+	Δz^+	Δt^+
3000	0.0814	2π	$136 \times 68 \times 272$	11.28	1.60	5.64	0.20
6000	0.0809	2π	$282 \times 141 \times 566$	10.81	1.52	5.38	0.16
12000	0.0766	π	$502 \times 249 \times 504$	11.51	1.63	5.73	0.18
28000	0.0693	π	$1024 \times 500 \times 1024$	11.92	1.71	5.96	0.20

Table 3.1: Discretisation parameters of the direct numerical simulations performed in the present study. $N_\varphi^{\max}$ and N_z are the number of maximum azimuthal and axial Fourier modes used to represent the flow field without accounting for the additional modes required to exactly remove the aliasing error. N_r is the number of collocation points adopted in radial direction. The value of spatial and temporal resolutions are computed at the temporal instant of transition to turbulence, for which the friction velocity achieves its maximum value $u_\tau^{\max}$. Line colours are used in section 3.6. Table adapted from [Kaiser et al., 2020a].
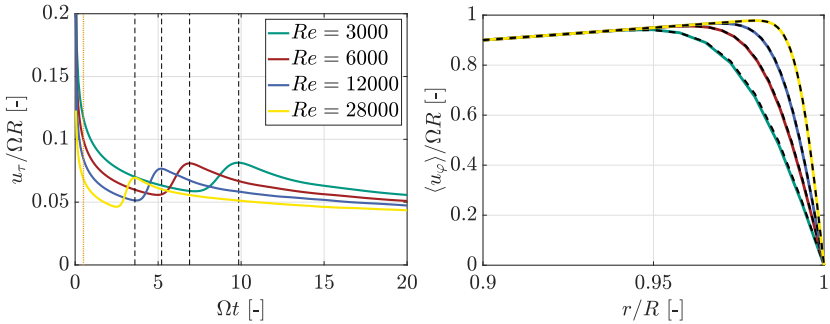
(a) Temporal development of the friction velocity u_τ at different values of Re. The maximum value, achieved during transition and used to determine the spatial resolution in the numerical simulation, is marked with dashed black lines.

(b) Averaged azimuthal velocity profiles at $\Omega t = 0.5$ (the instant is marked by a vertical dotted orange line in figure 3.2(a)) compared with the respective analytical solution (dashed black lines).

Figure 3.2: Procedure to select the spatial and temporal resolution of the numerical simulation. Figure adapted from [Kaiser et al., 2020a].

study is a mixed-discretisation parallel solver of the incompressible Navier–Stokes equations in cylindrical coordinates [29, 85]. Velocity and pressure fields are discretised via a Fourier–Galerkin approach along the two statistically homogeneous azimuthal (φ) and axial (z) directions, while second-order explicit compact finite-difference schemes [69] based on a three-point computational stencil on an inhomogeneous grid are adopted in the radial direction (r). Spectral accuracy is therefore achieved for the discretisation of all differential operators in the statistically homogenous directions. The accuracies of the differential operators $D_1 = \frac{\partial}{\partial r}$ and $D^* = \frac{\partial}{\partial r}\left(r\frac{\partial}{\partial r}\right)$ operating in the radial direction are fourth and second order, respectively. The incompressibility constraint is enforced within machine accuracy by direct solution of the continuity equation, which is coupled with pressure through the radial component of the momentum equation for the collocation point in the fluid domain closest to the wall. The number of Fourier modes in the azimuthal direction decreases from the wall towards the cylinder axis as a linear function of r, so that the azimuthal resolution $r\Delta\varphi$ is kept constant across the cylinder. The regularity boundary conditions (RBCs) [71] are based upon the invariance of the solution with respect to the origin of the coordinate system. RBCs are enforced at the cylinder axis, for all wavenumber pairs that exist throughout the cylinder cross-section, or at the radial position that represents the boundary for wavenumber pairs that only exist above certain values of r.

The governing equations are advanced in time starting from the initial condition of a fully established SBR. No pressure gradient is imposed in the axial direction. Temporal discretisation is achieved with an implicit second-order Crank–Nicholson scheme for the linear terms combined with an explicit third-order low-storage Runge–Kutta scheme for the nonlinear part of the governing equations. Random disturbances with constant energy of $10^{-12}\Omega^2 R^2$ satisfying no-slip boundary conditions are superimposed to each wavenumber and velocity component of the initial velocity field in the whole cylinder volume. The first time step of the simulation forces the random disturbance to ful-

fil the continuity equation. In the resulting divergence-free field, the energy contained in each wavenumber and velocity component space is randomly distributed and is bound by $10^{-12.55}\Omega^2 R^2$ and $10^{-11.5}\Omega^2 R^2$. Henceforth, governing equations and all variables are normalised via the cylinder radius R and the initial angular velocity Ω of the SBR. Four different numerical experiments are performed, characterised by different values of the Reynolds number $Re = \frac{\Omega R^2}{\nu} \in \{3000, 6000, 12\,000, 28\,000\}$, where ν is the kinematic viscosity of the fluid. The discretisation parameters are summarised in table 3.1.

Spatial and temporal resolutions are set to fulfil the requirements for wall-bounded turbulence [60] at all times of the temporal evolution of the flow. The resolutions are expressed in terms of viscous units, i.e. normalised via the kinematic viscosity ν of the fluid and the friction velocity $u_\tau = \sqrt{\tau_w/\rho}$. Here, τ_w is the spatially averaged wall shear stress and ρ is the fluid density. Normalisation in viscous units is indicated with the superscript $+$. The most stringent requirement for spatial resolution is achieved after onset of transition, when u_τ reaches the maximum value $u_\tau^{\max}$. At this time instant, indicated by dashed black lines in figure 3.2(a), the azimuthal, axial and minimum radial resolutions are $R^+\Delta\varphi \approx 11$, $\Delta z^+ \approx 6$ and $\Delta r_{\min}^+ \approx 1.5$, respectively. These values are computed without taking into account the additional modes used to exactly remove the aliasing error. It must be noted that such resolution is finer than the one required to correctly describe the onset of turbulent transition, as discussed in § 3.5. The resolution in viscous units improves for all other later time instants. The axial extent L_{cyl} of the computational domain is a compromise between the need for accommodating several Taylor rolls [100, 11], providing sufficient area for reliable computation of spatially averaged quantities, and constraining the computational effort and the required disk space for storing the large data sets." [Kaiser et al., 2020a]

3.2   Reynolds decomposition and energy budgets

For the sake of brevity, this section only provides a brief overview (in parts adapted from [Kaiser et al., 2020a]) of the budget equations utilised in section 3.5. The detailed derivation of the given equations is provided in Appendix A.1–A.3.

"The spin-down process is statistically unsteady, for which the Reynolds decomposition applied to the velocity field reads

$$u_i(r, \varphi, z, t) = \langle u_i \rangle_{\varphi, z}(r, t) + u_i'(r, \varphi, z, t), \tag{3.1}$$

where index notation is used to indicate the i-th velocity component in the respective direction of cylindrical coordinates (r, φ, z): $\langle \cdot \rangle_{\varphi, z}$ denotes averaging along the statistically homogeneous azimuthal and axial directions. It must be noted that the ensemble average of independent repetitions of the same experiment is applicable to unsteady problems. However, this has not been performed in the present study, for which spatial averaging resulted in sufficient statistical convergence. In equation (3.1) $u_i'(r, \varphi, z, t)$ is the fluctuating velocity field about the average value $\langle u_i \rangle_{\varphi, z}(r, t)$. In the following, the notation $\langle u_i \rangle = \langle u_i \rangle_{\varphi, z}(r, t)$ and $u_i' = u_i'(r, \varphi, z, t)$ is used for brevity." [Kaiser et al., 2020a]

3.2.1   Mean and turbulent kinetic engergy

"The temporal decay of the kinetic energy contained in the initial SBR is investigated in the present study. In the framework of the Reynolds decomposition, kinetic energy is split into mean kinetic energy K, associated with the averaged flow field $\langle u_i \rangle$, and turbulent kinetic energy k, associated with the fluctuating field u_i'. As $\langle u_r \rangle = \langle u_z \rangle = 0$ in the present flow, the mean kinetic energy is given

by $K = \frac{1}{2}\langle u_\varphi \rangle^2$. Its temporal evolution is governed by the following budget equation [derivation of the equations given in Appendix A.3]:

$$
\frac{\partial K}{\partial t} = \underbrace{-\frac{\partial}{\partial r}\left(\langle u_\varphi \rangle \langle u_r' u_\varphi' \rangle\right) - \frac{\langle u_\varphi \rangle \langle u_r' u_\varphi' \rangle}{r}}_{T_m} + \underbrace{\frac{\partial}{\partial r}\left(\nu \langle u_\varphi \rangle \frac{\partial \langle u_\varphi \rangle}{\partial r}\right) + \frac{\nu}{2r}\frac{\partial \langle u_\varphi \rangle^2}{\partial r}}_{V_m} \dots
$$

$$
\dots + \underbrace{\langle u_r' u_\varphi' \rangle \left(\frac{\partial \langle u_\varphi \rangle}{\partial r} - \frac{\langle u_\varphi \rangle}{r}\right)}_{P} \underbrace{- \nu \left(\frac{\partial \langle u_\varphi \rangle}{\partial r}\right)^2 - \nu \frac{\langle u_\varphi \rangle^2}{r^2}}_{\epsilon_m} \quad (3.2)
$$

where T_m is the turbulent diffusion, V_m the viscous diffusion and ϵ_m the dissipation of K. The turbulence production term P couples the budget equation of K and k as it draws energy from the mean flow and transfers it to the fluctuating field. Following Mansour *et al.*[83] and Bilson & Bremhorst[8] the budget equation for $k = \frac{1}{2}\left(\langle u_z' u_z' \rangle + \langle u_r' u_r' \rangle + \langle u_\varphi' u_\varphi' \rangle\right)$ is given by

$$
\frac{\partial k}{\partial t} = \underbrace{-\frac{1}{2r}\frac{\partial (r \langle u_r' u_i' u_i' \rangle)}{\partial r}}_{T_t} + \underbrace{\frac{\nu}{2r}\frac{\partial}{\partial r}\left(r\frac{\partial \overline{\langle u_i' u_i' \rangle}}{\partial r}\right)}_{V_t} \dots
$$

$$
\dots \underbrace{-\frac{1}{\rho}\left(\frac{\partial (\langle u_r' p' \rangle)}{\partial r} + \frac{\langle u_r' p' \rangle}{r}\right)}_{\Pi^d} \underbrace{- \langle u_r' u_\varphi' \rangle \left(\frac{\partial \langle u_\varphi \rangle}{\partial r} - \frac{\langle u_\varphi \rangle}{r}\right)}_{P} \dots
$$

$$
\dots \underbrace{- \nu \left[\left\langle \frac{\partial u_i'}{\partial z}\frac{\partial u_i'}{\partial z}\right\rangle + \left\langle \frac{\partial u_i'}{\partial r}\frac{\partial u_i'}{\partial r}\right\rangle + \frac{1}{r^2}\left\langle \left(\frac{\partial u_\varphi'}{\partial \varphi} + u_r'\right)^2 + \left(\frac{\partial u_r'}{\partial \varphi} - u_\varphi'\right)^2\right\rangle\right]}_{\epsilon_t}.
$$

$$
(3.3)
$$

Here, the viscous diffusion V_t, the pressure diffusion Π^d and the turbulent diffusion T_t describe the transport of k, while ϵ_t is its viscous dissipation.

Beyond the averaging in axial and azimuthal direction, the closed system allows averaging in the cylinder volume V, which is indicated in the following with the volume averaging operator $[\cdot]$. The volume-averaged total kinetic energy $[K]+[k]$ can be expressed as

$$[K]+[k] = \frac{1}{2V\Omega^2 R^2} \int_V u_i u_i \mathrm{d}V = \frac{1}{2V\Omega^2 R^2} \int_V \langle u_i \rangle^2 \mathrm{d}V + \frac{1}{2V\Omega^2 R^2} \int_V \langle u_i' u_i' \rangle \mathrm{d}V.$$
(3.4)

Due to the no-slip conditions at the decelerated cylinder walls, energy is constantly withdrawn from the system. The temporal change of kinetic energy $[K]+[k]$ can be described by volume averaging and summation of the equations (3.2) and (3.3). All transport terms T_t, V_t, T_m, V_m and Π_d contained in the two equations vanish by definition. Also the production P, which appears in both equations for $[K]$ and $[k]$ with an opposite sign, vanishes when the volume average of the kinetic energy $[K]+[k]$ is evaluated. As a consequence, only the dissipation terms ϵ_t and ϵ_m remain." [Kaiser et al., 2020a]

The temporal change of the volume average of total kinetic energy simplifies to

$$\frac{\partial([K]+[k])}{\partial t} = \frac{\partial[K]}{\partial t} + \frac{\partial[k]}{\partial t} = [\epsilon_m]+[\epsilon_t] = [\epsilon_{tot}].$$
(3.5)

3.3 Wall-based flow description

"To characterise turbulence in the developing boundary layer during spin-down, the classical friction Reynolds number

$$Re_\tau = u_\tau \delta_{99}/\nu$$
(3.6)

is introduced [58], in which δ_{99} is the boundary-layer thickness and $u_\tau = \sqrt{\tau_w/\rho}$ is the friction velocity based on the mean wall shear stress

$$\tau_w = \rho v \frac{\partial \langle u_\varphi \rangle}{\partial r}\bigg|_{r=R}. \tag{3.7}$$

Note that in the investigated flow τ_w, u_τ, δ_{99} and Re_τ change with time t. Due to the lack of a constant outer velocity, the traditional definition of δ_{99} is adapted by using the retracting vortex core in SBR as follows

$$\Omega(R - \delta_{99}) - \langle u_\varphi \rangle = 0.01\Omega R, \tag{3.8}$$

i.e. δ_{99} is defined as the distance from the wall, at which the flow deviates $0.01\Omega R$ from the initial SBR." [Kaiser et al., 2020a]

3.4 Energy spectra

"The appearance of Taylor rolls will be assessed by the analysis of the power spectral density of k. The summands of $k = \frac{1}{2}\langle u_i' u_i' \rangle$ are split up into the contribution of different axial modes κ_z of wavelength $\lambda_z = L_{cyl}/\kappa_z$. The axial energy spectra are given by

$$\Phi_{u_i u_i} = \Phi_{u_i u_i}(r, \kappa_z) = \int_{\kappa_\varphi^{min}}^{\kappa_\varphi^{max}} \mathfrak{R}\langle \hat{u}_i(\kappa_\varphi, \kappa_z, r)\hat{u}_i^*(\kappa_\varphi, \kappa_z, r)\rangle d\kappa_\varphi \tag{3.9}$$

where $\mathfrak{R}$ is the real part of a complex number, $\hat{\cdot}$ indicates the Fourier coefficients and the superscript $*$ denotes complex conjugation. By accumulating the energy of all modes except the base flow the summands of k are recovered,

$$\langle u_i' u_i' \rangle(r,t) = \int_{\kappa_z^1}^{\kappa_z^{max}} \Phi_{u_i u_i} d\kappa_z = \int_{\lambda_z^{min}}^{\lambda_z^{max}} \kappa_z \Phi_{u_i u_i} d(\ln(\lambda_z)). \tag{3.10}$$

To gather information about the linear and subsequent nonlinear growth of the different modes κ_z in the boundary layer, the energy spectrum $\Phi_{u_\varphi u_\varphi}$ is spatially averaged over the fluid volume contained in the boundary layer $V_\delta = \pi(2R\delta_{99} - \delta_{99}^2)L_{cyl}$, resulting in the one-dimensional spectrum

$$\frac{1}{V_\delta} \int_{V_\delta} \int_{\kappa_z^1}^{\kappa_z^{max}} \Phi_{u_\varphi u_\varphi} \, d\kappa_z dV = \int_{\kappa_z^1}^{\kappa_z^{max}} \underbrace{\frac{2\pi L_{cyl}}{V_\delta} \int_{R-\delta_{99}}^{R} \Phi_{u_\varphi u_\varphi} r dr}_{\xi_{\varphi\varphi}(\kappa_z)} d\kappa_z \qquad (3.11)$$

for each time step: $\xi_{\varphi\varphi}$ thus describes the contribution to $\langle u'_\varphi u'_\varphi \rangle$ of each wavenumber κ_z throughout the whole boundary layer. " [Kaiser et al., 2020a]

3.5 Flow regimes

"Dimensional analysis provides two dimensionless groups for the present flow: the Reynolds number $Re = \Omega R^2/\nu$ and a dimensionless time. Two distinct yet convertible representations of the dimensionless time are utilised in the following: the viscous time $\nu t/R^2$ and the outer time $\Omega t = Re \cdot \nu t/R^2$,
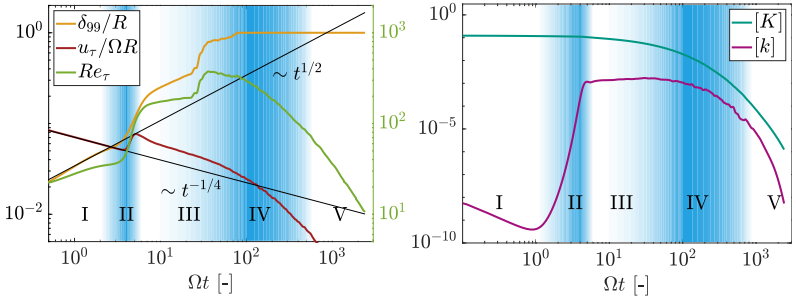
(a) Boundary-layer thicknesses δ_{99}, friction velocity u_τ and friction Reynolds number Re_τ.

(b) Mean $[K]$ and turbulent $[k]$ kinetic energy. Roman numbers I-V and background colouring indicate the different stages of the decay process.

Figure 3.3: Temporal development of bulk flow statistics for the spin-down process at $Re = 12\,000$. Figure adapted from [Kaiser et al., 2020a].

(a) Turbulent production $[P]$, mean dissipation $[\epsilon_m]$, turbulent dissipation $[\epsilon_t]$ and total dissipation $[\epsilon_{tot}]$.

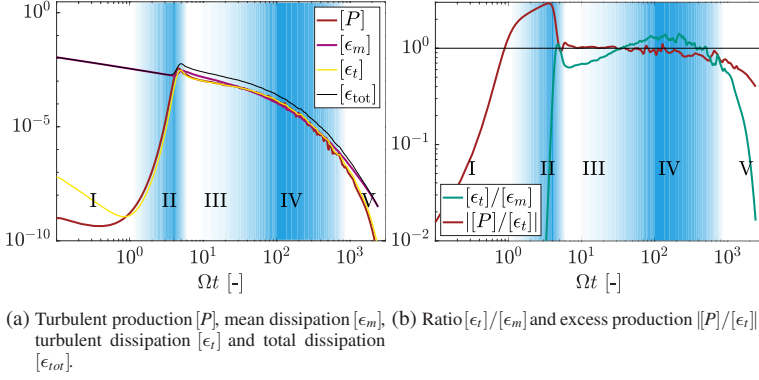(b) Ratio $[\epsilon_t]/[\epsilon_m]$ and excess production $[[P]/[\epsilon_t]]$.

Figure 3.4: Temporal development of the volume-averaged $[K]$ (3.2) and $[k]$ (3.3) budgets for the spin-down flow at $Re = 12\,000$. Figure adapted from [Kaiser et al., 2020a].

where $\Omega t = 2\pi$ represents a full revolution of the SBR. This section discusses the temporal development of the spin-down flow at $Re = 12\,000$, before the Re scaling is addressed in § 3.6.

Figures 3.3 and 3.4 provide a first overview of the flow evolution. Roman numbers I-V and background colouring indicate the different stages of the decay process. While each stage is characterised by unique features, the transition between stages occurs gradually and thus cannot be exactly localised in time.

During stage I, a stable, laminar boundary layer grows from the cylinder wall at a rate proportional to the viscous time scale $\sqrt{\nu t}$ (see figure 3.3(a)), while the friction velocity u_τ decreases. Since the increase in boundary-layer thickness outweighs the decrease in u_τ, Re_τ increases mildly in time. Figure 3.3(b) shows the corresponding evolution of volume-averaged mean and turbulent kinetic energy. As expected, $[K]$ decreases and the initial random disturbances contained in $[k]$ also decay in the stable boundary layer. Stage II is characterised by the centrifugal instability associated with the emergence of Taylor vortices and subsequent breakdown to turbulence. The sudden increase of u_τ and δ_{99} (and thus Re_τ) is accompanied by the exponential growth of $[k]$.

After transition to turbulence, stage III is entered. In this stage, $[k]$ varies slowly in time. The flow consists of the superposition of a constantly retracting SBR core at the centre of the cylinder and a turbulent boundary layer close to the cylinder wall. The latter is characterised by decreasing u_τ and increasing δ_{99}. The beginning of stage IV is marked by the breakdown of the SBR core, in which turbulent fluctuations become non-negligible and induce a reduction of $\langle u_\varphi \rangle$ inside the vortex core. Two distinct phenomena occur during stage IV. First, the breakdown of the SBR core is accompanied by a sudden increase of δ_{99} with no discernible effect on u_τ or $[k]$. Then, after the SBR core has been completely eroded by turbulence, $[k]$ and Re_τ drop in time. Finally, the temporal evolution of the flow ends with the viscous decay of stage V.

Figure 3.4a shows the temporal evolution of $[P]$, $[\epsilon_t]$ and $[\epsilon_m]$ during the five stages. In stage I, energy dissipation is governed by $[\epsilon_m]$, while very small values of $[\epsilon_t]$ indicate the decay of the initial disturbances (figure 3.4(a)). At the end of stage I, $[P]$ begins to increase in time until $[P]$ exceeds $[\epsilon_t]$, at which point the Taylor rolls emerge in stage II and yield the fast increase of $[k]$ discussed above. The onset of turbulence is accompanied by a strong increase of $[\epsilon_t]/[\epsilon_m]$ (figure 3.4(b)), after which $[\epsilon_t]$ and $[P]$ are in equilibrium, yielding the sustained turbulent regime of stage III with only marginal variation of $[k]$ (figure 3.3(b)). Within stage IV the ratio of dissipation $[\epsilon_t]$ and production $[P]$ leans towards dissipation and $[k]$ begins to decay. Eventually, the flow laminarises and the ratio $[\epsilon_t]/[\epsilon_m]$ drops significantly while $[\epsilon_{tot}] \approx [\epsilon_m]$. This final stage, which is most evident in figure 3.4(b), is referred to as stage V." [Kaiser et al., 2020a]

35

3.5.1 Stage I: Laminar boundary layer

"The laminar stage of the flow, for which $u'_i = 0$ and thus $u^{lam}_\varphi = \langle u_\varphi \rangle$, can be described by the analytical solution of [96]

$$\frac{u^{lam}_\varphi}{\Omega R} = -2 \sum_{i=1}^{\infty} \frac{J_1(\beta_i r/R)}{\beta_i J_0(\beta_i)} \exp(-\beta_i^2 \nu t/R^2), \qquad (3.12)$$

where J_0 and J_1 are Bessel functions of the first kind and β_i are the roots of $J_1(\beta_i) = 0$. For small t, while δ_{99}/R is small and the local curvature is negligible, the present boundary layer above the concave wall is similar to Stokes' first problem [119]. Thus, for small t, the growth rate of δ_{99} coincides with the growth rate of the boundary layer in the vicinity of a impulsively accelerated flat plate (here indicated with the superscript St),

$$\delta^{St}_{99} = a^{St}_{lam} \sqrt{\nu t} \approx 3.64 \sqrt{\nu t}. \qquad (3.13)$$

However, with increasing δ_{99}/R the growth rate of δ_{99} in the spin-down problem, computed exploiting the exact analytical solution (3.12), deviates from δ^{St}_{99} due to curvature effects. The deviation is such that δ_{99} can be made directly proportional to $\sqrt{\nu t}$, only if the proportionality coefficient a_{lam} is a weak function of time.

For simplicity, in the following analyses the growth rate during stage I is characterised through a constant growth rate coefficient a_{lam}, which is determined via a least square fit of the expression

$$\delta_{99} \approx a_{lam} \sqrt{\nu t} \qquad (3.14)$$

to the analytical solution for the spin-down process, which yields $a_{lam} \approx 3.68$. The approximation of neglecting the temporal variation of a_{lam} in (3.14) introduces an error smaller than $0.01\delta_{99}$ for $0 < \delta_{99} < 0.28R$. The good agreement
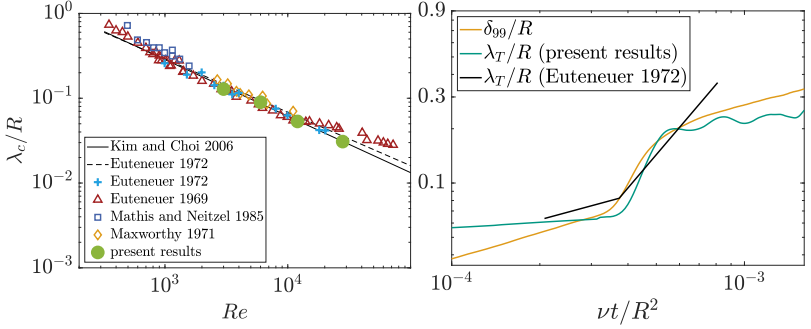
(a) Critical wavelength λ_c as a function of Re. Hollow symbols and lines are experimental data and correlations from the literature mentioned in the legend, respectively. Green dots denote current results

(b) Temporal evolution of δ_{99} and $\lambda_T(t)$ for the present numerical simulation compared against the measurement by [28] at $Re = 12\,000$.

Figure 3.5: Critical λ_c for different Re and dominant wavelength $\lambda_T(t)$ for $Re = 12\,000$. Note that in (a) the values of λ_c reported by Maxworthy [87] and Mathis & Neitzel [86] have been rescaled by a factor 0.5 due to their different definition of λ_c, as noted by Kim & Choi [61]. Figure adapted from [Kaiser et al., 2020a].

of (3.14) (black line) with the numerical results is emphasised in figures 3.3(a) and 3.6(a)." [Kaiser et al., 2020a].

3.5.2 Stage II: Emergence of Taylor rolls and laminar-to-turbulent transition

"If Re is large enough (the stability limit in literature varies in the range of $128 < Re < 350$), the boundary layer is linearly stable only until a critical time $\theta_c = \nu t_c / R^2$, after which the boundary layer undergoes linear primary centrifugal instability. The instability results in the emergence of radial plumes, which later evolve into Taylor rolls. The plumes occur at a characteristic time-dependent spacing $\lambda_T(t)$ in the axial direction, which at the critical time θ_c is representative of the linearly most-amplified axial wavelength, the so-called critical wavelength $\lambda_c = \lambda_T(\theta_c)$. For the sake of validation, the values of λ_c extracted from the present numerical simulation are compared in figure 3.5(a) against results obtained in the literature via linear stability analyses [61] and

37

laboratory experiments [87, 27, 28, 86]. In the present work, λ_c is measured as the most energetic wavelength of $\xi_{\varphi\varphi}(\kappa_z, \theta_c)$ (see §3.4 for the definition of $\xi_{\varphi\varphi}$) during the early stage of the linear growth and shows excellent agreement with these existing studies.

Figure 3.5(b) compares $\lambda_T(t)$ computed from the present numerical data against the experimental results of Euteneuer [28] at $Re = 12\,000$. Euteneuer [28] estimated the critical wavelength by counting the number of toroidal Taylor rolls aligned along the axial dimension of his experimental set-up. It was found that the rate of change in the observed number of streamwise rolls changes abruptly. This change in growth rate was referred to as *'Knickstelle'*, the German word for "kink", the origin of which will be discussed in the following.

Figure 3.6 shows the initial evolution of δ_{99}, u_τ, $[k]$, $[K]$ and $\xi_{\varphi\varphi}$. The flow at four selected time instances, marked with dashed black lines in figure 3.6, is visualised in figure 3.7. Figure 3.7 consists of a pre-multiplied spectrum $\kappa_z \Phi_{u_i u_i}$, the one-dimensional spectrum $\xi_{\varphi\varphi}$ averaged over the boundary layer and a (r,z)–slice of u'_φ. The respective boundary-layer thickness δ_{99} is depicted with an orange line. The complete corresponding temporal evolution is provided in supplementary material [of [Kaiser et al., 2020a]] Movie1.mp4 available at https://doi.org//10.1017/jfm.2019.974.

During the early linear stage ($\Omega t = 1$, figure 3.7(a)) most modes decay and only a narrow band of axial wavenumbers $\kappa_z \approx \kappa_c$ is amplified. This is most clearly visible in figure 3.6(c), where the temporal evolution of $\xi_{\varphi\varphi}$ is reported for relevant wavenumbers. As the mean velocity profile changes due to the temporal growth of the boundary layer, the stability properties of the mean velocity profile also change, and so does the most amplified wavenumber. Already at $\Omega t = 2$ wavenumbers $\kappa_z < \kappa_c$ are amplified and carry more energy than κ_c. This temporal change of the most amplified disturbances are represented in figure 3.6(d), in which $\xi_{\varphi\varphi}$ is reported as function of κ_z at dif-

(a) Temporal evolution of δ_{99} and u_τ

(b) Temporal evolution of $[K]$ and $[k]$

(c) Temporal evolution of $\xi_{\varphi\varphi}(\kappa_x, t)$

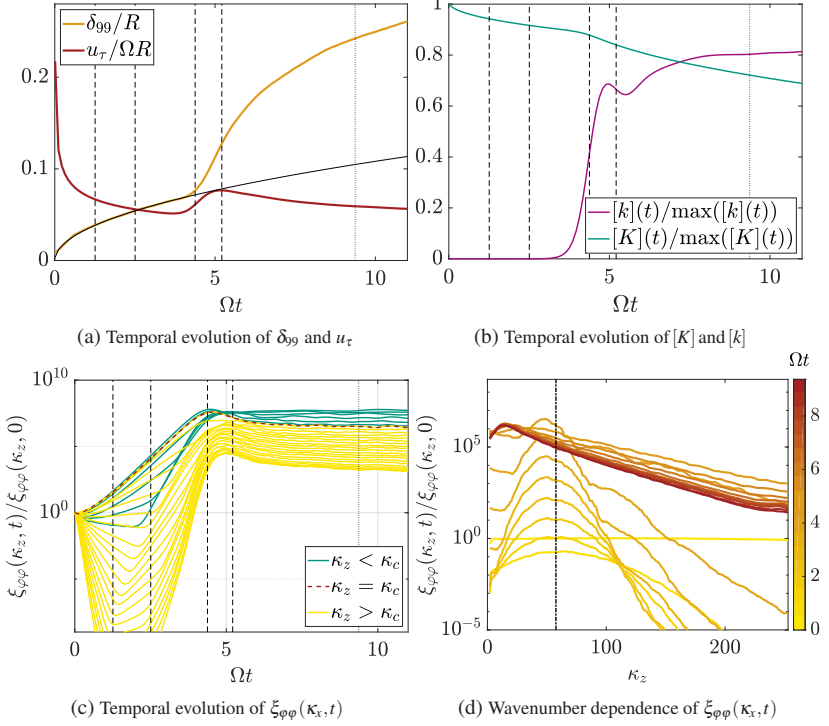(d) Wavenumber dependence of $\xi_{\varphi\varphi}(\kappa_x, t)$

Figure 3.6: Statistical quantities during the onset of primary and secondary instability. The vertical dashed lines indicate the four temporal instances $\Omega t \in \{1.0, 2.0, 4.3, 5.3\}$ that are discussed in detail in figure 3.7. The vertical dotted line marks the onset of turbulence as visualised in figure 3.10(a). The vertical dashed-dotted line in (d) marks the critical wavenumber κ_c. Figure adapted from [Kaiser et al., 2020a].
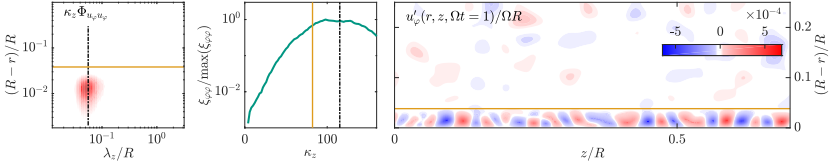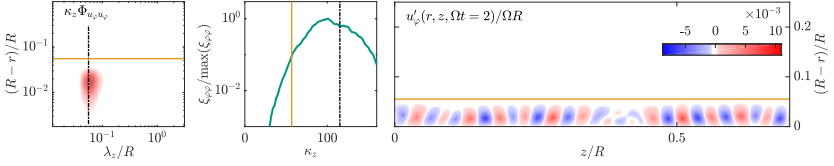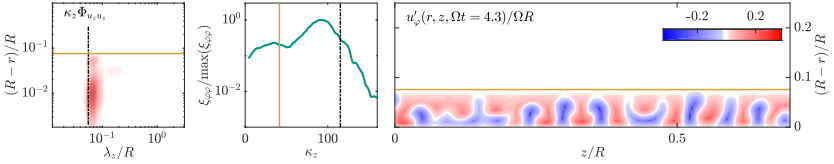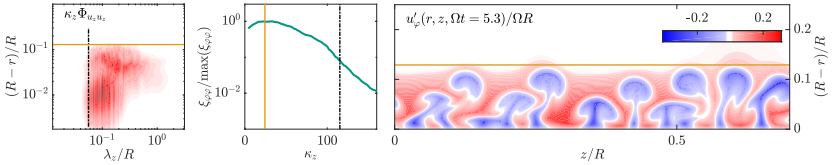
(a) exponential growth of primary instability: $\Omega t = 1$

(b) exponential growth for a broad range of modes: $\Omega t = 2$

(c) significant influence of instabilities onto the mean flow: $\Omega t = 4.3$

(d) right before onset of secondary instability: $\Omega t = 5.3$, $u_\tau(5.3) = \max(u_\tau(t))$

Figure 3.7: Pre-multiplied 1D spectra $\kappa_z \Phi_{u_i u_i}$ (left), 1D spectra $\xi_{\varphi\varphi}$ averaged across the boundary layer (middle) and instantaneous velocity fluctuations $\left\langle u'_\varphi u'_\varphi \right\rangle$ (right) during transition ($Re = 12\,000$). The orange line marks the boundary-layer thickness δ_{99} (left and right) and the wavenumber $\kappa_\delta = 2 \cdot 2\pi / \delta_{99}$, which would be the most energetic wavenumber if the streamwise vortices were circular and had diameter δ_{99}. The vertical dashed-dotted line marks the critical wavelength λ_c (left) and wavenumber κ_c (right), respectively. Figure adapted from [Kaiser et al., 2020a].

ferent temporal instances distinguishable through colour coding from the start of spin-down (bright colour) onwards.

Starting from $\Omega t = 2$ the energy of almost all wavenumbers grows exponentially, leading to increasing $[k]$ (figure 3.6(b)), until nonlinear saturation is reached and the growth stops at $\Omega t = 4.3$. At this moment, the initially amplified wavenumbers achieve their maximum energy content. The fluctuations start to influence the mean profile $\langle u_\varphi \rangle$ and thus δ_{99}, u_τ and $[K]$. The premultiplied spectrum $\Phi_{u_z u_z}$ shows a distinct second peak at a radial position close to δ_{99}, marked by an orange line in the left panels of figure 3.7(c) and 3.7(d). The second peak is related to the axial flow at the head of the radial jets, which starts the formation of plumes and streamwise vortices by redirecting the radial flow in axial direction. This process is accompanied by a simultaneous rapid growth of δ_{99}, u_τ and $[k]$ (figure 3.6a,b).

The friction velocity u_τ reaches its maximum at $\Omega t = 5.3$, right before the breakdown of this still coherent and quasi-axisymmetric flow through presence of a secondary instability. This effect will be discussed later in more detail. At this instance (figure 3.8(e)), the plumes are roughly twice as tall in the radial direction than they are wide in the axial direction, and begin to merge with adjacent plumes towards restoring an aspect ratio of unity. The sudden merging of consecutive plumes causes the dominant wavelength λ_T to shift from the critical wavelength of early linear primary instability to $\lambda_T \approx \delta_{99}$ (figure 3.6(d)). This, together with the rapidly growing δ_{99}, explains the "kink" observed by Euteneuer [28]. It can be seen in figure 3.5(b) that the numerical data reproduce the "kink" around $\nu t / R^2 \approx 3.7 \cdot 10^{-4}$ ($\Omega t \approx 4.4$). However, during the later evolution of the flow, large deviations between the present data and the curve published by Euteneuer exist. These deviations are related to the onset of the secondary instabilities and breakdown to turbulence, as discussed in the following.

Eventually, the interaction of the slow fluid transported from the wall with the fast fluid in the core leads to secondary instabilities, which cause the
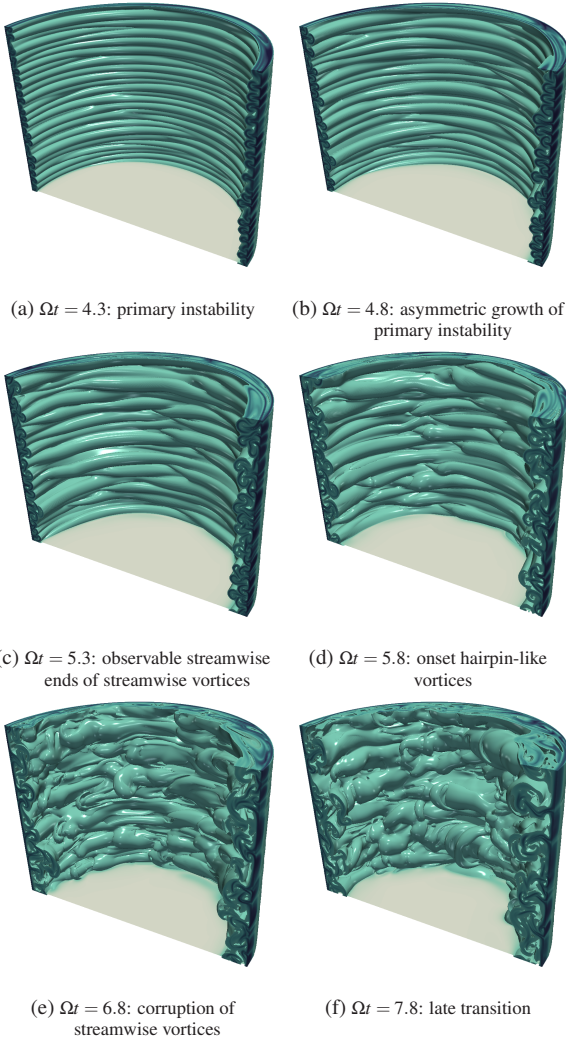
(a) $\Omega t = 4.3$: primary instability

(b) $\Omega t = 4.8$: asymmetric growth of primary instability

(c) $\Omega t = 5.3$: observable streamwise ends of streamwise vortices

(d) $\Omega t = 5.8$: onset hairpin-like vortices

(e) $\Omega t = 6.8$: corruption of streamwise vortices

(f) $\Omega t = 7.8$: late transition

Figure 3.8: FTLE visualisations of the transition process to turbulence at $Re = 12\,000$. Figure adapted from [Kaiser et al., 2020a].

breakdown of the quasi-axisymmetric flow patterns formed after the primary centrifugal instability. Two distinct competing mechanisms responsible for the onset of the secondary instability have been identified in prior studies on concave-wall flows [112]: the varicose and the sinuous mode, described in § 2.3.1. In order to observe which of the two mechanisms dominate the onset of secondary instabilities during spin-down, the LCS in the flow are visualised by means of the FTLE (§ 2.2.3). Figure 3.8 and supplementary material [of [Kaiser et al., 2020a]] Movie2.mp4 show the temporal evolution of the three-dimensional flow during transition. Linear amplification of the random disturbances given by the initial condition (details in § 3.1) results in Taylor rolls that do not cover the whole circumference of the cylinder. As such, figure 3.8(a-c) presents Taylor rolls with distinct start and ending points along the circumference. Under the action of shear, the two ends of the Taylor vortices roll up into hairpin-like vortices (figure 3.8(d)), which grow in time (figure 3.8(e)) and eventually lead to a turbulent flow populated by a richer range of vortical structures (figure 3.8(f)). Note that the detected structures are similar to FTLE visualisations of an isolated hairpin vortex in a turbulent boundary layer [41]. Therefore, the varicose mode seems to be the dominant secondary instability mechanism of the spin-down process." [Kaiser et al., 2020a]

The hypothesis that the onset of the secondary instability mechanism is related to the non-axissymmetric initial disturbances is investigated by means of an additional simulation. For $Re = 3000$ the simulation described in § 3.1 is repeated with axisymmetric initial conditions. The simulations with axisymmetric and non-axisymmetric initial conditions are compared in figure 3.9. As expected the onset of secondary instabilities is delayed for the simulation with axisymmetric initial conditions.

3.5.3 Stage III: Turbulent regime with intact vortex core

"Stage III is entered once the plumes break down into a turbulent flow. The statistical flow quantities only change slowly and multiple characteristic fea-
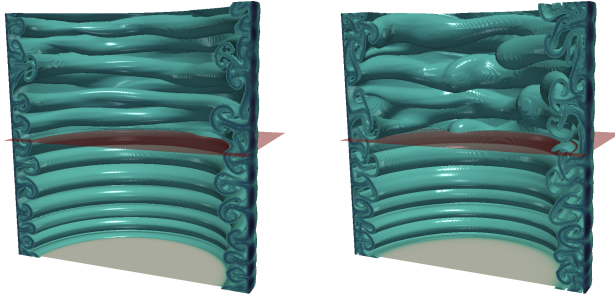
(a) non-axisymmetric Taylor rolls (top) vs. (b) onset of secondary instabilities (top)
    axisymmetric Taylor rolls (bottom)

Figure 3.9: FTLE visualisations of two distinct simulations: arbitrary, non-axisymmetric initial
conditions (top) and axisymmetric initial conditions (bottom) ($Re = 3000$). Even
though the simulation are performed independently, the results are presented together
in a single visualisation to emphasise the difference.

(a) turbulent state: $\Omega t = 9.3$

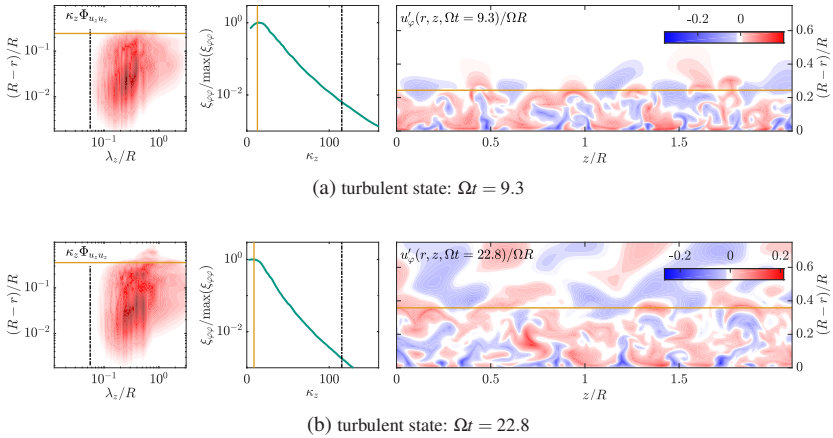(b) turbulent state: $\Omega t = 22.8$

Figure 3.10: Pre-multiplied spectra $\kappa_z \Phi_{u_i u_i}$ (left), 1D spectra $\xi_{\varphi\varphi}$ in the boundary layer (middle)
and instantaneous velocity fluctuations $\left\langle u'_\varphi u'_\varphi \right\rangle$ (right) during stage III ($Re = 12000$).
Figure adapted from [Kaiser et al., 2020a].

(a) Temporal evolution of $\langle u_\varphi \rangle$
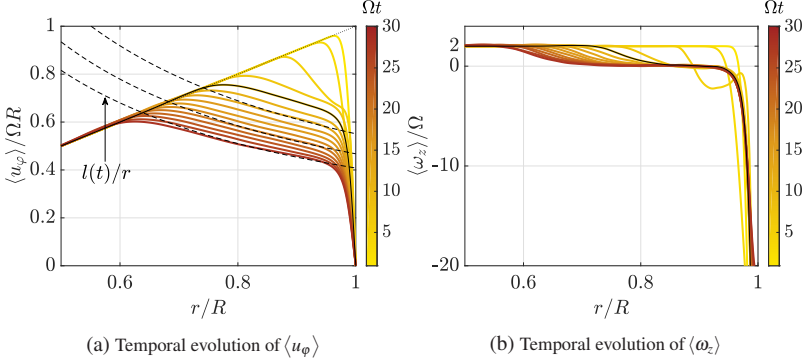
(b) Temporal evolution of $\langle \omega_z \rangle$

Figure 3.11: Temporal evolution of mean quantities during the stages I-III for the spin-down at $Re = 12\,000$. The black solid line marks the end of the transition (II) at $\Omega t \approx 9$. The temporal dependence of $\langle u_\varphi \rangle$ and $\langle \omega_z \rangle$ is colour-coded. Figure adapted from [Kaiser et al., 2020a].

tures co-exist. Figure 3.10 shows two time instances at the beginning (figure 3.10(a)) and during the later evolution (figure 3.10(b)) of stage III. The radial plumes have merged, leading to an average axial plume spacing of approximately δ_{99}. Moreover, velocity fluctuations start to reach outside the boundary layer into the SBR core (figure 3.10(a)).

Figure 3.11 shows $\langle u_\varphi \rangle$ and the mean axial vorticity $\langle \omega_z \rangle$ during stages I-III. The temporal development is colour coded and the black line depicts the end of the laminar-to-turbulent transition and the beginning of stage III. As soon as stage III is entered ($\Omega t > 9$) a region of negligible mean axial vorticity $\langle \omega_z \rangle \approx 0$ is established at radial distances between the near-wall region and the SBR. A region where $\langle \omega_z \rangle = 0$ implies a spatially constant angular momentum $l = l(t) = \langle u_\varphi \rangle r$ and is thereby equivalent to the marginally stable case of the Rayleigh instability criterion. This region is well known in other flows on concave walls, such as the TC flow [84, 103, 101] and swirling pipe flows [63]. Recovering the region of spatially constant angular momentum in this unsteady problem implies that the time scale of self-organisation in the turbulent boundary layer is significantly smaller than the outer time scale

45
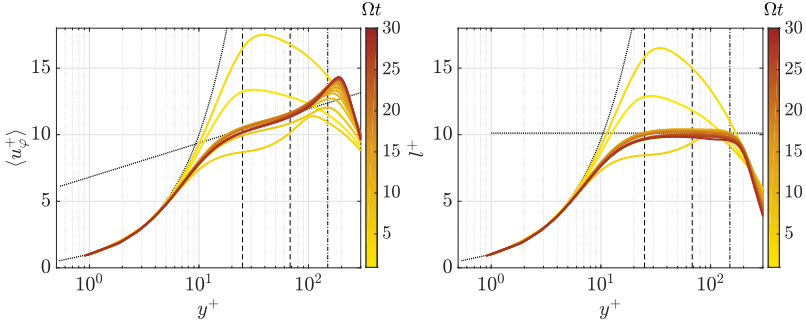
(a) Mean velocity profile $\langle u_\varphi^+ \rangle$ in viscous wall units presented in the form of the law of the wall. Dotted lines indicate the relationship $\langle u_\varphi^+ \rangle = y^+$ and (3.15) with $M = 1.11$ and $N = 6.81$.

(b) Angular momentum $l^+ = \langle u_\varphi^+ \rangle (r/R)$ in wall units. Dash-dotted vertical line marks the wall-normal distance up to which the angular momentum l^+ is approximately constant.
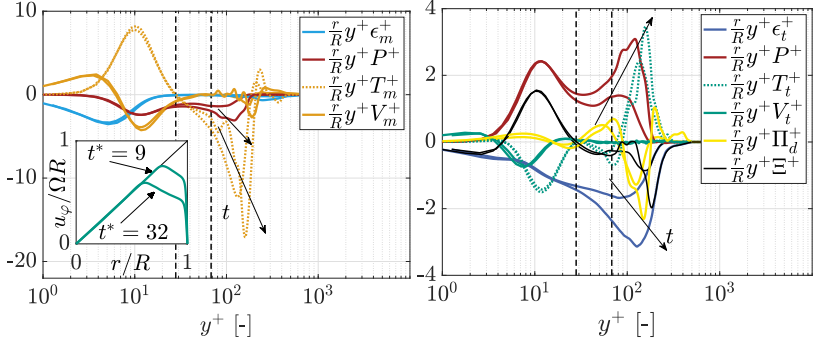
Figure 3.12: Two vertical dashed lines enclose the region of approximately logarithmic behavior of $\langle u_\varphi^+ \rangle$. Results refer to the spin-down process at $Re = 12\,000$. Figure adapted from [Kaiser et al., 2020a].

of the temporally varying mean flow. This is in good agreement with recent laboratory experiments on unsteady and turbulent TC flow by [135].

Examining the temporal development of the instantaneous value of Re_τ during stage III (figure 3.3(a)) shows that the decline of u_τ is compensated by the growth of δ_{99} so that Re_τ increases only slightly in time. Therefore, near-wall similarity is expected when turbulent statistics are normalised in time-varying viscous units, despite the statistical unsteadiness of the boundary layer. Figure 3.12(a) reports the mean velocity profile $\langle u_\varphi^+ \rangle$ at different temporal instances. A clear collapse of $\langle u_\varphi^+ \rangle$ against the wall-normal distance $y^+ = (R-r)u_\tau/\nu$ is visible as soon as stage III is entered. The approximate logarithmic behaviour

$$\langle u_\varphi^+ \rangle = M \log y^+ + N \tag{3.15}$$

is found for $y^+ > 25$, resembling what has been observed for the statistically steady TC flow, for which the constants M and N are related to the degree of curvature of the system [103, 67]. This ratio, here described by δ_{99}/R,

(a) Terms of the K budget equation (azimuthal veloc- (b) Terms of the k budget equation.
   ity profiles presented in the inlay).

Figure 3.13: Terms of the budget equations for K and k during stage III at $\Omega t = 9$ and $\Omega t = 32$ at $Re = 12\,000$. Two vertical dashed lines enclose the region of approximately logarithmic behavior of $\left\langle u_\varphi^+ \right\rangle$. Figure adapted from [Kaiser et al., 2020a].

varies in time. Interestingly, disregarding the significant increase of δ_{99}/R during stage III, M and N are observed to be only a function of Re and do not depend on time.

An even clearer collapse within the boundary layer is obtained for the profiles of angular momentum

$$l^+ = \left\langle u_\varphi^+ \right\rangle \frac{r}{R} = \frac{l}{u_\tau R} \tag{3.16}$$

in viscous units, as shown in figure 3.12(b). Besides being constant throughout a range of wall-normal distances, l^+ is found to be approximately constant in time, indicating that $l \sim u_\tau$ during stage III." [Kaiser et al., 2020a]

The profiles of both $\left\langle u_\varphi^+ \right\rangle$ and l^+ at $Re \in \{3000, 6000, 28\,000\}$ are reported in Appendix B.

"In order to understand the effects of turbulence on the decay of the SBR core, the terms of the budget equations for K and k (§ 5.2.2) are studied for an early ($\Omega t = 9$) and a late ($\Omega t = 32$) phase of stage III. Again, normalisation with the

instantaneous wall units is adopted. Furthermore, the terms are pre-multiplied by the factor r/R to compensate for curvature effects and by y^+ to compensate for the use of a logarithmic scale [52]. Integrated over the cylinder volume, all transport terms are zero by definition. The aforementioned pre-multiplication allows one to capture this property visually in figure 3.13. As an additional benefit, this representation highlights the significant contribution of the outermost part of the boundary layer to the overall development of kinetic energy. Similarly to $\langle u_\varphi^+ \rangle$, the profiles only collapse in the near-wall region. Figure 3.13(a) shows the different terms of the K budget equation. Viscous dissipation ϵ_m mainly takes place in the viscous sublayer and the buffer region. The viscous transport term V_m transfers K from the outer buffer layer towards the wall. In the vorticity free region ($y^+ > 100$) all viscous terms except of ϵ_t are negligible and the transport of K and k from the vortex core towards the buffer region is mainly driven by turbulence (T_t and T_m). Starting from the buffer region ($y^+ > 5$), k is produced all through the boundary layer. In the logarithmic region, the sum $\Xi = P + \epsilon_t$ of production and dissipation of k tends towards a local excess of dissipation, in contrast to fully developed flat boundary layers [83]. While ϵ_m^+ is roughly unchanged between the two exemplary time instances, ϵ_t^+ increases, implying that the relative contribution of $[\epsilon_t]$ to the total dissipation $[\epsilon_{tot}]$ increases during stage III. An overview of the temporal evolution of the statistics shown in figures 3.11-3.13 is given in supplementary material [of [Kaiser et al., 2020a]] Movie3.mp4." [Kaiser et al., 2020a]

3.5.4 Stage IV: Vortex-core breakdown and decay of turbulence

"Regime III ends with the breakdown of the SBR core and the sudden increase of δ_{99} (figure 3.3(a)). Figure 3.14 shows three time instances during stage IV. The region of constant angular momentum ($\langle \omega_z \rangle \approx 0$) still exists during this flow stage. At the start of stage IV, $\langle u_\varphi \rangle$ at the interface between SBR and boundary layer is higher than in the initial condition, as indicated by the dashed circle in figure 3.3. Eventually, the velocity profile within the whole

(a) Averaged velocity profiles for different time instances during stage IV.

(b) Cumulative contribution $A(\cdot)$ of various terms to the K budget equation at the time instances shown in figure 3.14(a).
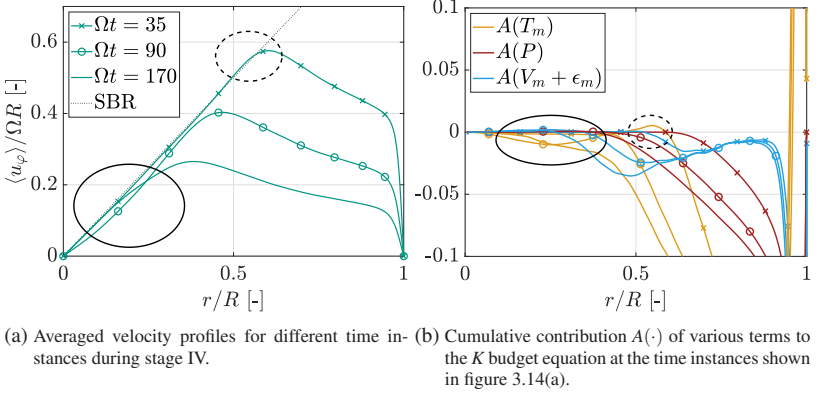
Figure 3.14: The line markers introduced in the legend of the panel (a) indicate different time instances. Results refer to the spin-down process at $Re = 12\,000$. Figure adapted from [Kaiser et al., 2020a].

SBR core substantially deviates from the initial condition, as indicated by the solid circle for the time instances $\Omega t = 90$ and $\Omega t = 170$. To understand how the breakdown of the SBR core occurs, the influence of the different K transport terms on the flow state at a time t is evaluated. The cumulative influence A of such terms is derived by integration of the respective term from $t = 0$ until the time t under consideration

$$A(T) = \frac{1}{\Omega^3 R^2} \int_{\tilde{t}=0}^{t} T \, \mathrm{d}\tilde{t} \qquad (3.17)$$

where T is a generic term in the K or k budget equation. Figure 3.14(b) shows A for the terms of the K budget equation at the same temporal instances shown previously in figure 3.14(a). Both the excess of mean kinetic energy at $\Omega t = 35$ as well as the decaying core flow can be clearly related to the turbulent transport term $A(T_m)$. At $\Omega t = 35$ fast fluid from the outer areas of the cylinder has been transported inwards by turbulent fluctuations, inducing larger $\langle u_\varphi \rangle$ in the SBR at the interface with the boundary layer. For the decaying core flow the mechanism is the opposite. $A(T_m)$ transports K from the core and towards
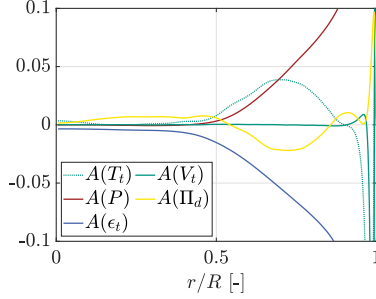
49

Figure 3.15: Cumulative contribution $A(\cdot)$ of various terms to the k budget equation at time instance $\Omega t = 90$ during stage IV ($Re = 12\,000$). Figure adapted from [Kaiser et al., 2020a].

the wall. The azimuthal velocity profile suggests that the boundary layer does not yet reach the core region. Yet there are enough fluctuations in the core to allow a significant transport of K (see also figure 3.10(b)). To understand how fluctuations reach into the SBR core, A is also determined for the terms of the k budget equation (figure 3.15). The influence of turbulent transport $A(T_t)$ on the propagation of k into the core flow is small. However, the impact of pressure diffusion $A(\Pi^d)$ is significantly larger and not-fully cancelled by $A(\epsilon_t)$.

Due to the closed geometry under consideration, the length scale of the boundary layer δ_{99} is bounded by the cylinder radius R and tops off with the breakdown of the vortex core. Moreover, after the transition to turbulence, the wall shear stress and the friction velocity continuously decrease. As time passes this leads to small Re_τ (figure 3.3(a)). While the ratio $[P]/[\epsilon_t]$ is approximately constant and equals unity during stage III of the spin-down process, the ratio decreases during the later phases of stage IV. As a consequence also $[k]$ starts to decline (figure 3.3(b)) and $[\epsilon_m]$ becomes the main contributor to $[\epsilon_{tot}]$ (see figure 3.4(b))." [Kaiser et al., 2020a]
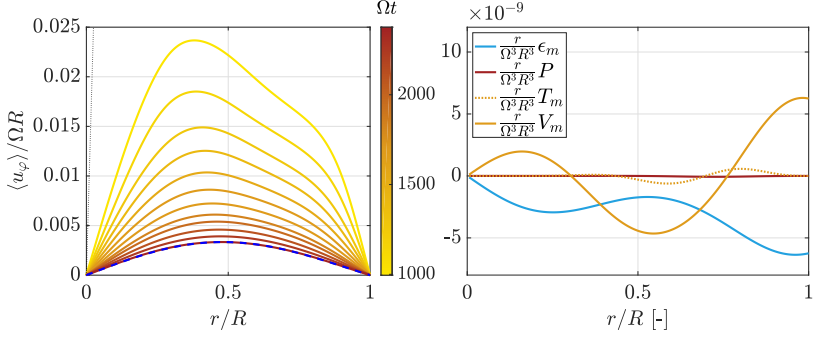
(a) $\langle u_\varphi \rangle$ in the transition from stage IV to stage V. Blue dashed line depicts the analytical solution of the laminar flow (3.12) for $\Omega t = 4430$, black dotted line represents the initial SBR.

(b) Instantaneous terms of the K budget equation after reentering the viscous state V at $\Omega t = 2400$.

Figure 3.16: Remlaminarisation after the decay of turbulence at $Re = 12\,000$. Figure adapted from [Kaiser et al., 2020a].

3.5.5 Stage V: Relaminarisation

"Eventually, $\langle k \rangle$ becomes negligible and the flow relaminarises. The temporal evolution of $\langle u_\varphi \rangle$ during transition from stage IV to V is shown in figure 3.16(a). The viscous nature of the flow is highlighted by means of the K budget equation for $\Omega t = 2400$, shown in figure 3.16(b). Both P and T_m are negligible compared to the other terms not involving turbulent quantities. With the decay of turbulence, the flow recovers the laminar state and $\langle u_\varphi \rangle$ approaches the analytical solution for the laminar flow u_φ^{lam}, given by (3.12) and visualised as a dashed blue line in figure 3.16(a). However, the effect of turbulent dissipation results in a temporal shift ΔT when $\langle u_\varphi \rangle$ is compared with the corresponding laminar solution u_φ^{lam}: $\langle u_\varphi \rangle (t) = u_\varphi^{lam}(t + \Delta T)$. As shown in figure 3.16(a), for $Re = 12\,000$ the present solution at time $\Omega t = 2400$ is compared to the laminar solution at $\Omega t = 4430$, which results in effective temporal shift of $\Omega \Delta T = 2030$." [Kaiser et al., 2020a]

3.6 Low *Re* scaling

The influence of varying *Re* on the spin-down process are discussed in the following. Various simple empirical models are derived. As the *Re*-range of the data is limited ($3000 < Re < 28\,000$), the models ought to be validated by experimental investigations for higher *Re* (see chapter 4).

"First, the *Re* scaling of the transition onset is addressed and compared to classical Taylor-Couette flow in § 3.6.1. Second, the *Re*-dependent effects of transition on the evolution of δ_{99} are evaluated in § 3.6.2 before the influence of *Re* on the evolution of Re_τ is discussed in § 3.6.3. Furthermore, the scaling of energy decay (both $[K]$ and $[k]$) is analysed in § 3.6.4." [Kaiser et al., 2020a]

In addition, a *Re*-independent flow feature is investigated in detail. The region of constant angular momentum, which exists for all investigated *Re*, is utilised to model the flow as a Rankine vortex during stage III (§ 3.6.5). The constant angular momentum l^+ is then used to derive a model for the evolution of u_τ. Finally, in § 3.6.6 the *Re* scaling of the vorticity annihilation process is addressed and its effect on the pressure distribution is discussed.

3.6.1 Critical Taylor number

"In TC flow with a gap width *d*, a resting outer cylinder and a rotating inner cylinder of radius R_i (angular velocity Ω_i) the onset of Taylor rolls typically occurs for a characteristic Taylor number [30] of

$$Ta_{tc} = \frac{\Omega_i d R_i}{\nu} \sqrt{\frac{d}{R_i}} \approx 41.2\,.\qquad(3.18)$$

In contrast, the stability of the spin-down flow is usually described by a critical time θ_c and a critical wavelength λ_c. The critical values can be obtained by stability analysis as performed by Neitzel [96] and Kim & Choi [61], which showed good agreement with present DNS results as reported in § 3.5.2.

For the sake of comparison between TC and spin-down flow, the critical time θ_c of the spin-down problem can also be translated into a Taylor number. Defining the SBR core as the inner cylinder and δ_{99} as the gap width, the spin-down Taylor number results in

$$Ta = \frac{\Omega \delta_{99}^{3/2}(R - \delta_{99})^{1/2}}{\nu}.$$ (3.19)

Note that different flow events and their respective onset time can be analysed and related to a Taylor number. Examples include the visual onset of instabilities [28] or the time where the energy of the critical wavelength λ_c first starts to increase. However, for the following evaluation, the critical time θ_c is utilised, that was obtained by the propagation theory of Kim & Choi [61]. Here, θ_c is the point in time at which the energy growth rate of the most amplified disturbance is larger than the energy decay rate of the base flow. Its *Re*-dependence can be approximated by

$$\theta_c = \frac{\nu t_c}{R^2} = 9.4 Re^{-4/3},$$ (3.20)

if *Re* is large enough. Equation (3.20) is inserted into the approximate expression for δ_{99} (see (3.14)) to provide the critical boundary-layer thickness $\delta_c \approx 11.28 R \cdot Re^{-2/3}$, which plugged into (3.19) leads to the critical Taylor number

$$Ta_c \approx 37.9 \sqrt{\frac{R - \delta_c}{R}} = 37.9 \sqrt{1 - 11.28 Re^{-2/3}}.$$ (3.21)

Thus, similar to TC flow also for the spin-down problem a Taylor number Ta_c can be formulated, that is related to the onset of Taylor rolls. Ta_c tends to the constant value 37.9 for $Re \to \infty$." [Kaiser et al., 2020a]

3.6.2 Boundary-layer thickness

"Figure 3.17(a) presents the evolution of δ_{99} for different *Re*. The value of δ_{99} collapses for all *Re* during the laminar stage if time is expressed in units

(a) Temporal evolution of δ_{99} at different values of Re (colour-coding as in figure 3.18).

(b) Ratio a_{turb}/a_{lam} at different values of Re. A least-squares fitted power-law is indicated by the dashed line.
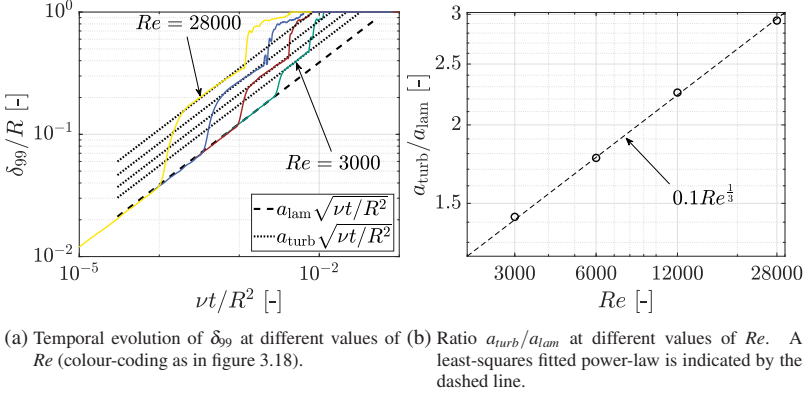
Figure 3.17: Scaling of the boundary-layer thickness evolution $\delta_{99}(t)$ for different Re. δ_{99} grows proportionally to $\sqrt{\nu t}$ with the proportionality constant a_{lam} during the laminar stage (stage I) and a_{turb} during the sustained turbulent stage (stage III). Figure adapted from [Kaiser et al., 2020a].

of $\nu t/R^2$. The thickness of the laminar boundary layer grows as described by (3.14) proportionally to $\sqrt{\nu t}$ with a proportionality constant $a_{lam} \approx 3.68$, until Taylor rolls start to emerge. The onset of Taylor rolls happens at an earlier time and thus at lower value of δ_{99} with increasing Re. During stage II the fast increase of δ_{99} is related to the growth of radial plumes as discussed in figure 3.7(d) in § 3.5.2. Subsequently, the growth of the plumes becomes nonlinear and eventually ceases. Secondary instabilities appear and initiate the breakdown to turbulence. Also in the turbulent flow of stage III the boundary layer grows approximately proportionally to $\sqrt{\nu t}$ (figure 3.17(a)), albeit with a different and Re-dependent proportionality constant $a_{turb} = a_{turb}(Re)$. The ratio a_{turb}/a_{lam} is plotted in figure 3.17(b) for different values of Re. Utilising the present results, the ratio of these two quantities can be linked to Re by the empirical correlation

$$a_{turb}/a_{lam} = 0.1Re^{\frac{1}{3}} ."$$

(3.22)

[Kaiser et al., 2020a]

3.6.3 Friction Reynolds number Re_τ

"Figure 3.18 shows the temporal history of Re_τ for each value of Re consid-
ered in the present study. As expected, larger peak values of Re_τ correspond
to larger values of Re. For the same total energy of the initial perturbations, a
larger Re lead to an earlier onset of the primary centrifugal instability so that
stage II is entered at an earlier time which also yields a smaller value of δ_{99}.
For the two smallest values of Re considered in the present work, the simul-
taneous increase of δ_{99} and decrease of u_τ result in an almost constant value
of Re_τ during the boundary-layer growth with an intact vortex core in stage
III. For larger values of Re, however, the growth of δ_{99} increasingly outweighs
the decrease of u_τ, resulting in a mild increase of Re_τ during phase III. The
breakdown of the vortex core, which marks the beginning of stage IV and the
related sudden increase of δ_{99}, is associated with the peak values of Re_τ for all
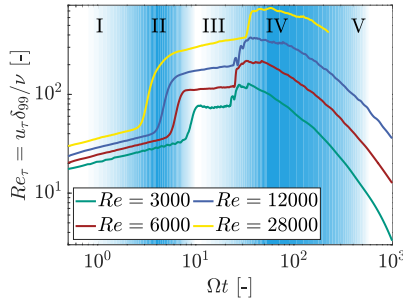considered values of Re. This is a consequence of the boundary-layer thick-

Figure 3.18: Temporal development of Re_τ for different Re in the range of $3000 < Re < 28\,000$.
Two steep gradients can be detected for each Re. The first gradient corresponds to
the primary and secondary instability, followed by the transition to turbulence (start
of stage II). The second gradient corresponds to the breakdown of the SBR core (start
of stage IV). Figure adapted from [Kaiser et al., 2020a].

ness being bounded by the cylinder radius ($\delta_{99}/R = 1$) and the monotonically decreasing u_τ." [Kaiser et al., 2020a]

3.6.4 Decay of kinetic energy

"The decay of $[K]$ and $[k]$ at different *Re* is shown in figure 3.19. The data is normalised by the volume-averaged total kinetic energy of the initial condition $[K_0] = [K](t = 0) = 1/4$, which is identical for all considered *Re*. The temporal evolutions of $[K]$ and $[k]$ are presented with a logarithmic (figures 3.19(a) & 3.19(c)) and a linear timescale (figures 3.19(b) & 3.19(d)) to emphasise the early and the later stages of the decay, respectively. Different non-dimensional time units are used, which are related by $\Omega t = Re \cdot \frac{\nu t}{R^2}$.
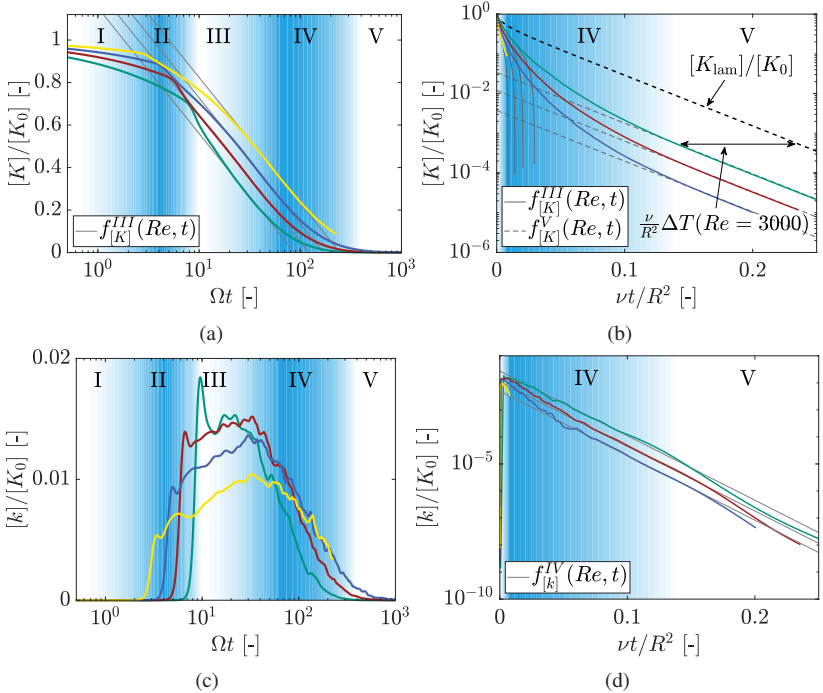
Figure 3.19: Temporal development of (a,b) $[K]$; and (c,d) $[k]$ at different values of *Re* (colour-coding as in figure 3.18). Roman numbers $I - V$ and the background highlight the different stages of the decay.

The larger the value of Re, the slower the decay of $[K]$ in units of Ωt, due to the expected less dominant role of viscosity; see figure 3.19(a). There is a clearly noticeable increase in the decay rate (i.e. the negative slope) of $[K]$ when Taylor rolls emerge and the flow transitions to turbulence during stage II. Towards the end of stage III the decrease of $[K]$ follows a logarithmic decay for all cases, which can be described by

$$f_{[K]}^{III}(Re,t) = -h_{[K]} \cdot \log(\Omega t) + g_{[K]}(Re), \qquad (3.23)$$

where $h_{[K]}$ is constant and $g_{[K]}(Re)$ depends on Re. The fact that the logarithmic decay of equation (3.23) is either approached from larger (low Re) or lower (high Re) values of $[K]$ is best understood by considering the temporal evolution of $[k]$ shown in figure 3.19(c). Note that the initial decrease of $[k]$ before the onset of primary instability, which was previously discussed in the context of figure 3.3(b), is not visible here due to the linear scale. For all considered values of Re, the emergence of Taylor rolls with the primary instability yields the visible strong increase of $[k]$ and results in the peak of $[k]$ at the end of stage II. In particular, the peak of $[k]$ is larger for lower values of Re, due to the larger radial extent of the Taylor rolls before secondary instabilities occur. In fact, the larger the size of the Taylor rolls, the larger the amount of kinetic energy the Taylor rolls can extract from $[K]$ and redistribute into $[k]$ in form of streamwise vortices. Therefore, a faster decay of $[K]$ at the beginning of stage III is observed for lower Re, until the logarithmic decay of (3.23) is approached at approximately $\Omega t = 20$. The value of $[k]$ grows slowly during stage III for all Re considered in the present study. Yet the growth is more pronounced for the larger Re cases. As a result, except at $Re = 3000$, the global maximum of $[k]$ is not given by the peak of stage II but occurs later on during stage III. The relative importance of the two mechanisms of $[K]$ conversion, via the initial Taylor rolls and via turbulence, determines how the logarithmic decay of $[K]$ (3.23) is approached; see figure 3.19(a).

The decay of $[k]$ during the late portion of stage IV exhibits an exponential character as shown in figure 3.19(d). The decay can be described by

$$f_{[k]}^{IV}(Re,t) = g_{[k]}(Re) \cdot \exp(-h_{[k]} \cdot \nu t / R^2),\qquad(3.24)$$

where $h_{[k]}$ is constant and $g_{[k]}(Re)$ depends on *Re*. Once $[k]$ is small enough, a laminar velocity profile u_φ^{lam} is recovered; see § 3.5.5. This leads to the collapse of the data with the kinetic energy of the laminar solution

$$[K_{lam}] = \frac{1}{2V\Omega^2 R^2} \int_V (u_\varphi^{lam})^2 dV \qquad(3.25)$$

in stage *V*, if the latter is shifted by a *Re*-dependent $\Delta T = \Delta T(Re)$ (see figure 3.19(b)):

$$f_{[K]}^V = \frac{[K_{lam}](t + \Delta T(Re))}{[K_0]}.\qquad(3.26)$$

Note that the decay of $[K_{lam}]$ and as such also of $[K]$ is approximately exponential for large t (3.12)." [Kaiser et al., 2020a]

3.6.5 Rankine-vortex analogy

"For all investigated *Re*, three distinct regions can be distinguished in the radial profile of $\langle u_\varphi \rangle$ during stage III: the region of SBR, the region of spatially constant angular momentum ($\langle \omega_z \rangle = 0$, $l = l(t)$) and the shear layer at the wall. These are visualised in figure 3.20(a). The two innermost regions of the $\langle u_\varphi \rangle$ profile are well approximated by a Rankine vortex

$$\langle u_\varphi^{ran} \rangle(l,r) = \begin{cases} \Omega r & \forall r \le \sqrt{l/\Omega} \\ l/r & \forall r > \sqrt{l/\Omega} \end{cases},\qquad(3.27)$$
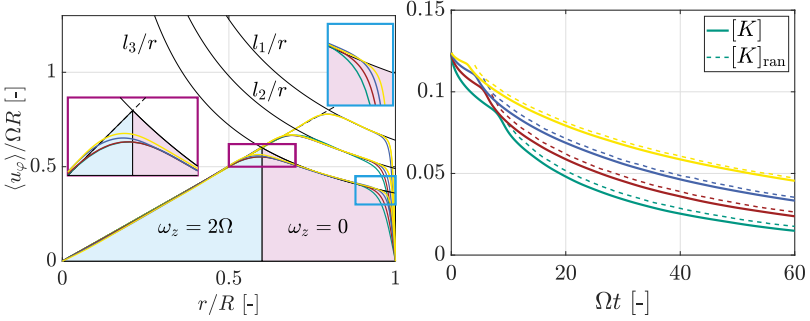
(a) Velocity profiles $\langle u_\varphi \rangle$ at different values of Re are compared against the velocity profile of a Rankine vortex u_φ^{ran}. Insets show close-ups of the regions, where u_φ^{ran} deviates most significantly from $\langle u_\varphi \rangle$.

(b) Temporal evolution of $[K]$ at various Re for the actual $\langle u_\varphi \rangle$ profile (solid line) and its Rankine vortex approximation $[K]_{ran}$ (dashed lines).

Figure 3.20: Modeling the velocity profile in stage III as a Rankine vortex for different Re (colour-coding as in figure 3.18). The irrotational part of u_φ^{ran} in (a) is chosen to match the angular momentum l of the $\langle \omega_z \rangle \approx 0$ portion of $\langle u_\varphi \rangle$. Temporal instants corresponding to three different values of $l \in \{l_1, l_2, l_3\}$ are indicated with a subscript. Figure adapted from [Kaiser et al., 2020a].

with angular momentum l in its irrotational portion chosen to match the $\langle \omega_z \rangle \approx 0$ portion of $\langle u_\varphi \rangle$.

Rankine vortices at three different values of $l = l_i$ are presented in figure 3.20(a). At each value of l_i a matching time instance is selected for each of the four investigated Re. As expected, the velocity profiles almost collapse. Only near the wall and at the interface between the region of SBR and $\langle \omega_z \rangle = 0$ the profiles differ (see close ups in figure 3.20(a)). With increasing Re, the error made by the Rankine-vortex approximation decreases, as shown exemplarily for $[K]$ and its approximation K_{ran} estimated with (3.27) in figure 3.20(b). This bears particular potential for experimental investigations, as now $\langle u_\varphi \rangle$ and the connected quantities (i.e. angular momentum and K) can be estimated by determining the temporal velocity development $\langle u_\varphi \rangle (r_1, t)$ at a single radial position r_1 inside the region of constant angular momentum." [Kaiser et al., 2020a]
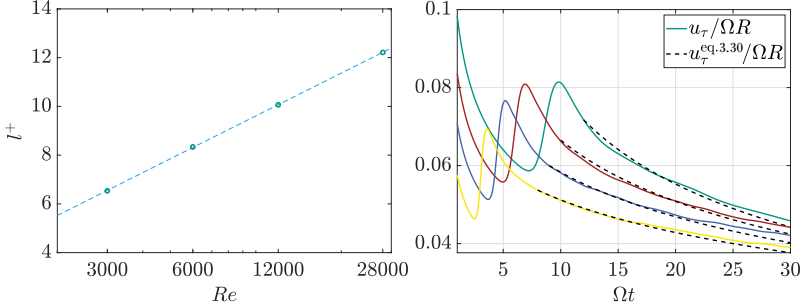
(a) Magnitude of the angular momentum $l^+(Re)$ in the region where $\langle \omega_z \rangle \approx 0$ during stage III for different Re. Dashed blue line: fitted correlation approximating $l^+ = g_{l+}\ln(Re) + h_{l+}$.

(b) Temporal evolution of friction velocity u_τ compared to the model given by (3.30). Colour-coding of the different Re in (b) as in figure 3.18.

Figure 3.21: Scaling of $l^+(Re)$ and modeling of the temporal evolution of u_τ.

In the following, the Rankine model is combined with the averaged angular momentum equation (see e.g. [125]) and the observation of a constant l^+ for each Re (see § 3.5.3) to derive an ordinary differential equation for u_τ. For the present flow the integral form of the angular momentum equation in azimuthal direction simplifies to

$$\frac{\mathrm{d}}{\mathrm{d}t} \int_0^R \langle u_\varphi \rangle r^2 \mathrm{d}r = -u_\tau^2 R^2 . \tag{3.28}$$

The combination of the rankine model (3.27) and the angular momentum equation (3.28) leads to

$$\frac{\mathrm{d}}{\mathrm{d}t} \left[\frac{lR^2}{2} - \frac{l^2}{4\Omega} \right] = -u_\tau^2 R^2. \tag{3.29}$$

As described in § 3.5.3, the value of angular momentum $l^+(Re) = l/(u_\tau R)$ (see (3.16)) in viscous units is constant in time during stage III and only depends on Re. The values of $l^+(Re)$ are extracted from figure 3.12(b) (at $Re = 12\,000$) and Appendix B (at all other Re) and follow a logarithmic trend in the investigated Re range, as shown in figure 3.21(a). Equation (3.29) can

be reduced to a non-linear ordinary differential equation for u_τ by substituting l^+ in place of l as follows

$$\frac{\mathrm{d}}{\mathrm{d}t}\left[\frac{l^+ u_\tau R}{2} - \frac{(l^+)^2 u_\tau^2}{4\Omega}\right] = -u_\tau^2 R^2. \qquad (3.30)$$

Figure 3.21(b) compares the numerical data to the solution of (3.30) for various Re. The accordance between (3.30) and the numerical results increases with Re, as diminishing viscous effects increase the accuracy of both the Rankine model and the assumption that l^+ is constant in time.

3.6.6 Cross-annihilation of vorticity and the pressure distribution

After the cylinder walls are impulsively stopped no further vorticity is introduced at the side walls [94]; see also § 2.1.2. Thus, the overall circulation in axial direction is zero at all times

$$\Gamma = 2\pi \int_{r=0}^{R} \langle \omega_z \rangle r \mathrm{d}r = 0 \quad \forall t > 0. \qquad (3.31)$$

However, at $t = 0$ all negative vorticity is in an infitisimally small layer at the wall. During spin-down the negative vorticity diffuses into the core until eventually $\langle \omega_z \rangle = 0$ for all r when the flow is at rest. This implies that there is a temporally decreasing amount of positive vorticity in the core of the cylinder. The core circulation is defined as the accumulation of all remaining positive vorticity

$$\Gamma_c = 2\pi \int_{r=0}^{R_c} \langle \omega_z \rangle r \mathrm{d}r, \qquad (3.32)$$

where R_c is the radius at which $\langle \omega_z \rangle (r = R_c) = 0$. On a viscous time scale vt/R^2 (figure 3.22(b)) the earlier onset of turbulence leads to a faster decay of Γ_c for high Re. On the outer time scale Ωt (figure 3.22(a)), the issue is more complex. A smaller Re leads to a faster decay of Γ_c due to more pro-

(a) Time normalised as Ωt.
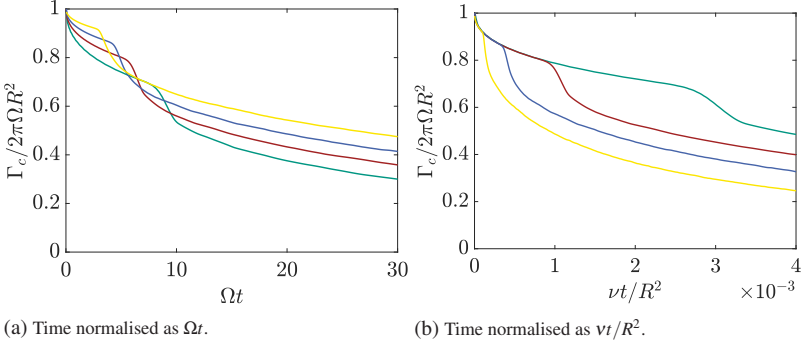
(b) Time normalised as $\nu t/R^2$.

Figure 3.22: Decay of core circulation Γ_c for different *Re* and distinct normalisations of t. Colour-coding of the different *Re* as in figure 3.18.

nounced viscous effects during the laminar stage. However, this is (in parts) compensated for by earlier transition for high *Re*. For example, Γ_c is almost identical for $Re = 3000$ and $Re = 28\,000$ for $7 < \Omega t < 9$, despite *Re* differing almost one order of magnitude. In regards to the guiding example of this thesis, the similar evolution of Γ_c is particularly interesting, as it could motivate the limited *Re* scaling of vortex formation in animal locomotion reported by Taylor [129]. The statement that *Re* has small effects should, therefore, be clarified: *Re* scaling has two distinct effects (viscous diffusion and transition) which compensate at therefore lead to similar behaviour for a wide range of *Re*. Note, however, that if a vortex, which is used to obtain lift or thrust is stabilised on a propulsor for a long period of time $\Omega t > 10$ a *Re* scaling effect is likely to become more apparent (cp. figure 3.22(b)).

The vorticity annihilation process leading to the decay of core circulation Γ_c also influences the pressure distribution inside the vortex. Figure 3.23 shows the spatially averaged pressure distribution

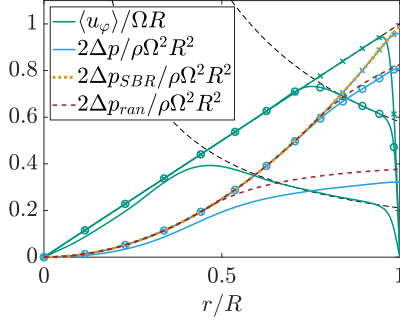$$\Delta p(r) = \langle p \rangle (r) - \langle p \rangle (r = 0) \tag{3.33}$$

Figure 3.23: Azimuthal velocity profiles and the pressure difference Δp between the center of the cylinder and the wall at $Re = 12\,000$ at three different time instances $\Omega t = 2.0$ (x-shaped markers, stage I), $\Omega t = 11.3$ (circular markers, stage III), $\Omega t = 93.5$ (no markers, stage IV). The distribution of Δp is compared to its approximations by Δp_{SBR} and Δp_{ran}.

and the respective azimuthal velocity profile $\langle u_\varphi \rangle$ at $Re = 12\,000$ and at three time instances. During the laminar stage and when the boundary-layer thickness is relatively small and the pressure distribution of an SBR proves to be a good approximation

$$\Delta p_{SBR} = \langle p \rangle (r) - \langle p \rangle (r = 0) = \frac{\rho \Gamma_c^2 r^2}{8\pi^2 R^2}. \tag{3.34}$$

However, with increasing boundary-layer thickness the agreement between the SBR approximation and the real pressure distribution decreases. Yet again, in stage III the Rankine-vortex approximation provides a good model for pressure distribution. The pressure inside the Rankine vortex [42] is given by

$$\Delta p_{ran}(r) = p_{ran}(r) - p_{ran}(r = 0) = \frac{\rho \Gamma_c^2}{8\pi^2} \begin{cases} \frac{r^2}{R_c^4} & \forall\, r < R_c \\ \frac{2}{R_c^2} - \frac{1}{r^2} & \forall\, r > R_c. \end{cases} \tag{3.35}$$

R_c is well approximated by the intersection of a potential vortex fit in the region of constant angular momentum and the initial SBR, leading to

$$R_c = \sqrt{l/\Omega}. \tag{3.36}$$

As positive vorticity predominately exists inside the SBR (cp. figure 3.11(b)), Γ_c can be approximated by

$$\Gamma_c = 2\Omega\pi R_c^2 = 2\pi l. \tag{3.37}$$

The application of the aforementioned approximations to (3.35) simplifies the expression to

$$\Delta p_{ran}(r) = p_{ran}(r) - p_{ran}(r=0) = \rho \begin{cases} \frac{\Omega^2 r}{2} & \forall\, r < R_c \\ \Omega l - \frac{l^2}{r^2} & \forall\, r > R_c, \end{cases} \tag{3.38}$$

which shows good agreement with the numerically obtained pressure distribution $\Delta p(r)$ during stage III as presented in figure 3.23 (circular markers). However, as expected, for $\Omega t = 93.5$ (stage IV) the corrupted SBR leads to a significant deviation of numerical data and Rankine model. The simplified expression for Δp_{ran} provides a relation of angular momentum l and the pressure difference between the cylinder wall and the center of the cylinder

$$\Delta p_{ran}(r=R) = \rho \left(\Omega l - \frac{l^2}{R^2} \right), \tag{3.39}$$

for all time instances during stage III. Figure 3.24 compares the temporal evolution of the modelled pressure difference $\Delta p_{ran}(r=R)$ to the numerical data $\Delta p(r=R)$. Similar to Γ_c (cp. figure 3.22(a)) on the outer time scale Ωt (figure 3.24(a)) also for $\Delta p(r=R)$ the transition to turbulence compensates in parts for the different impact of viscosity at varying *Re*.
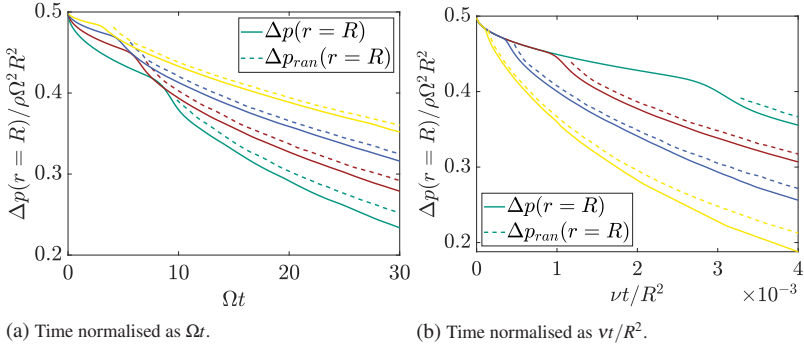
(a) Time normalised as Ωt.

(b) Time normalised as $\nu t/R^2$.

Figure 3.24: Decay of Δp for different Re and distinct normalisations of t. Colour-coding of the different Re as in figure 3.18.

3.7 Summary

In this chapter the results of a DNS, which covered a complete spin-down from SBR, are presented.

"The generated data, which cover almost a decade of Reynolds numbers up to $Re = 28\,000$, allow for the observation of five different flow stages (I−V) during the decay of the initial SBR, each entailing its own characteristic phenomena. The following describes these five stages:

Numerical experiments over almost a decade of Re were performed. Evaluation of the spin-down process showed five distinct flow stages (I−V). The flow phenomena that occur during those stages are summarised in the following:

I. In the first stage of spin-down a laminar boundary layer, similar to Stokes' first problem, grows at the cylinder walls.

II. The formation and merging of Taylor rolls following linear and non-linear growth of a primary centrifugal instability is the characteristic phenomenon of stage II. This causes a fast increase in boundary-layer thickness δ_{99}, which is associated with a simultaneous shift of the dominant axial wavelength in the energy spectra. The subsequent transi-

tion to turbulence, initiated by secondary shear instabilities, is analysed by means of LCS. Hereby, the streamwise endpoints of the elongated streamwise vortices (Taylor rolls) are identified as the origin of evolving hairpin-like vortices and thus as the nucleus of transition. Larger values of the global Reynolds number Re are associated with earlier transition and smaller wavelengths of the primary instability. As such, the maximum of kinetic energy accumulated in the Taylor rolls decreases with increasing Re.

III. Once transition to turbulence is completed, the boundary-layer flow is turbulent while the retracting SBR vortex core is still intact. Therefore, the flow resembles turbulent TC flow between two concentric rotating cylinders, in which the inner cylinder in TC flow represents the SBR core in the present case. However, the unique feature of the present flow is that the radius of the SBR core varies in time, due to the growth of the boundary layer. In addition, turbulent fluctuations are allowed at the interface with the SBR core, whereas in TC flow a no-slip condition exists at the inner cylinder.

Interestingly, in the investigated Reynolds number range, δ_{99} still grows at the laminar growth rate $\sqrt{\nu t}$, albeit with a different constant of proportionality. The simultaneous increase of δ_{99} and decrease of u_τ lead to a negligible temporal variation of Re_τ and thus to a collapse of turbulence statistics in the near-wall region. In addition, the outer boundary layer organises as dictated by the marginal stability criterion [107]. A slowly growing region of constant angular momentum $l = u_\varphi r$ forms, so that the mean velocity profile is well approximated by an appropriately defined Rankine vortex. It is found that the angular momentum $l^+ = (r/R)\langle u_\varphi^+ \rangle$ in viscous units is constant in time. Similarly, the constants M and N describing the logarithmic behaviour of $\langle u_\varphi^+ \rangle$ do not vary significantly during stage III, despite significant changes of the lo-

cal curvature δ_{99}/R in the boundary layer. During stage III and the early stage IV a logarithmic decay of $[K]$ is observed.

IV. Eventually, the SBR core breaks down. Applying a temporal integration of k and K budget equations, the mechanism behind the core breakdown is identified: the pressure diffusion term Π_d transports fluctuations into the core region. These fluctuations in turn transport K from the core into the boundary layer (term T_m). Towards the end of stage IV turbulent dissipation ϵ_t overtakes its production P and $[k]$ starts to decrease exponentially.

V. As $[k]$ diminishes, laminar flow is recovered and the velocity profile collapses with the analytical solution [96]. The net effect of transition and turbulence can be lumped into a single parameter, namely the temporal shift $\Omega\Delta T$ that needs to be added to the laminar solution in order to match the velocity profile of the actual flow." [Kaiser et al., 2020a]

4 Wall-bounded vortex decay – experimental approach

The in-depth analysis of DNS data in chapter 3 provides insights into the flow phenomena occurring during the wall-bound decay of an idealised vortex in SBR. In particular, § 3.6 discusses the Re scaling of the spin-down and formulates several scaling laws, which are valid for the limited Re range provided by the numerical simulations ($3000 < Re < 28\,000$). However, despite the efficient spectral code used to produce the results of chapter 3, the range of Re in DNS is still fairly limited by today's computational resources. Thus, the present chapter strives to extent the Re range experimentally up to $Re = \Omega R^2/\nu = 4 \cdot 10^6$ in order to elaborate whether the suggested scalings also hold up to very high Re. In particular, the following questions are addressed in this chapter:

- Very high values of Re result in small δ_{99}/R during the growth of the primary instability, and thus a diminishing influence of curvature. In TC flow the narrow-gap limit with negligible curvature converges towards the linearly stable Couette flow. However, for the present spin-down case, Stokes' first problem is approached when δ_{99}/R is very small during transition. As such, for very large Re, Tollmien–Schlichting waves [81] could originate before or simultaneously with the centrifugal instability. It is thus of interest, which instability mechanisms triggers the transition to turbulence.

- The prediction of transition of Kim & Choi [61] holds for the Re range addressed in chapter 3. The present chapter strives to validate the scaling for very high Re.

- The scaling law for the boundary-layer growth due to the transition process a_{turb}/a_{lam} (3.22) is tested for a significantly wider range of Re as in chapter 3.

However, the design of an experiment, which allows to investigate the aforementioned statements, proves to be challenging and is therefore also discussed in detail. In contrast to the numerical implementation of the spin-down, where axially periodic boundary conditions mimic an infinitely long cylinder, end-wall effects and/or a free surface are inevitably present in an experimental implementation of the flow. The fluid in a cylinder of filling height H is bounded by a bottom wall and either a top wall or a free surface. End-wall/free-surface effects influence the flow and might falsify any attempts to evaluate the aforementioned Re scaling experimentally. Literature on the influence of the end wall and a free surface is reviewed in § 4.1. Subsequently, a method is suggested, which reduces the end-wall influence: A saturated salt-water layer is introduced at the bottom of the cylinder. To address the Re scaling experimentally, two consecutive experimental campaigns were performed.

First, the feasibility of experiments on such a complex and unsteady flow is tested in a small-scale campaign performed in a 0.49 m diameter acrylic glass cylinder filled with distelled water; see § 4.2. The measurement technique at hand – particle image velocimetry (PIV) – is shown to be capable of extracting the unsteady statistical properties of the spin-down. In addition, the suitability of a salt-water layer to reduce end-wall effects is tested.

Second, the insights gained in the small-scale experiment are utilised to design a large-scale campaign, which is realised at the CORIOLIS II platform in Grenoble, France. The 13 m diameter platform allows measurements at very high Re while allowing a high temporal and spatial resolution in normalised units (r/R for space and $\nu t/R^2$ for time). Multiple PIV measurements are performed in parallel to capture various aspects of the flow: The scaling of both, the transition process as well as the boundary-layer growth are assessed. Furthermore, the high-Re behavior of the logarithmic region is investigated.

Note that preliminary results of the present chapter were partially reported in [Kaiser et al., 2016], [von der Burg et al., 2017], and [Kaiser et al., 2017]. Adapted figures and paraphrased quotations are highlighted. Furthermore, the following student theses contributed to the evaluation of the data presented in this chapter: [Wah16], [Sch17], [vdB17], and [Oßw18].

4.1 End-wall and free-surface effects

4.1.1 Background

Besides the side-wall boundary layer with thickness δ_{99} and the bulk flow in SBR a third flow region is present in the experimental setup: an end-wall boundary layer (Ekman boundary layer [24]); see figure 4.1. In the Ekman layer the inequality of centrifugal forces and pressure forces leads to a radial acceleration of the flow. For the present spin-down case this boundary layer is also referred to as Bödewadt layer [136]. The end-wall boundary layer also
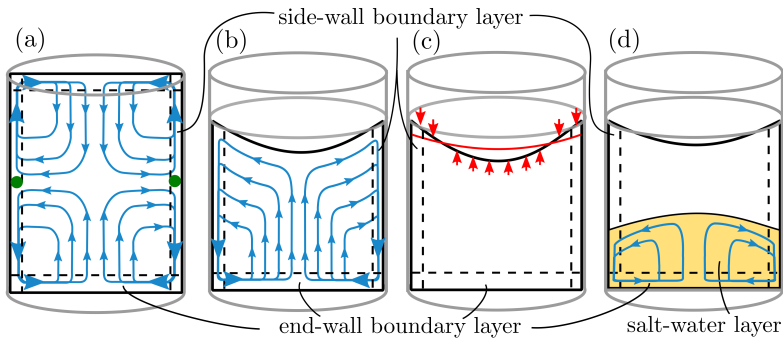
Figure 4.1: Spin-down: (a) Ekman pumping in a closed cylinder with the position of first occuring Rayleigh instability during non-linear spin-down (green dots) as presented by [97]; (b) Ekman pumping in a free-surface configuration; (c) free surface effects as investigated by [82]. Black and red line highlight the surface shape before spin-down and at a later time during spin-down, respectively; and (d) Ekman pumping confining salt-water layer (orange).

71

affects the bulk flow as slow fluid is ejected from the near-wall region into the bulk and hereby provides an additional convective decay mechanism that leads to a faster decay of the SBR; see figure 4.1a. This additional decay mechanism is often referred to as Ekman pumping.

For very small absolute values of the Rossby number

$$Ro = \Delta\Omega/\Omega, \tag{4.1}$$

the linearisation of the swirl equation leads to an approximate analytical solution of the flow [43]. The value of $\Delta\Omega$ hereby describes the change of rotational speed of the cylinder, while Ω is its initial rotational speed.

The effects on linear and slightly non-linear spin-up and spin-down of closed cylinders are comprehensively reviewed by Benton & Clark [6] and Duck & Foster [23]. Even though the present experiment is in the highly non-linear and turbulent regime, the investigations on linear spin-down yet provide valuable insights on the properties and formation of the Ekman layer and are therefore briefly summarised in the following.

First, in case of linear spin-down the formation time of the Ekman layer is delayed to approximately $\Omega t = 1$. Second, for linear spin-down the time scale of the spin-down due to Ekman pumping is $t_E = \Omega^{-1}Ek^{-1/2}$, where the Ekman number

$$Ek = \frac{\nu}{\Omega H^2} \tag{4.2}$$

describes the relative impact of viscous forces to Coriolis forces. The ratio between t_E and the time scale of laminar decay of the vortex due to the side-wall boundary layers $t_D = R^2/\nu$ is given by $t_E/t_D = Ek^{1/2}(H/R)^2$. This implies that (for linear spin-down) only in case of large aspect ratios $A = H/R$ the decay rate of the side wall boundary layer is much faster and thus roughly unaffected by the Ekman pumping.

To further reduce the effects of the Ekman layers, the experiment can be performed in a free-surface configuration. The impact of the free surface can be described by the ratio of intertial (centrifugal) forces and gravitational forces; i.e. the Froude number

$$Fr = \frac{\Omega^2 R^2}{gH}.$$

(4.3)

In the linear regime, the combined effects of removing the top-wall Ekman layer (see figure 4.1(b)) and the surface deformation during spin-down (see figure 4.1(c)) increases the Ekman time scale t_E by a factor $1 + \frac{1}{2}Fr$ [82, 98]. Note that while high Fr counteract the effects of Ekman pumping, the free-surface deformation could possibly introduce its own (unwanted) three-dimensional vortex stretching effects. At higher Ro but yet small Re, the linear theory has been extended to the non-linear regime [44, 133, 137, 138]. However, this still does not provide an accurate description of the present problem, as the non-linear theory only applies until one of the boundary layers becomes unstable. Besides the well-known Rayleigh instability at the side walls (see chapter 3), two distinct spiral instability modes were identified in the end-wall boundary layer, commonly referred to as Type I (Class B) and Type II (Class A) modes [79, 80, 113]. Note that the different instability mechanisms do not occur independently: The convection caused by the end-wall boundary layer can trigger the side wall instability as presented by Neitzel & Davis [97] and highlighted by a green dot in figure 4.1(a).

4.1.2 Approaches to reduce end-wall and free-surface effects

The present section reviews various approaches to minimise end-wall and free surface effects. In particular, the scalability of the approaches is evaluated concerning safety and costs. The obvious measure to achieve quasi two-dimensional vortex decay would be very high A [28, 86] to reduce Ekman pumping and small Ω and large R to minimise free surface effects

($Fr = \Omega^2 R^2 / gH$) while still achieving high $Re = \Omega R^2 / \nu$. As large R and A are requirements that are in direct contrast to the requirements of an affordable high-Re experiment, alternative approaches have to be considered.

Burin *et al.* [15] reduced Ekman-pumping successfully by splitting the end-walls into multiple slices that can be rotated and controlled interdependently. Yet again, a physical implementation of this multi-disc approach in a large scale facility (such as the aforementioned CORIOLIS II platform) would come with high costs and is thus not further considered in the following.

An alternative approach was first suggested by Pedlosky [104]. Two immiscible fluid layers of different density are filled into the cylinder. If the top of the upper layer is confined by a free surface, linear theory [104] predicts that the effects of Ekman pumping on the upper layer are significantly reduced. Experimental investigations (on spin-up) [99] validated the theoretical results. The scale of a large scale and high-Re experiment excludes hazardous or expensive fluids as possible liquids. Therefore, a saturated salt-water solution (density $\rho_s \approx 1.2 \, \frac{\mathrm{g}}{\mathrm{cm}^3}$ at 20°C [130]) is selected as the high-density fluid, while the measurements are performed in a water layer (density $\rho_w \approx 1.0 \, \frac{\mathrm{g}}{\mathrm{cm}^3}$ at 20°C [130]). Even though linear theory does not apply at high Re, it is hypothesised that also for the highly non-linear spin-down, the Ekman pumping is confined to the salt-water layer as depicted in figure 4.1(d). Note that the faster decay of the salt-water layer leads to an inverse parabola at the interface between the fluids. The applicability of this mechanism to reduce end-wall effects is investigated in the following. First, the background is elaborated in § 4.1.3, before the effect is further discussed alongside experimental investigations in sections 4.2.3 and 4.2.4.

4.1.3 Salt-water layer: parabola and interface stability

Two requirements have to be met for the salt-water layer to reduce end-wall effects. First, the upper water layer should not reach the bottom wall during all stages of the spin-down. Linden & van Heijst [76] reported the occurrence of
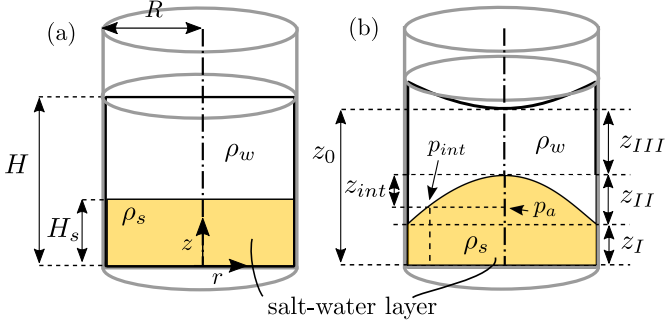
Figure 4.2: Spin-down: (a) Ekman pumping in a closed cylinder with the position of first occuring Taylor rolls during non-linear spin-down (green dots) as presented by [97]; (b) Ekman pumping in a free-surface configuration; (c) free surface effects as investigated by [82]; and (d) Ekman pumping confining salt-water layer (orange).

instabilities as soon as the top layer reaches the bottom end-wall, which in turn lead to mixing of the two fluid layers. Second, the interface between saturated salt-water solution and water has to remain stable to replicate the non-mixing two-phase flow suggested by Pedlosky [104].

Sufficient salt-water layer thickness

Contact of the upper water layer with the bottom wall can be easily avoided by an appropriate thickness of the salt-water layer H_s^{min}. A lower limit for H_s^{min} is estimated with the assumption of a worst-case scenario during spin-down: a salt-water layer, which is already at rest and an upper fluid, which rotates in SBR; see figure 4.2. The pressure distribution in the water layer in SBR is given by

$$p_w(r,z) = p_0 + \rho_w g(z - z_0) + \rho_w \frac{\Omega^2 r^2}{2}, \qquad (4.4)$$

where p_0 is the ambient pressure and z_0 the water level at $r = 0$. The pressure at the interface between the two surfaces at a radial position r is given by

$$p_{int} = p(r, z = z_0 - z_{III} - z_{int}) = \rho_w \frac{\Omega^2 r^2}{2} + z_{III} \rho_w g + z_{int} \rho_w g + p_0 \qquad (4.5)$$

The pressure in at the same height and at $r = 0$ is

$$p_a = p(r = 0, z = z_0 - z_{III} - z_{int}) = \rho_w g z_{III} + \rho_s g z_{int} + p_0 \,. \tag{4.6}$$

As the salt-water layer is at rest and no centrifugal forces apply $p_a = p_{int}$, which yields

$$z_{int}(r) = \frac{\rho_w}{\rho_s - \rho_w} \frac{\Omega^2 r^2}{2g} \,. \tag{4.7}$$

This results in

$$z_{II} = \frac{\rho_w}{\rho_s - \rho_w} \frac{\Omega^2 R^2}{2} \,, \tag{4.8}$$

which due to $\rho_w/(\rho_s - \rho_w) \approx 5$ corresponds a significantly larger parabola height at the interface during spin-down than in the initial SBR. The salt-water volume during spin-down can be described by

$$V_s^{SD} = \int_{\varphi=0}^{2\pi} \int_{r=0}^{R} \left(z_I + \frac{\rho_w}{\rho_s - \rho_w} \frac{\Omega^2}{2g} (R^2 - r^2) \right) r \mathrm{d}r \mathrm{d}\varphi \,. \tag{4.9}$$

V_s^{SD} is constant in time and thus equal to the salt-water volume after the complete decay of the flow $V_s^0 = \pi R^2 H_s$. Thus, for $z_I = 0$ the minimum required salt-water thickness H_s^{min} is given by:

$$H_s^{min} = \frac{\rho_w}{\rho_s - \rho_w} \frac{\Omega^2 R^2}{4g} \,. \tag{4.10}$$

Interface stability

The stability of the interface is hypothesised to depend on the ratio of the kinetic energy that is dissipated during spin-down ($\sim \rho_s \Omega^2 R^2$) and the sta-

bilising effects of the potential energy ($\sim (\rho_s - \rho_w)gH_s$). The relation of the forces yields a hypothesis for a modified Froude number

$$Fr_s = \frac{\rho_s \Omega^2 R^2}{(\rho_s - \rho_w)gH_s},\qquad (4.11)$$

where a large Fr_s implies a higher chance for the interface to become unstable. Note, accordingly, that a high relative density $(\rho_s - \rho_w)/\rho_s$, large H_s, small Ω, and small R result in a stable two-layer system.

4.2 Small-scale experiments – medium *Re*

The preliminary goal of the small-scale experiments is to clarify whether or not an experimental approach is feasible for the spin-down problem. The feasibility study is presented as follows: § 4.2.1 provides the experimental setup before § 4.2.2 discusses the data quality and the reproducibility of the experiments. Thereafter, the stability of the salt-water layer is addressed in § 4.2.3 and its influence on the spin-down flow is evaluated in § 4.2.4.
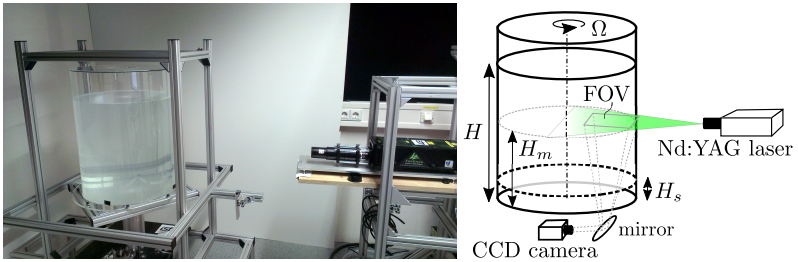
(a) Small-scale test rig with rotating cylinder (left) and laser with light sheet optics (right). (b) Sketch of the planar PIV setup.

Figure 4.3: Setup of the small-scale experiments performed at Karlsruhe Institute at Technology. Figures similar to figures in [Kaiser et al., 2016].

4.2.1 Experimental setup

As depicted in figure 4.3(a) an acrylic glas cylinder with an inner diameter
of $2R = 0.49$ m is mounted on a central shaft. The shaft is fixed with ball
bearings, which allow co-axial rotation, and connected to a step motor via a
toothed driving belt. The transmission ratio of the driving belt (3:1) in com-
bination with a closed-loop controlled step motor (NEMA 42, holding torque
2.5 Nm) allows fast acceleration and deceleration of the cylinder without
mounting an additional braking system. The cylinder can be decelerated from
a maximum rotational speed of $f = 1.5$ Hz ($\Omega = 2\pi f = 9.42$/s) within one
revolution. The closed-loop control is implemented with an incremental posi-
tion encoder and a motor controller. The control loop allows smooth rotation
without noticeable artifacts of motor stepping for $f \geq 0.075$ Hz ($\Omega \geq 0.47$/s).
The tank is filled with distilled water (room temperature 20°C, kinematic
viscosity $v = 1.004 \cdot 10^{-6}$) up to the level H. All experiments were per-
formed in an free-surface configuration (cp. § 4.1) and various aspect ra-
tios $0.5 < A = H/R < 2$ are tested. The rotational speed before spin-down
is in the range of $0.47 \leq \Omega \leq 9.42$, which corresponds to a Re range of
$28\,200 \leq Re \leq 564\,000$. The salt-water layer (height H_s) and its stability is
further tested in additional experiments.

The flow is measured with low-speed planar PIV setup as sketched in figure
4.3(b). A double-frame CCD camera (PCO Pixelfly, 1392 px × 1040 px) is
mounted below the tank to avoid image deformation due to free surface ef-
fects. The camera records double-frame images at 5 Hz and is equipped with
an AF Nikkor 50 mm objective lens. A dual pulsed Nd:YAG laser (Quantel Ev-
ergreen 70) provides a horizontal light sheet (thickness 2 mm) at the measure-
ment height H_m, which is placed at medium filling height $H_m = 0.5H$ unlesss
explicitly stated otherwise in the following. A pulse energy of 20 mJ/pulse
provides sufficient illumination of 20 µm Polyamid 12 particles in a 90 mm ×
60 mm field of view (FOV). Note that a mirror is mounted between the cylin-
der and the CCD camera to simplify the adaptation of the object distance and

ensure a similar FOV for different measurement heights H_m. The pulse distance is adapted to the initial condition (i.e. Ω) of the respective experiments to ensure a maximum displacement of 15 px, which at the present spatial resolution of 15 px/mm corresponds to a displacement of 1 mm. Following Raffel *et al.*[106], a multi-grid scheme with non-uniform final interrogation areas (96 px $\times$ 32 px with 75% and 50% overlap, respectively) was applied during post-processing to minimise in-plane loss. The long axis was aligned tangential to the circumferential main-flow direction.

4.2.2 Data quality and reproducibility

The three-dimensional DNS data of chapter 3 allows for a spatial average $\langle . \rangle = \langle . \rangle_{\varphi,z}(r,t)$ in a large volume in φ- and z-direction and thus makes the instantaneous evaluation of high-order statistics possible. The present experimental data, in contrast, is limited to the FOV of the PIV measurements,
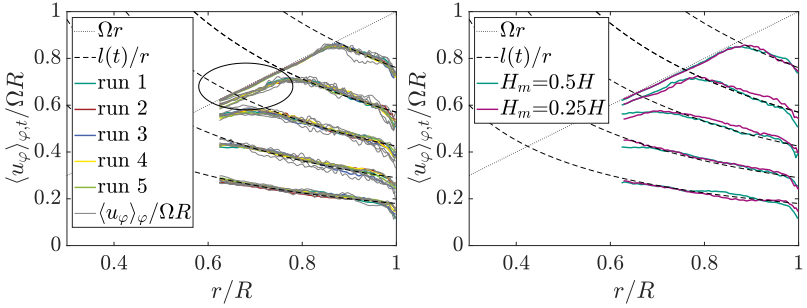
(a) Five consecutive runs of the spin-down experiment are depicted in different colors. The measurement plane is set at $H_m = 0.5H$. The ellipse highlights the footprint of core decay due to Ekman pumping.

(b) Comparison of measurements at different measurement planes $H_m = 0.5H$ and $H_m = 0.25H$.

Figure 4.4: Reproducibility of spin-down measurements exemplarily shown for $Re = 282000$ at five arbitrary time instances $\Omega t \in \{11, 22.5, 45, 90, 180\}$, which corresponds to $\theta = \nu t / R^2 \in \{3.9, 8.0, 16.0, 31.9, 63.8\} \times 10^{-5}$. SBR and regions of constant angular momentum $l(t)$ are emphasised with dotted and dashed lines, respectively. Aspect ratio was set to $A = H/R = 2$.

which requires a thorough test of statistical significance. Accordingly, this section evaluates if the average over the FOV in azimuthal direction

$$\langle u_\varphi \rangle_\varphi = \langle u_\varphi \rangle_\varphi (r,t) = \frac{1}{\varphi_{max} - \varphi_{min}} \int_{\varphi=\varphi_{min}}^{\varphi_{max}} u_\varphi (r,\varphi,t) \mathrm{d}\varphi \qquad (4.12)$$

allows a sufficient approximation of $\langle u_\varphi \rangle$ or if a combination of spatial and moving temporal average such that

$$\langle u_\varphi \rangle_{\varphi,t} = \langle u_\varphi \rangle_{\varphi,t} (r,t) = ...$$
$$... \frac{1}{(\varphi_{max} - \varphi_{min})t_{avg}} \int_{\varphi=\varphi_{min}}^{\varphi_{max}} \int_{t^*=t-t_{avg}/2}^{t+t_{avg}/2} u_\varphi (r,\varphi,t^*) \mathrm{d}t^* \mathrm{d}\varphi \quad (4.13)$$

is necessary. The parameters $\varphi_{max}, \varphi_{min}$ are the azimuthal limits of the FOV and t_{avg} is the window of the moving temporal average. The reproducibility of the results is tested by repeating and evaluating the same experiment multiple times.

Figure 4.4(a) presents the results of five consecutive spin-down experiments at $Re = 282\,000$. While the instantaneous data $\langle u_\varphi \rangle_\varphi$ (grey lines) shows run-to-run scatter, a moving temporal average over five time steps ($t_{avg} = 1\,\mathrm{s}$) delivers good run-to-run reproducibility for $\langle u_\varphi \rangle_{\varphi,t}$. Despite the limited FOV, the results of the five different runs agree well for the entire spin-down process and thereby validate sufficient statistical convergence as well as the repeatability of the experiment. As expected, the region of constant angular momentum $l(t) = u_\varphi r$ (see § 3.5.3) is also uncovered experimentally.

The results of the present section are obtained without a salt-water layer. Therefore, an influence of the bottom wall is expected and is already obvious at $\Omega t = 22$, where the vortex core has lost momentum, (circled by an ellipse in figure 4.4(a)). Linear theory implies that outside the Ekman layer, $\langle u_\varphi \rangle$ does not depend on z [23]. To clarify if this property holds also for the non-linear spin-down, measurements at different heights H_m are performed. Figure

4.4(b) presents a comparison of $H_m = 0.25H$ and $H_m = 0.5H$ in experiments with $A = 2$. Matching results suggest that the effect of the measurement height is minor and $\langle u_\varphi \rangle$ is independent of H_m and thus z.

4.2.3 Stability and required thickness of the salt-water layer

As suggested in § 4.1.3, a saturated salt-water layer is introduced at the bottom of the tank to reduce end-wall effects. The present section estimates the critical Froude number Fr_s^c (cp. (4.11)), at which the interface becomes unstable and validates the existence of the predicted inverse parabola during spin-down.

Fr_s^c is determined experimentally in various spin-down experiments, where Ω is increased from run to run, while the other quantities remain constant; saturated salt water: $(\rho_s - \rho_w)/\rho_s = 6$; $R = 0.245$ m, $H_s = 0.5R$ at $A = 0.5$. To visualise the interface, the salt-water layer is colored with food ink as shown in figure 4.5. At $f = 0.25$ Hz ($Fr_s = 2.265$) the interface shows first signs of instability. In addition, the expected inverse parabola for the interface between saltwater and distilled water can be observed. Note, however, that as expected the height of the parabola appears to be below the theoretically estimated value (z_{II}, see § 4.1.3).
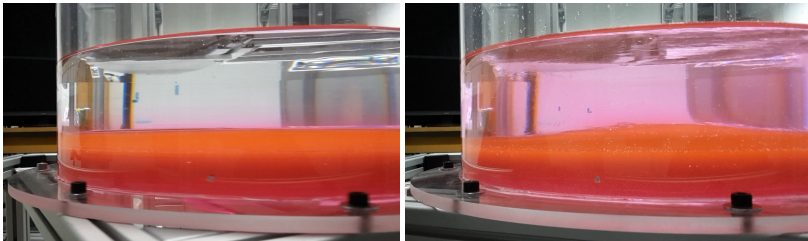
(a) spin-down from $\Omega = 0.075$ Hz. Interface remains stable and without visible curvature.

(b) spin-down from $\Omega = 0.25$ Hz. Color-coded salt water mixes into distilled-water layer. The fluid-fluid interface shows an inverse parabola.

Figure 4.5: Pictures captured during early spin-down for experiments with different Ω and thus Fr_s. Experimental parameters: $(\rho_s - \rho_w)/\rho_s = 6$; $R = 0.245$ m; $H_s = 0.04$ m at $A = 0.5$.

f [Hz]	Ω [1/s]	Re	Fr_s	z_{II} [cm]	H_s^{min} [cm]	stable
0.075	0.47	28 200	0.204	0.34	0.17	yes
0.150	0.94	56 400	0.815	1.36	0.68	yes
0.200	1.26	75 200	1.450	2.42	1.21	yes
0.250	1.57	94 000	2.265	3.77	1.89	no

Table 4.1: Re, Fr_s, stability of the interface, and the theoretical values for the height of the inverse parabola z_{II} and minimum salt-water level H_s^{min} for various Ω in the small-scale experiments. Parameters: $(\rho_s - \rho_w)/\rho_s = 5$; $R = 0.245$ m; $H_s = 0.04$ m, and $A = 0.5$.

Table 4.1 provides an overview of the performed experiments on interface stability and the theoretical parameters z_{II} and H_s^{min} for different Fr_s. The critical modified Froude number below which the interface is stable was found to be within the range $1.450 < Fr_s^c < 2.265$.

4.2.4 End-wall effect reduction: A and H_s

While for $A = 2$ end-wall effects are already existent (see figure 4.4), linear theory suggests a more significant influence for smaller $A = H/R$ as $t_E/t_D = Ek^{1/2}A^2$; cp. §4.1. The present section evaluates if the predictions on the importance of A from linear theory still apply for the turbulent and non-linear spin-down. Furthermore, it is quantified whether or not a stable salt-water layer (see §4.2.3) is capable to significantly reduce those end-wall effects. Figure 4.6(a) presents the scaling of Ekman pumping with A for $Re \approx 56400$. The effects of A are significant as the vortex core decays faster for $A = 0.5$ as for $A = 2$. However, the introduction of a salt-water layer into the low aspect-ratio setup ($A = 0.5$), results in a vortex core that contains its kinetic energy even better as the comparable experiments with $A = 2$ and no salt-water layer. To further validate the two-layer setup concerning its capability to mimic an infinite cylinder, figure 4.6(b) compares the experiments at $Re \approx 28\,200$ with the DNS data presented in chapter 3 ($Re = 28\,000$). Within
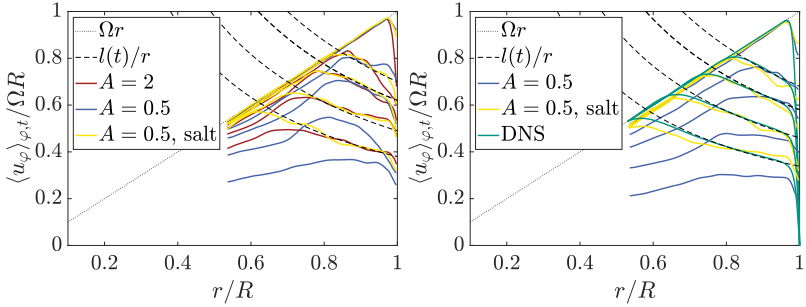
(a) $Re = 56\,400$: spin-down experiments with $A = 2$ (red) and $A = 0.5$ (blue, yellow). Bottom wall influence increases with decreasing A. However, a salt-water layer significantly reduces end-wall effects (yellow).

(b) Comparison of DNS results for $Re = 28\,000$ and experimental results at $Re = 28\,200$ with $A = 0.5$. The experiment with salt-water layer show good agreement with the simulation.

Figure 4.6: Influence of aspect ratio $A = H/R$ and the presence of a salt-water layer on the flow character during spin-down experiments. Five time instances $\Omega t \in \{2, 8, 16, 32, 64\}$ are presented. SBR and regions of constant angular momentum $l(t)$ are emphasised with dotted and dashed lines, respectively. Measurements were performed at height $H_m = 0.5H$.

the accuracy of the experimental data, the experiment with salt-water layer shows good agreement with the DNS data.

In conclusion, the small-scale experiment validates the capability of the experimental method to approximate low order statistics such as $\langle u_\varphi \rangle$ and provides a salt-water layer as an appropriate technique to obtain a flow, which is similar to the decay in an infinite cylinder. This end-wall effect reducing technique provides reliable data for $Fr_s \leq 1.45$. A destabilisation of the interface was observed at $Fr_s = 2.265$. In conclusion the critical Froude number, where the interface destabilises, lies within the range $1,45 < Fr_s^c < 2.265$ For $Fr_s > Fr_s^c$ the salt-water layer cannot be used and a large aspect ratio A is considered an alternative measure to reduce end-wall effects.

4.3   Large-scale experiments – high *Re*

To increase the Reynolds number range ($Re = \Omega R^2/\nu$) of the spin-down problem towards very high Re, experiments were conducted during a three-week campaign at the CORIOLIS II platform in Grenoble, France. The platform with $2R = 13\,$m diameter and an approximate weight of 300 t is the largest of its kind.

The large dimensions of the platform allow high temporal and spatial resolutions and small curvatures of the free surface while Reynolds numbers up to $Re = 4 \cdot 10^6$ can still be achieved. The present section describes the parameter range, the experimental setup, and investigates if the scaling of the salt-water layer stability suggested in § 4.2.3 holds for very large Re.

4.3.1 Parameter range

For the present campaign, the filling height of the $13\,$m diameter platform was set to 1 m, which results in approximately $133\,\mathrm{m}^3$ of water and an aspect ratio $A = H/R = 2/13$ for all conducted experiments. For the PIV measurements the complete volume was seeded with polyamide 12 particles (density $\rho_p = 1.03\,$g/cm^3, diameter $d_p = 30\,\mu$m; Orgasol 2002 ES3 NAT). To reduce particle settlement during the very long spin-up times until SBR is reached (2 h-3 h) the density of the water is slightly increased to $\rho_w = 1.004\,$g/cm^3 by dissolving a small amount of salt. Due to temperature variations of the water T_w during the measurement campaign ($15.8°$C $\leq T_w \leq 18°$C), ν varied within the range $1.06 \cdot 10^{-6}\,\mathrm{m}^2/\mathrm{s} \leq \nu \leq 1.12 \cdot 10^{-6}\,\mathrm{m}^2/\mathrm{s}$. To account for the temperature changes, the water temperature was measured before each run.

revolution time [s]	Re $\times 10^6$	runs (total)	ramp time (salt water)	t_{SD} [s]
470	0.5	2	-	10.9
240	1.0	2	-	16.9
120	2.0	8	2	23.4
90	2.7	4	2	30.3
60	4.0	2	-	37.8

Table 4.2: Overview of conducted spin-down experiments at the CORIOLIS II platform.

Table 4.2 provides an overview of the performed spin-down experiments. In a total of 18 successful runs, five different rotation rates within the range $0.0134/\text{s} \leq \Omega \leq 0.105/\text{s}$ were tested. The high mass of the platform limits the maximum deceleration rate to $3.4 \cdot 10^{-3}\,\text{rad/s}^2$. In combination with jerk-free acceleration, the time span until the final velocity of the platform is reached (ramp time t_{SD}) varies in the range $0.12 \leq \Omega t_{SD} \leq 3.97$ or $\theta < 10^{-6}$.
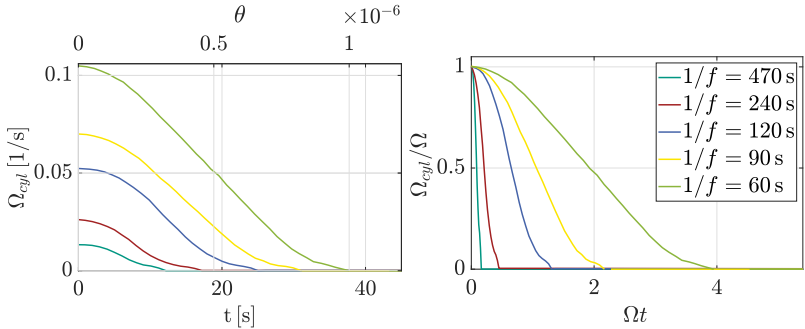
(a) Time and Ω_{cyl} in SI units. Second time axis normalised as $\theta = \nu t / R^2$.

(b) Time and Ω_{cyl} normalised by Ω.

Figure 4.7: Angular velocity of the platform Ω_{cyl} during the deceleration process for different revolution times $1/f = 2\pi/\Omega$.

The angular velocity of the cylinder Ω_{cyl} during the deceleration is visualised in figure 4.7.

For the last two days of the campaign a layer of saturated salt-water was carefully introduced at the bottom of the cylinder. Approximately 3.4 t of salt were dissolved to produce $10.6 \, \text{m}^3$ of saturated salt-water solution, which corresponds to a layer of 8 cm thickness. Four spin-down experiments were conducted with the salt-water layer.

4.3.2 Experimental setup

Figure 4.8(a) provides an overview of the three PIV setups that are conducted simultaneously. All experimental equipment is mounted on the rotating platform and thus co-rotates and accelerates/decelerates with the cylinder. A stereo setup (figure 4.8d) uses the optical access through one of the 16 lat-
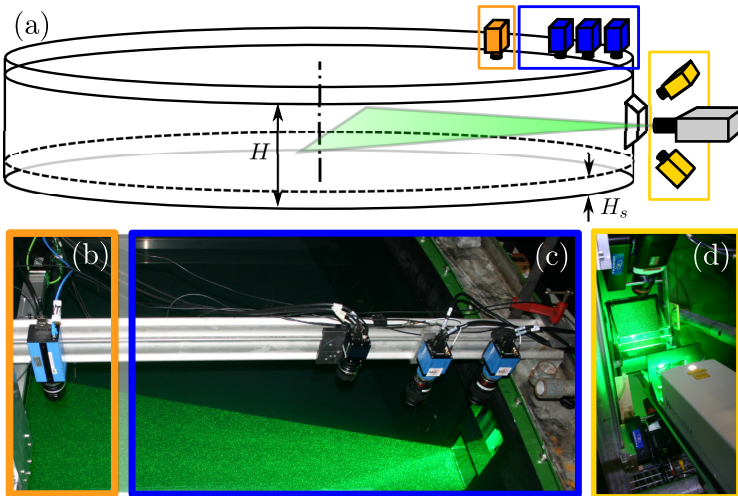
Figure 4.8: Measurement setup at the CORIOLIS II platform: (a) schematic overview; (b) planar PIV at 1.5 m distance from side walls; (c) planar three camera PIV system; and (d) high-speed stereo PIV.

eral windows. In addition, planar PIV is captured through the open surface (figures 4.8b,c).

All three PIV setups utilise the same horizontal laser sheet produced by a continuous 25 W Spectra Physics Millennia laser. Exposure time $t_E \leq 0.5 \cdot 10^{-3}$ s and repetition rate are controlled by the respective camera.

A pco.1200 HS (AF Nikkor 50 mm, figure 4.8(b)) records the flow at a approximate side-wall distance of 1.5 m ($r = 5$ m). A FOV of 25 cm × 20 cm results in a resolution of approximately 5 px/mm. Note that during the measurement time, the side-wall boundary layer will not grow up to $\delta_{99} = 1.5$ m. Thus, the purpose of this camera is solely to record if end-wall effects lead to a decay of the core flow.

The side-wall boundary layer is recorded by a time-resolved three-camera system consisting of two pco.edge 5.5 (Samyang ED AS UMC 35 mm) and a Dalsa Falcon 4M (AF Nikkor 28 mm). The cameras shown in figure 4.8(c) provide an overlapping FOV with a radial extend of approximately 75 cm and a resolution of 10 px/mm. Due to varying flow velocities at different *Re* (different Ω) the recording frequency varies between 25 Hz–200 Hz. For the higher recording frequencies the cameras cannot operate in full-frame mode. As such, the azimuthal extent of the FOV varies within the range 4 cm – 21.5 cm.

The stereoscopic high-speed PIV setup shown in figure 4.8(d) focuses on the onset of instabilities. Two Phantom Miro M310 cameras (AF Micro-Nikkor 60mm) are each oriented 45° towards the light-sheet and record the near-wall region with a resolution of 14.5 px/mm. Image distortion is minimised by a water-filled acrylic glass prism attached to the lateral window. Dependent on Ω, the recording frequency varies within the range 40 Hz-400 Hz.

4.3.3 End-wall effect reduction

The aspect ratio is limited by the maximum filling height of the CORIOLIS II platform and set to $A = 2/13$. As discussed in §4.2.4, small A imply large

impact of end-wall effects. Therefore, the evaluation of experiments without a salt-water layer is limited to the early stages of the flow and in particular the transition process. However, to gather information about the boundary-layer growth during the turbulent stage III (see § 3.5.3), seven experiments are performed with a saturated salt-water solution at the bottom of the cylinder; see § 4.3.1.

$1/f$ [s]	Ω [1/s]	approx. Re	Fr_s	z_{II} [cm]	H_s^{min} [cm]	stable
120	0.052	2.0×10^6	0.89	0.74	0.37	yes
90	0.070	2.7×10^6	1.57	2.95	1.48	yes

Table 4.3: Re, Fr_s, stability of the interface, and the theoretical values for the height of the inverse parabola z_{II} and minimum salt-water level H_s^{min} for various Ω in the small-scale experiments. Parameters: $(\rho_s - \rho_w)/\rho_s = 6$; $R = 6.5$ m; $H_s = 0.08$ m, $T_w = 15.8°$C , and $A = 2/13$.

The experimental parameters of the experiments with salt-water layer satisfy the requirements formulated in sections 4.1.3 and 4.2.3. Table 4.3 provides an overview of the parabola height z_{II} and the hypothesised measure of interface stability Fr_s. The small-scale experiments provided an estimate for the critical Frounde number within the range $1.45 \leq Fr_s^c \leq 2.65$. As for 2.7×10^6, the Frounde number $Fr_s = 1.57$ slightly exceeds the maximum stable Frounde number found in the small-scale experiments ($Fr_s = 1.45$), the interface stability is additionally validated by capturing the interface with an additional camera through one of the lateral windows. The interface remained stable for two days and four spin-down experiments. Two runs at $Re = 2 \cdot 10^6$ and two runs at $Re = 2.7 \cdot 10^6$ were performed. However, at the third day of the measurements with salt-water layer the interface became unstable during an experiment, which made the data of the run unusable and also marked the end of the experimental campaign. It is hypothesised that the interface thickness had grown due to diffusion and thus lost its stability.

(a) spin-down at different *Re*.

(b) Influence of salt-water layer on spin-down.
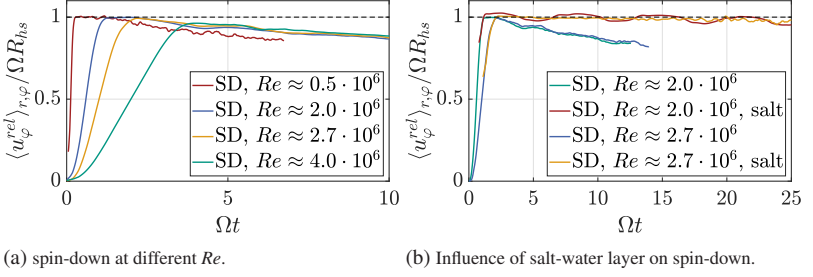
Figure 4.9: End-wall effects and their reduction. While $\langle u_{\varphi}^{rel} \rangle_{r,\varphi}/\Omega R_{hs} \approx 1$ the core is still in SBR. The ramp of of the acceleration/deceleration process varies for different *Re*. The experiments where a saturated salt-water layer was introduced are marked with the tag "salt".

The influence of end-wall effects was further assessed quantitatively by evaluating the results of the pco.hs1200 (figure 4.8b), which was positioned at $R_{hs} = 5\,\text{m}$. The relative velocity of the fluid towards the platform u^{rel} is evaluated and spatially averaged over the complete FOV. The resulting quantity $\langle u_{\varphi}^{rel} \rangle_{r,\varphi}$ grows to $\langle u_{\varphi}^{rel} \rangle_{r,\varphi} \approx \Omega R_{hs}$ during the acceleration/deceleration of the platform and should remain constant, while the core flow is still intact.

Figure 4.9 shows the temporal evolution of $\langle u_{\varphi}^{rel} \rangle_{r,\varphi}$ to analyse the impact of Ekman pumping. Figure 4.9(a) shows a strong end-wall effect during spin-down without the salt-water layer for all *Re*. In particular, for $Re = 4 \cdot 10^6$, the increased deceleration times for high *Re* (see table 4.2) in combination with the end-wall effects during spin-down, leads to a decay of the SBR in the vortex core before the platform is completely at rest. In figure 4.9(b) the influence of the salt-water layer is evaluated. The saturated salt-water layer preserves the SBR and thus significantly extends the time span, where meaningful observations of the side-wall boundary layer can be made.

In conclusion, the reduction of end-wall effects with the salt-water layer proves to be successful and the suggested scaling of the interface stability with Fr_s is confirmed. While the usability of experiments without salt-water layer is limited to an analysis of the transition process, the successful re-

duction of end-wall effects allows a long-term observation of the turbulent side-wall boundary layer.

4.4 Results

This section strives to validate the hypothesised scaling which resulted from the DNS presented in chapter 3. In § 4.4.1 the transition to turbulence is addressed. In particular, the primary instability mechanism is discussed and the scaling of the onset time θ_o is investigated. Thereafter, the scaling of boundary-layer growth during the turbulent stage is described in § 4.4.2.

4.4.1 Transition

The objectives of the present section are twofold. First, it is to be validated if centrifugal instabilities also occur at very high Re. Second, the time instance $\theta_o = \nu t_o / R^2$, where $\langle u_\varphi \rangle$ first deviates from a laminar profile is captured and compared to analytical, numerical and experimental studies in literature. The time instant θ_o is equivalent to the onset time defined by Neitzel & Davis [97], who defined the time instance of minimal torque on the cylinder walls as their characteristic time.

The Re range of the present data exceeds prior measurements by two orders of magnitude. Note, however, that the finite deceleration time of the CORIOLIS II platform discussed in § 4.3.1 has to be taken into account, when comparing the present data to literature. In particular, the onset time θ_o and in some cases also Re are corrected in the following.

Primary instability

At very high Re, the influence of curvature decreases as δ_{99}/R is very small during transition. Thus, the flow asymptotically approaches Stokes' first problem with growing Re. Stokes' first problem is also linearly unstable [81], however the transition to turbulence is initiated by Tollmien-Schlichting (TS) waves instead of a destabilisation of streamwise vortices as they appear in
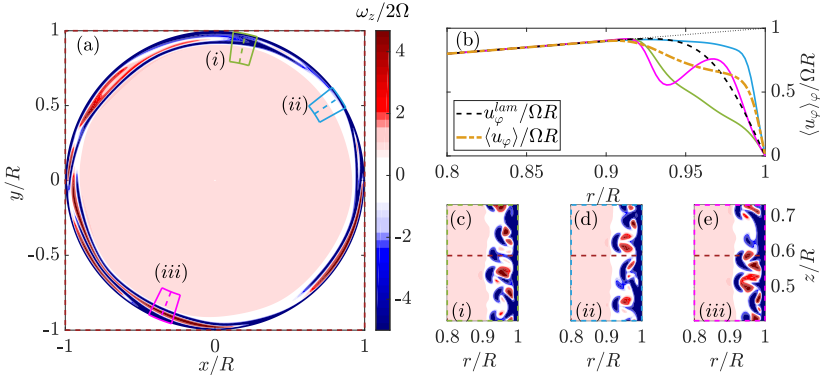
Figure 4.10: Exemplary horizontal cuts through spin-down data of the DNS ($Re = 12\,000$, $\Omega t = 4.7$) depicting the footprint of Taylor rolls on two-dimensional data: (a) Possible positions of the FOV of PIV; (b) profiles of $\langle u_\varphi \rangle$ in the respective FOV compared to $\langle u_\varphi \rangle$ averaged over φ and z and the laminar solution at the same time instance; (c)-(e) vertical cut through the respective FOVs: (*i*) fluid moving in negative radial direction; (*ii*) fluid moving in positive radial direction; and (*iii*) cut through the middle of the streamwise vortex.

the case of centrifugal instabilities. In flat and spatially developing boundary layers, spanwise periodic arrays of boundary-layer streaks were shown to successfully stabilise TS waves [21, 36, 117]. Thus, it is hypothesised, that even if the onset times of TS waves and centrifugal instabilities were similar, the streamwise structures would damp TS waves. However, if *Re* is high enough, TS waves could possibly occur before spanwise periodic structures. Assuming impulsive spin-down, the critical wavelength λ_c of possible centrifugal instabilities are estimated using the prediction of Kim *et al.* [61]. Small λ_c within the range $7.5\,\text{mm} \leq \lambda_c \leq 28.9\,\text{mm}$ for initial rotation times 470 s - 60 s are expected. Therefore, the highly resolved horizontal stereo setup (figure 4.8d, resolution: 14.5 px/mm) is utilised to capture the transition process. Due to very large scales of the facility ($R = 6.5$) the normalised spatial resolution and the normalised temporal resolution ($\theta = \nu t / R^2$) is sufficient to capture the transition process at the present high *Re*.

91

The footprint of Taylor rolls in the FOV of the PIV measurements depends on the relative axial position of the light sheet towards the Taylor rolls. Three distinct scenarios occur as visualised with numerical data from chapter 3 in figure 4.10(a), where three possible relative positions of the Taylor rolls towards the light sheet are presented with three synthetic FOVs $(i) - (iii)$. Figures 4.10(c-e) show a vertical cut through the respective FOV and motivate the origin of the deviating vorticity distributions of cases $(i) - (iii)$. If the light sheet cuts through the centre of the streamwise vortices a distinct vorticity profile is detected (case (iii), see figure 4.10(a,e)). The effects of Taylor rolls are less obvious if the light sheet cuts through the centre or the outer border of the plumes (cases (i) & (ii) in figures 4.10(a,c,d)). Here, the movement of fluid in either positive or negative radial direction leads to an increase or decrease of the boundary-layer thickness, respectively. Figure 4.10(b) presents the effect of cases $(i) - (iii)$ on $\langle u_\varphi \rangle_\varphi$. During the primary instability, the velocity profiles averaged over the synthetic FOVs $\langle u_\varphi \rangle_\varphi$ deviate significantly from the statistically converged average over the complete volume of the simulation $\langle u_\varphi \rangle = \langle u_\varphi \rangle_{\varphi,z}$. While case (iii) shows a characteristic profile with two infliction points, case (i) is hard to distinguish from a laminar profile at an earlier stage. During transition the axial position and the size of Taylor rolls change. Thus, cases $(i) - (iii)$ might be observable in the same FOV during the same experiment. As only the footprint of case (iii) is unique, it is utilised as the criterion that a Taylor roll occurred at the time $\theta_{(iii)}$; see table 4.4.

For almost all experiments the existence of Taylor rolls is validated at a time $\theta_{(iii)}$ (see table 4.4) before the transition to turbulence. For the two experiments, where case (iii) is not detected, it is unclear which mechanism led to transition to turbulence. Taylor rolls could still have been present (only case (i) and/or case (ii) in the FOV), however also other mechanisms could have led to transition. Yet it can be concluded, that for the present high Re measurements the centrifugal instability generally occurs before TS can evolve. This is in good agreement with studies on spatially developing boundary lay-

$1/f$ [s]	Re $\times 10^6$	$\nu \left[\frac{\text{m}}{\text{s}^2}\right]$ $\times 10^{-6}$	$\theta_{(iii)}$ $\times 10^{-7}$	θ_o $\times 10^{-7}$	$\Delta\Omega(\theta_o) \left[\frac{1}{\text{s}}\right]$ $\times 10^{-2}$	Re_{cor} $\times 10^6$	θ_o^{cor} $\times 10^{-7}$
470	0.52	1.08	12.82	8.81	1.34	0.52	7.41
470	0.52	1.10	15.38	9.34	1.34	0.52	6.23
240	1.01	1.09	8.14	6.34	2.62	1.01	3.16
240	1.03	1.07	-	-	-	-	-
120	2.10	1.06	4.99	4.49	4.39	1.75	1.27
120	2.03	1.09	4.70	4.59	4.35	1.68	1.29
120	1.97	1.12	4.52	4.52	4.14	1.56	1.33
120	1.97	1.12	3.80	3.80	3.20	1.20	1.41
120	1.97	1.12	4.26	4.26	3.80	1.43	1.20
120	1.98	1.12	3.96	3.69	3.17	1.20	1.27
120	1.98	1.12	3.75	3.75	3.17	1.20	1.21
120	1.98	1.12	-	-	-	-	-
90	2.66	1.11	4.73	4.73	4.45	1.69	1.58
90	2.62	1.12	4.31	4.31	3.84	1.44	1.38
90	2.65	1.12	4.59	4.59	4.25	1.61	1.53
90	2.65	1.12	4.30	4.30	3.84	1.46	1.48
60	3.99	1.11	4.47	4.47	4.71	1.79	1.18
60	3.94	1.12	4.52	4.52	4.71	1.77	1.14

Table 4.4: Performed spin-down experiments. Note that due to varying water temperatures. the kinematic viscosity and thus Re slightly varies for the experiments with equal f.

ers with small curvature ratios δ_{99}/R [9, 126], where centrifugal instabilities lead to the evolution of Görtler vortices.

Transition time θ_o

After the presence of Taylor rolls is confirmed, in the following their onset time θ_o is compared to prior experiments of smaller Re and predictions from stability analysis.

(a) Temporal developement of $\langle u_\varphi \rangle$. ω_z at the time instant $\theta_{(iii)}$, where Taylor rolls first appear (vorticity field shown in inlay).

(b) Development of the fitted time θ_{fit} that corresponds to the analytical solution of a laminar profile for a perfectly impulsive spin-down.
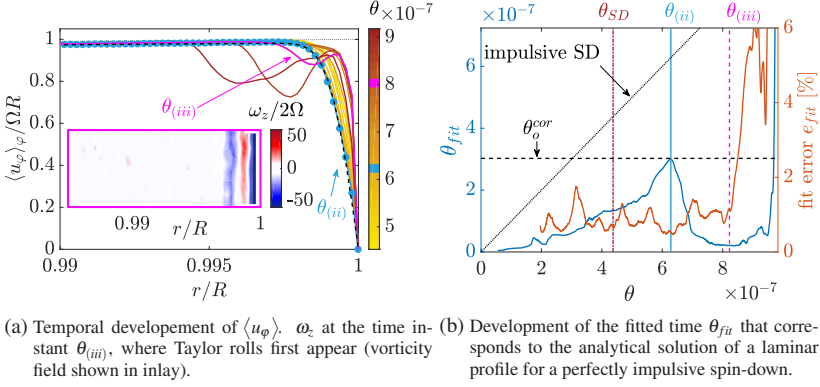
Figure 4.11: Application of the method to determine the corrected onset time θ_o^{cor} at $Re \approx 1 \cdot 10^6$. At the time instant θ_o at which the velocity profile starts to deviate from laminar growth (here $t_{(ii)}$) the fitted to time of the equivalent analytical solution θ_{fit} is determined and set to θ_o^{cor}. At $Re \approx 1 \cdot 10^6$ the tank is at rest before transition starts $t_T > t_{SD}$.

The rotation of the CORIOLIS II platform does not stop instantaneously but within a finite ramp time $\theta_{SD} = v t_{SD}/R^2$ (cp. §4.3.1). Therefore, even for the laminar stage the velocity profiles $\langle u_\varphi \rangle$ are not equivalent with the analytical solution u_φ^{lam} (cp. (3.12)). To account for $\theta_{SD} \neq 0$ a five step algorithm is applied. Figure 4.11 visualises the process for one of the experimental runs at $Re \approx 1 \cdot 10^6$.

- First, it is checked if case (*iii*) is detected at any time within in the FOV of the PIV measurement, as highlighted with the magenta line and the inlay in figure 4.11(a). The experiments in which case (*iii*) was not detected are excluded from the following analysis.

- For all times $\theta < \theta_{(iii)}$ an alternate time θ_{fit} is found, where the relative fit error

$$e_{fit}(\theta_{fit}, \theta) = \frac{1}{0.01R} \int_{r=0.99R}^{R} \left| \frac{u_\varphi^{lam}(\theta_{fit}, r) - \langle u_\varphi \rangle_\varphi(\theta, r)}{\langle u_\varphi \rangle_\varphi(\theta, r)} \right| \mathrm{d}r \quad (4.14)$$

is minimal. Figure 4.11(a) shows the temporal evolution of $\theta_{fit}(\theta)$. While for a perfectly impulsive spin-down $\theta_{fit} = \theta$, the finite ramp times yield $\theta_{fit} < \theta$.

- In addition to accounting for the finite ramp times, θ_{fit} also provides a measure if case (*i*) or (*ii*) occur in the FOV before case (*iii*). As shown in figure 4.11(b), θ_{fit} starts to decline at $\theta_i = 6.3$. This is due to case (*ii*) being present in the FOV. The onset time θ_o is set to whichever case occurs first

$$\theta_o = \min\left(\theta_{(i)}, \theta_{(ii)}, \theta_{(iii)}\right). \tag{4.15}$$

For the experiment shown in figure 4.11 case (*ii*) is first detected, leading to $\theta_o = \theta_{(ii)}$.

- As of now the corrected onset time $\theta_o^{cor} = \theta_{fit}(\theta_o)$ can be defined. $u_\varphi^{lam}(\theta_{fit}^{cor}, r)$ (dashed black line in figure 4.11(a)) shows excellent agreement with $\langle u_\varphi \rangle_\varphi(\theta_{(i)}, r)$ (light blue line).

- For the experiments with $Re \geq 2 \cdot 10^6$ Taylor rolls occur before the tank is fully at rest. Therefore, the spin-down process cannot be considered to be impulsive. However, to compare the data of those $Re \geq 2 \cdot 10^6$ experiments with the impulsive spin-down theory, a second correction is applied. The change of angular velocity at the time instance of transition θ_o is determined: $\Delta\Omega = \Omega - \Omega_{cyl}(\theta_o)$. $\Delta\Omega$ is utilised to formulate a corrected Reynolds number $Re_{cor} = \Delta\Omega R^2/\nu$.

The algorithm is applied to all performed spin-down experiments. The results are reported in table 4.4 and compared to literature data in figure 4.12.

The critical time θ_c predicted by propagation theory [61] (solid line, see §3.6.1) occurs significantly earlier as the onset time θ_o. Kim *et al.* [61] reported good agreement between θ_o from experiments and simulations and $4\theta_c$ (dashed line). The numerical results for the onset time θ_o from chapter 3 coincide with the visually captured onset time θ_v of earlier experiments. The visual onset time θ_v is the time instant, where aluminium flakes in the fluid
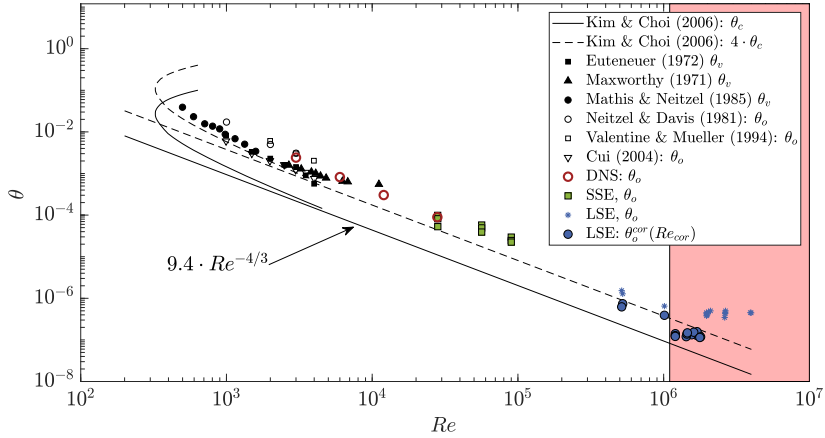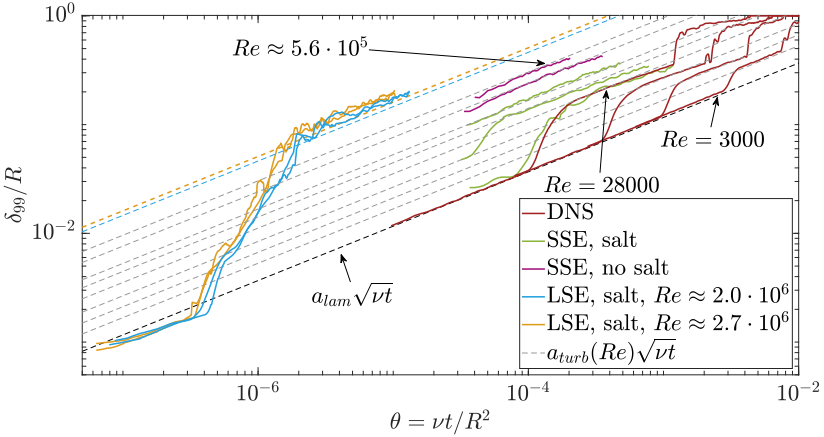
Figure 4.12: Comparison of present experimental data of the small (SSE) and large-scale experiment (LSE) to numerical data (empty markers) and prior experiments (filled markers). Due to the significant spin-down time for the large scale experiments, both Re and θ_o are corrected. The corrected onset times θ_o^{cor} are also plotted.

first revealed the onset of Taylor rolls during spin-down experiments. The experimental results from the small-scale (LSE) and large-scale (SSE) experiments align with the predicted trends and extend the Re range significantly. Note that for the for each large-scale experiment $\theta_o(Re)$ and $\theta_o^{cor}(Re_{cor})$ are plotted, respectively. The data, where the instability occured before the platform was at rest is highlighted with a coloured background.

4.4.2 Boundary-layer thickness

The numerical results presented in chapter 3 hypothesise a scaling for the turbulent boundary-layer growth. After the transition to turbulence, the growth of the boundary-layer thickness maintains its viscous time scale $\sim \sqrt{vt}$, yet with a Re dependent proportionality factor a_{turb} (cp. § 3.6). In particular the scaling law (3.22)

$$a_{turb}/a_{lam} = 0.1Re^{\frac{1}{3}}$$
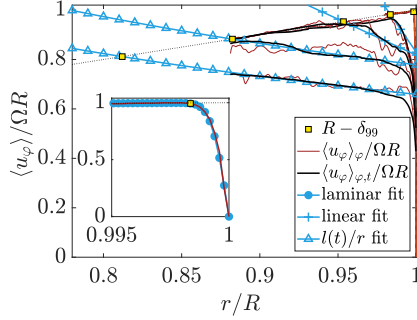
Figure 4.13: Fitting techniques for a robust approximation of δ_{99} exemplarily shown for an experiment at $Re \approx 2.6 \cdot 10^6$ with salt water layer at five arbitrary time instances $\Omega t \in \{1.1, 2.2, 4.3, 8.7, 23.9\}$, which corresponds to $\theta = vt/R^2 \in \{4.1, 8.2, 16.4, 32.9, 90.0\} \times 10^{-7}$. The applied fitting functions are: analytical solution of the laminar profile during laminar stage, linear fit during transition to turbulence and potential vortex during turbulent stage.

is suggested based on the numerical date within the range $3000 \leq Re \leq 28\,000$. The present section strives to validate the scaling law with experimental data for high Re. As discussed in § 4.4.1 the limited FOV of the PIV measurements leads to non-converged velocity profiles $\langle u_\varphi \rangle_\varphi$ after the onset time θ_o. This complicates the extraction of such sensitive quantities as δ_{99}. Therefore, more robust methods as the 1% threshold (cp. (3.8)) are applied to estimate δ_{99} from the experimental data. In particular, for each flow stage (laminar, transition to turbulence and turbulent stage) the data is fitted with an appropriate function. Figure 4.13 provides an overview of the algorithm.

Stage I: Laminar stage – circular marker

$\langle u_\varphi \rangle_\varphi(\theta)$ is approximated by $u_\varphi^{lam}(\theta_{fit})$ (see equation (4.14) and the inlay in figure 4.13). The respective δ_{99} is evaluated by $\delta_{99}/R = a_{lam}\sqrt{\theta_{fit}}$ (3.14). The highly resolved data of the stereo system is utilised during this stage (figure 4.8(d)).

Figure 4.14: Comparison of present experimental data of the small (SSE) and large-scale experiment (LSE) to numerical data (DNS). The plotted curves correspond to $Re \in \{3000, 6000, 12\,000, 28\,000\}$ (DNS), $Re \in \{28\,200, 56\,400, 94\,000\}$ (SSE, salt, $A = 0.5$), $Re \in \{282\,000, 564\,000\}$ (SSE, no salt, $A = 2.0$), and $Re \in \{2.0 \cdot 10^6, 2.7 \cdot 10^6\}$ (LSE, salt, $A = 2/13$) Dashed lines show the predicted Re scaling of turbulent boundary layers from equation (3.22).

Stage II: Emergence of Taylor rolls – plus shaped marker

As the boundary layer thickness quickly exceeds the FOV of the stereo setup, the planar PIV setup is utilised in the following (figure 4.8(c)).
To achieve better convergence of the velocity profiles, the data is additionally averaged over a moving time window of $\Delta\theta = 10^{-7}$. The resulting velocity profiles $\langle u_\varphi \rangle_{\varphi,t}$ are fitted with a linear fit and the intersection with the SBR is selected as the approximation of δ_{99}.

Stage III: Turbulent regime – triangle shaped marker

After transition to turbulence $\langle u_\varphi \rangle_{\varphi,t}$, a region of constant angular momentum $l(t)$ forms. As suggested in §3.6.5 this feature of the flow is utilised by fitting the vorticity free region of a Rankine vortex $l(t)/r$ onto $\langle u_\varphi \rangle_{\varphi,t}$. Again the intersection with the SBR is depicted as the approximation of δ_{99}.
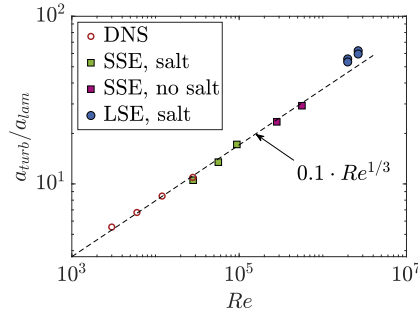
Figure 4.15: *Re* scaling of a_{turb}/a_{lam} for numerical resulsts (DNS, cp. figure 3.17(b)) small-scale experiments (SSE) and large-scale experiments (LSE).

Figure 4.14 presents $\delta_{99}(\theta)$ for the different performed experiments and numerical simulations. Hereby, the data of the small-scale experiments as well as the large-scale experiments is considered. For parameters with $Fr_s < Fr_s^c$, the experiments with salt-water layer and small aspect ratios (SSE: $A = 0.5$ (green lines in figure 4.14), LSE: $A = 2/13$ (blue and orange lines)) are evaluated. In case of the small-scale experiments additional experiments at higher Ω are considered in figure 4.14 (purple lines). No end-wall effect reducing salt-water layer is possible in those experiments as $Fr_s > Fr_s^c$. Therefore, end-wall effects are reduced by a larger aspect ratio $A = 2$.

As discussed in § 4.4.1, the deviation of $\delta_{99}/R \neq a_{lam}\sqrt{\nu t}$ during the laminar stage of the large-scale experiments results from the finite ramp time θ_{SD}. All performed experiments show good agreement with the expected boundary-layer development $a_{turb}(Re)\sqrt{\nu t}$ during the turbulent stage. This is additionally emphasised in figure 4.15, where the present data is compared to the suggested scaling of a_{turb}/a_{lam} from equation (3.22).

4.5 Summary

The present chapter describes two experiments that were designed to validate various *Re*-scaling hypotheses of the vorticity annihilating spin-down process

formulated in chapter 3. Two requirements were satisfied for the experimental design:

- **End-wall effects:** To mimic the infinite cylinder simulated in chapter 3, end-wall effects in the experiments have to be minimised. Hereby, two approaches were tested and adapted. First, if possible, a large aspect ratio (A) is chosen. Second, as a large A is not an option in experiments at the CORIOLIS II platform ($A = 2/13$), an alternate approach was suggested, tested, and validated. While the top wall is simply removed (free-surface configuration), the bottom wall influence is reduced by a saturated salt-water layer. Two requirements are identified for the salt-water layer so as not to mix with the water layer: A sufficient salt-water layer thickness (H_s); and a small modified Froude number (Fr_s). If these two requirements were met, the salt-water layer reduced the end-wall effects to such an extent, that the side wall time scale dominated over the end-wall effects.

- **Measurement technique:** To capture statistics of a transient and turbulent flow enough data had to be captured simultaneously to allow for sufficient averaging. In contrast to single-point measurements techniques, the planar (and stereo) PIV measurements that were used, allowed for the capture of the flow evolution in a two-dimensional FOV, and thus a spatial average. The combination of a spatial average (along the φ-direction) and a moving temporal average proved to be sufficient to estimate first-order statistics such as $\langle u_\varphi \rangle \approx \langle u_\varphi \rangle_{\varphi,t}$.

The large-scale CORIOLIS II platform, in combination with the carefully-designed experiments, allowed for the extent of the Re range for more than two orders of magnitude when compared to experimental data available in the literature. The hereby captured data now provides insights into the Re scaling of the spin-down process.

- **Instability mechanism:** Even at very high *Re*, and for very slightly curved streamlines (small δ_{99}/R), the centrifugal instability remains the primary instability mechanism.

- **Onset time:** The time instant where $\langle u_\varphi \rangle$ first deviates from the laminar profile u_φ^{lam} scales as predicted by Kim *et al.* [61] by $\theta_o \sim Re^{-4/3}$.

- **Turbulent growth of boundary-layer thickness:** During stage III the boundary-layer thickness grows proportional to $\sqrt{\nu t}$ for all *Re*. However, the proportionality constant a_{turb} is *Re*-dependent such that $a_{turb}/a_{lam} = 0.1 Re^{1/3}$. This empirical scaling law suggested in chapter 3 is confirmed by both the results of the small as well as the large scale experiments.

5 Scales of vortex formation – accelerated propulsors

Chapters 3 and 4 focus on the vorticity annihilating boundary layer between a vortex and a solid boundary. The interaction of oppositely signed vorticity is discussed in the simplified scenario of a vortex decaying from SBR. In bio-propulsion however, a vortex results from the roll-up of a shear layer separating from a vortex-forming edge (VFE, highlighted in green in figure 5.1). This chapter shifts the focus away from vortex decay and the vorticity-annihilating boundary layer and towards vortex formation and its stability. Hereby, the vorticity-feeding shear layer, as well as the evolution of the vortex core, are analysed.

"In particular, we strive to draw insight into the influence of turbulence and associated coherent flow structures of different length scales on the vortex formation process. Inspired by undulated modifications on the VFE of multiple
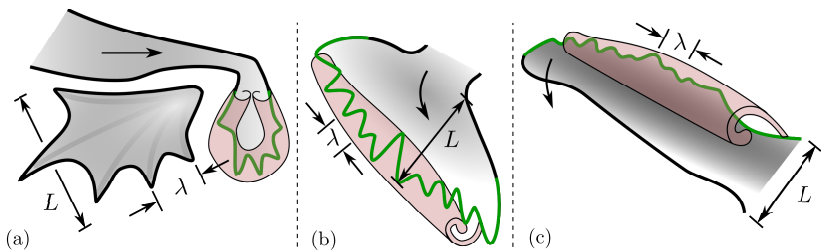
Figure 5.1: Undulatory modifications of the vortex-forming edge (VFE; depicted in green): (a) leopard frog (sketch abstracted from [59]); (b) sea lion (sketch abstracted from [115]); (c) humpback whale (sketch abstracted from [33]). Figure adapted from [Kaiser et al., 2020b].

propulsors in nature (see figure 5.1), this problem is tackled with a combined study of vortex formation over a wide range of Re superimposed with various VFE modifications. While an increase of Re is known to extend the range of turbulent substructures towards additional smaller vortices, VFE modifications allow for the introduction of disturbances with distinct wavelengths λ, which are predetermined by the propulsor itself." [Kaiser et al., 2020b]

This chapter is based on the publication *The influence of edge undulation on vortex formation for low-aspect-ratio propulsors* [Kaiser et al., 2020b]. In addition, preliminary results of the data presented in this chapter were previously reported in [Kaiser et al., 2018] and [Kaiser et al., 2019].

5.1 Background on vortex formation

5.1.1 *Re* scaling of vortex formation in bio-propulsion

The short review of evolutionary convergence in nature given in chapter 1 highlighted reoccurring kinematics in animal locomotion such us similar wake behaviour ($0.2 \leq St \leq 0.4$) and the use of rotation for LEV stabilisation ($Ro < 4$). In contrast, the Re range in which vortical structures occur ($10^2 \leq Re \leq 10^8$ [37]) suggests that, independent of viscous effects, vortices can be a efficient method to produce lift and thrust. However, the brief review of free shear layers in § 2.3.2 as well as the detailed analysis of vorticity annihilation in chapters 3 and 4 clearly motivates that Re will somehow influence vortex formation and its decay.

"By conducting experiments over a wide range of Re, the present study attempts to address the paradox, that on the one hand, the Re influence based on dimensional analysis seems to be small, yet, on the other hand, the entrainment in free shear layers is influenced by the small structures and thus Re. Particular focus lies on the interaction of the Re scaling with the aforementioned VFE modifications." [Kaiser et al., 2020b]

5.1.2 Background on vortex-forming edge modification

"For quasi-steady flows, applications of passive flow control by means of geo-
metrical modifications are well established, as already outlined by Carmichael
[16]. For instance, Lissaman [78] demonstrated significant delay of flow sep-
aration on stalling airfoils by means of tripping strips, fixed at the respective
leading edges. Similarly, vortex generators and bio-inspired serrations have
been applied for airfoil flow control by Lin [75] and Ito [56], respectively.
Furthermore, lobe mixers have been proven by McComrmick & Bennett [90]
to reduce the noise through mixing in the wake of jet engines. These exam-
ples underline the importance of the nonlinear impact of convective effects,
where the introduction of small-scale structures leads to a significant change
in behaviour of the global system.

In the category of separated flows, Usherwood & Ellington [132], Rival *et al.*
[109] and Leknys *et al.* [68] investigated the influence of mild VFE modifi-
cations for accelerating propulsors. Motivated by the reports of Hertel [49]
on the dragonfly-wing leading edge, Usherwood & Ellington [132] imprinted
a spanwise saw-like structure on the VFE under consideration. This study -
most likely due to the choice of a single wavelength - did not reveal notable
influences of VFE modifications on the flow and the measured forces. Rival *et
al.* [109] and Leknys *et al.* [68] focused on small changes of the leading-edge
curvature and reported small yet measurable delays on vortex formation.

The high impact of nonlinear effects onto quasi-steady flows and the already
measurable influence of VFE modifications in the case of small VFE modi-
fications suggest that there is merit in further investigation of a wider range
of introduced disturbances in separated flows. This is supported by the ob-
servation of significant VFE modifications on propulsors in nature. The list
of examples - even though from strongly differing lineages - includes webbed
frog feet [59], the hind limbs of sea lions [115] and the tubercles on the flip-
pers of humpback whales [33]; see also figure 5.1. Note that each of those

105

VFE modifications is of distinct wavelength λ, all significantly smaller than the length scale L of the propulsor itself." [Kaiser et al., 2020b]

5.1.3 Objectives and experimental procedure

"The combined effects of VFE modification and Re scaling are investigated on the reference case of an impulsively accelerated, rigid, and circular plate of diameter D." [Kaiser et al., 2020b]

The plate is accelerated to its final velocity U_∞ within half a plate diameter of travelled distance. The plate's Reynolds number is therefore defined as

$$Re_p = \frac{U_\infty D}{\nu} \, . \tag{5.1}$$

"This canonical flow for vortex formation was recently characterised by Fernando & Rival [32] and combines several features, qualifying it as a suitable base case for this study. First, the lack of leading-edge sweep, no rotational accelerations of the propulsor and the absence of wing-tip or wing-body effects minimises three-dimensional effects during vortex formation. Thus, the influence of small scales in the flow can be observed without being superimposed by complex, global and three-dimensional flow features. Second, Fernando & Rival [31] showed that in contrast to non-circular propulsors, the circular case produces a stable vortex, which only pinches off after multiple diameters D travelled. The stable vortex allows a longer observation time and provides the possibility to investigate the effects of VFE modifications onto vortex stability. The bio-inspired VFE modifications are abstracted from the undulatory examples mentioned in §5.1.1 and modelled by adding a cosine function of different wavelengths λ with amplitude $a = \lambda/4$ onto the circular edge geometry; see §5.2.1 for more parameter details.

Early on during the onset of vortex formation, a thin layer of vorticity is produced along the VFE on the varying plates, as indicated in figures 5.2(a)–5.2(c). While the frontal area remains constant for all plates, the effective
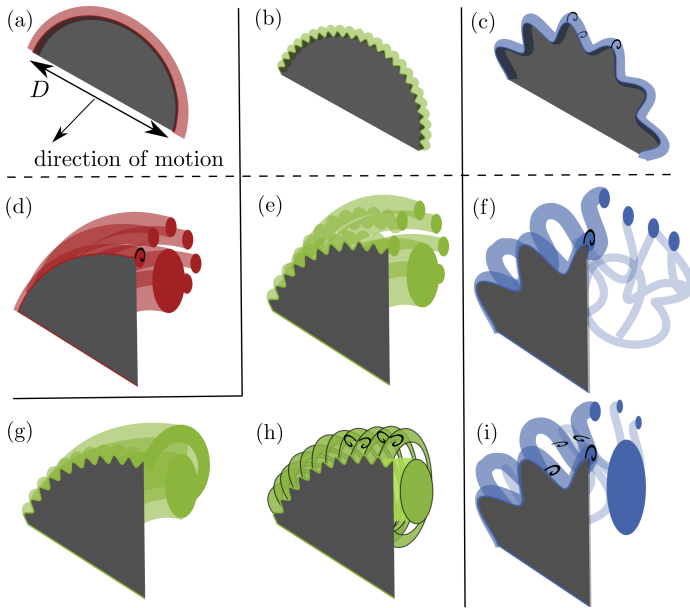
Figure 5.2: Summary of possible flow topologies around various plate geometries; (a)-(c) sketch of the shear layer directly after the onset of acceleration for different plate geometries; (d)-(i) different possible vortex formation topologies for varying Re_p and plate geometries. Figure adapted from [Kaiser et al., 2020b].

perimeters vary due to the superimposed waves. Therefore, it is expected that the magnitude and orientation of vorticity generated on the edge should vary between the different geometries. During the subsequent vortex formation, the shear layer detaches, rolls up and forms a vortex. For the circular plate, the vortex evolution is well known (see figure 5.2d). KHIs appear during the plate's acceleration and are continuously produced during the whole vortex formation process, as has been shown by Wong *et al.* [142] and Rosi & Rival [110].

A high-vorticity core remains stable until azimuthal instabilities appear and destabilise the system. The wavelength of the azimuthal instabilities and their

onset in a circular vortex ring depend on Re_p, which has been shown by Max-worthy [89] for vortices produced by a classical piston–cylinder vortex genera-tor. Fernando & Rival [32] confirmed the existence of the azimuthal instability for vortex rings in the wake of an accelerated circular plate. For the geome-tries with VFE modifications, however, the formation of the vortex wake is yet unknown. Various wakes seem possible, all of which are outlined in figure 5.2. It is hypothesised that the relation

$$B = \lambda/2\delta \qquad\qquad (5.2)$$

of the undulatory VFE modification height $\lambda/2$ to shear-layer thickness δ is a crucial relative quantity. Therefore, the flow around the plates is colour-coded accordingly in figure 5.2, where red indicates flow around a smooth circular plate, and green corresponds to VFE wavelengths in the order of magnitude of the shear-layer thickness or smaller ($B \leq 1$). The flow around plates with VFE modifications with significantly larger wavelengths is visualised in blue ($B \gg 1$). Three flow topologies seem possible for small λ ($B \leq 1$). As a trivial solution, the effects of the VFE modifications might be irrelevant or directly damped out such that the vortex formation would then appear similar as for the unmodified circular plate (see figure 5.2e). The disturbances introduced by the undulated VFE could also promote transition to a turbulent shear layer, where the presence of turbulent small-scale structures directly corrupts the forming KHIs (see figure 5.2g). Recent reports by Buchner *et al.* [14] suggest that a change of the dominant instability mechanism towards centrifugal instabil-ities (CIs) is also possible. Small-scale VFE modifications could favour the formation of CIs as indicated in figure 5.2(h). The shear layer of larger undu-latory VFE modifications λ ($B \gg 1$) might reorient towards a circle and roll up as discussed for the smaller perturbations (similar to figure 5.2e). In con-trast, a complete disruption of the vortex formation process and an expedited transition to the fully separated and turbulent state also seems possible (see figure 5.2f). However, a mixture between these above cases is most likely: a

destabilised shear layer that rolls up to a complex turbulent flow with a diffuse vortex core, as sketched in figure 5.2(i).

As a consequence of the above-outlined variety of possible flow conditions and hypotheses, the objective of the present work centres around which VFE modifications influence the unsteady vortex wake behind accelerating propulsors. A systematic variation of λ across a wide range of Re_p is performed by means of time-resolved particle image velocimetry (PIV) and force measurements in an optical towing tank. The resulting data serve as a basis to study the instability mechanisms as they occur with varying wavelength λ and/or Re_p. In particular, the footprint of the VFE modifications in the vortex formation is evaluated with respect to the resulting loading on the propulsor and the stability of the vortex wake itself." [Kaiser et al., 2020b]

5.2   Methods

The following section provides an overview of the investigated kinematics, the four geometries under consideration and the Reynolds number space. Furthermore, the testing facility, the experimental parameters, and the applied measurement techniques are outlined.

5.2.1 Kinematics and parameter space

"The kinematics and the Re_p space are chosen to match the previous study by Fernando & Rival [32]. The plates of mean diameter D are impulsively accelerated perpendicular to their orientation to a terminal velocity of U_∞ within a distance of $s^* = s/D = 0.5$, where s is the physical distance travelled. Two terminal velocities U_∞ are compared, which correspond to $Re_p = U_\infty D/\nu = 50\,000$ and $Re_p = 350\,000$ based on constant values for plate diameter D and kinematic viscosity of water ν.

Three plates with undulatory VFE modifications of varying wavelengths λ are compared to a smooth circular plate ($n_p = \infty$). The mean perimeter πD
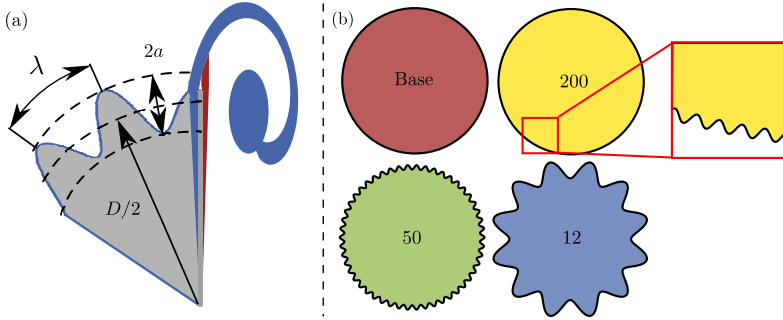
Figure 5.3: (a) Sketch of the chosen vortex-edge modification. Wavelength λ, undulatory disturbance amplitude a and mean plate diameter D. (b) Geometries with number of undulations $n_p = \infty$, $n_p = 12$, $n_p = 50$ and $n_p = 200$. Figure adapted from [Kaiser et al., 2020b].

is divided into n_p waves of length $\lambda = \pi D / n_p$. To avoid the introduction of additional (and confusing) length scales into the system, the wavelength λ and amplitude a of the introduced undulations are held constant at a ratio of $a/\lambda = 1/4$. Consequently, the radius of the modified plates is defined as

$$R(\varphi) = D/2 + \lambda/4 \cos(n_p \varphi), \qquad (5.3)$$

which is indicated in figure 5.3(a). The frontal surface area A_p of all plates is held constant, which is achieved by iteratively adjusting D. Note that the addition of the cosine function in combination with a constant frontal area A_p implies different perimeters P_p for plates of different wavenumbers $k_p = 1/\lambda = n_p/\pi D$. In particular, the influence of the number of undulations $n_p = 12$, $n_p = 50$ and $n_p = 200$, is tested. Additionally, the experiments for a circular plate ($n_p = \infty$) from Fernando & Rival [32] are repeated for reference and comparison. All plate geometries considered are shown in figure 5.3(b); the geometrical details are also listed in table 5.1. The plate with $n_p = 50$ leads to a length scale $2a$ similar to the spacing of KHIs and the shear-layer thickness δ ($B \approx 1$). Accordingly, undulatory VFE modifications with larger

110

Plate	D [m]	a [m]	n_p [-]	k_p [m^{-1}]	A_p [m^2]	P_p [m]
Base	0.300	0	∞	∞	0.707	0.942
200	0.300	0.012	200	212.2	0.707	1.39
50	0.300	0.047	50	53.1	0.707	1.381
12	0.298	0.195	12	12.8	0.707	1.423

Table 5.1: Parameters of the tested plate geometries. Table adapted from [Kaiser et al., 2020b].
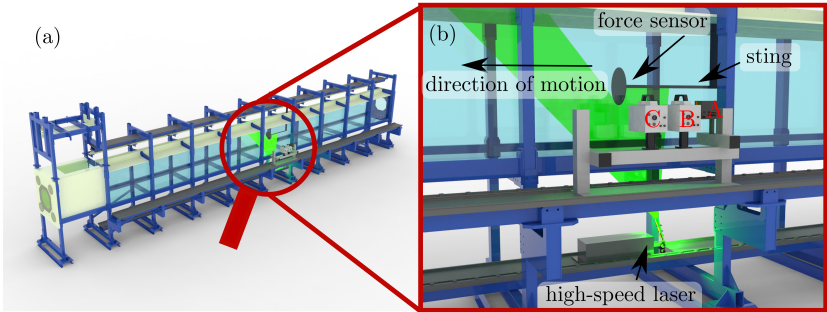
Figure 5.4: Optical towing tank (a) and PIV setup (b). The light sheet enters the tank from the bottom window; multiple high-speed cameras (A,B,C) capture the accelerating plate in a lab-fixed frame of reference. Figure adapted from [Kaiser et al., 2020b].

or smaller wavelengths ($n_p = 200$ and $n_p = 12$) introduce structures that are smaller ($B < 1$) or larger ($B > 1$) than the shear-layer thickness, respectively." [Kaiser et al., 2020b]

5.2.2 Experimental set-up

"The experiments were conducted in the 15 m long optical towing tank facility at Queen's University as shown in figure 5.4(a). The cross-section spans $1\,\text{m} \times 1\,\text{m}$ and is optically accessible from three sides. An overhead traverse is used to tow models, where an additional non-transparent semi-enclosed

111

Experiment	Re_p	force	I	II	III	IV	V	VI	VII
Base	50 000	✓	✓	✓	✓	-	-	-	-
200	50 000	✓	✓	✓	✓	-	-	-	-
50	50 000	✓	✓	✓	✓	-	-	-	-
12top	50 000	✓	✓	✓	✓	-	-	-	-
12bot	50 000	✓	✓	✓	✓	-	-	-	-
Base	350 000	✓	-	✓	✓	✓	✓	✓	✓
200	350 000	✓	-	✓	✓	-	-	-	-
50	350 000	✓	-	✓	✓	-	-	-	-
12top	350 000	✓	-	✓	✓	✓	✓	✓	✓
12bot	350 000	✓	-	✓	✓	✓	✓	✓	✓

Table 5.2: Overview of the conducted experments; roman letters I-VII corrrespond to different FOVs of the PIV setup; cp. also figure 5.5. Table adapted from [Kaiser et al., 2020b]

ceiling minimises free-surface effects. In the present study, the four plates considered were mounted onto a cylindrical sting with a diameter of $0.08D$ and length $2D$, which was further connected to the traverse by a symmetric profile of thickness $0.08D$. A six-component, submersible ATI Nano force transducer was applied between the sting and the plates to record force data at $1000\,\text{Hz}$ with a static resolution of $0.125\,\text{N}$ (see figure 5.4(b)). Every parameter combination was repeated 20 times for $s^* \leq 33$ and the data were ensemble-averaged accordingly.

Complementary to the force measurements, the flow fields in the wake of all plates were captured by means of time-resolved planar PIV, as shown in figure 5.4(b). A $2\,\text{mm}$ thick light sheet was created through a $40\,\text{mJ/pulse}$ Photonics high-speed laser, and then introduced into the tank through the bottom window. The light sheet was centred parallel to the sidewalls in the tank and was tilted towards the towing direction to avoid shadows in the wake.
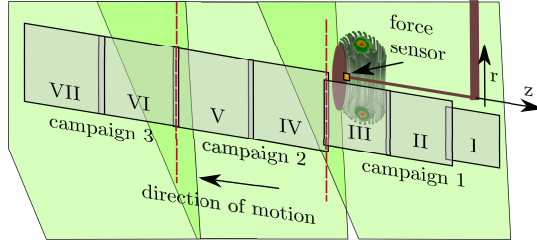
Figure 5.5: Overlapping fields of view (FOV) and campaigns of the conducted PIV experiments (plate motion from right to left). Figure adapted from [Kaiser et al., 2020b].

Three multi-camera PIV campaigns were performed in a lab-fixed frame of reference, as illustrated in figure 5.5 and listed in table 5.2. Raw images were recorded at 200 frames per second (f.p.s) for $Re_p = 50000$ and 1400 f.p.s for $Re_p = 350000$. Note that for plate 12 ($n_p = 12$) the PIV measurements were performed twice per Re_p, where the light sheet was either aligned with the maximum or with the minimum of the plate radius ($r = 169.3$ mm, $r = 129.3$ mm). These two measurements are from here on referred to as 12top and 12bot. Similar to the force measurements, 20 runs of PIV data collection were performed for each set of parameters throughout all campaigns.

Three cameras were used during the first measurement campaign to cover a combined field of view (FOV) of $s^* = 0 - 2.3$ on the bottom half of the plate (see figure 5.5). The early acceleration stage was captured in a small FOV (I in figure 5.5) of $0.7D \times 0.7D$ with a Photron Fastcam Mini WX100 (2048×2048 pixels, camera A) to ensure sufficient spatial resolution near the VFE. Two additional Photron SA4 cameras (1024×1024 pixels, cameras B & C) captured the further evolution of the vortex, where larger FOVs of $0.85D \times 0.85D$ (II & III in figure 5.5) were chosen to account for the vortex growth. All cameras were equipped with AF-S Micro-Nikkor 60 mm 1:2.8G ED lenses, which resulted in a resolution of 9.8 px/mm (FOV I) and 4 px/mm (FOVs II and III).

Owing to frame rate limitations, camera A (Mini WX100) was only used for the lower-Re_p cases. The evaluation of the first campaign (i.e. the force measurements), however, provided evidence to investigate later vortex formation stages - particularly for the high-Re_p case. This insight will be elaborated in more detail in § 5.3. Therefore, two additional PIV campaigns were performed for the circular and the $n_p = 12$ plate and the higher Re_p ($Re_p = 350\,000$). The two Photron SA4 cameras (cameras B & C) were readjusted to allow for an even larger FOV of $1.0D \times 1.0D$ and were used to measure the vortex evolution from $s^* = 2.3 - 4.2$ (campaign 2 - FOVs IV and V) and $s^* = 4.2 - 6.1$ (campaign 3 - FOVs VI and VII). The frame rates were kept identical to campaign 1, but, owing to the larger FOV, the resolution decreased to 3.4 px/mm.

The raw images were pre-processed in MATLAB in terms of ensemble-based median subtraction, edge detection and plate tracking, and masking of the shadowed area. DaVis 8.4 was used to calibrate and process the data of each camera separately. A multi-grid scheme with a final interrogation area of 32×32 pixels and 75% overlap was chosen for FOVs II–VII. FOV I was evaluated with an interrogation area of 48×48 pixels and 75% overlap. The resulting velocity fields of all 20 runs were ensemble-averaged for each FOV. Finally, all FOVs were merged on a common plate-fixed grid. Note that the interplay of accurate calibration, edge tracking and good reproducibility of the flow even allows stitching of the separate campaigns to a single FOV." [Kaiser et al., 2020b]

5.2.3 Analysis methods

"To further analyse the ensemble-averaged and merged velocity fields, various post-processing strategies are applied, each of which is outlined in this section and indicated in Figure 5.6. Hunt, Wray & Moin [55] introduced the second invariant Q of the velocity gradient tensor as a robust means to locate vortical structures [see also § 2.2.2]. Its maximum Q^{max} is frequently applied to localise the core of such structures. More recently, Graftieaux,
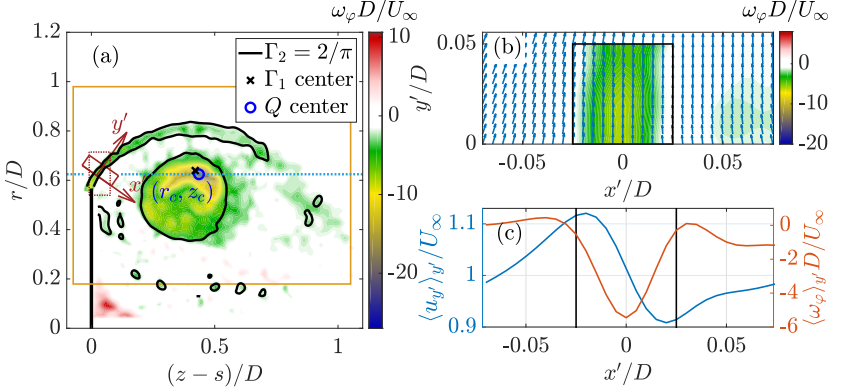
Figure 5.6: Sample processing for Case 12 top, $s^* = 3.5$. (a) Overview of applied methods: x', y'-coordinate system aligned with the shear layer (red); vortex core centers (r_c, z_c) determined with Γ_1 and Q; horizontal line through the vortex core (light blue); vortex core boundaries evaluated with Γ_2 (black); CV for total vortex circulation (orange). (b) Velocity vectors and vorticity contours of the (x', y') domain (red box). (c) Spatially-averaged profiles of velocity $\langle u_{y'} \rangle_{y'}$ and vorticity $\langle \omega_{\varphi'} \rangle_{y'}$. Black lines in b) and c) indicated the domain for the calculation of circulation flux $\Gamma_{sl}^{\cdot}$. Figure adapted from [Kaiser et al., 2020b].

Michard & Grosjean [39] proposed two criteria (Γ_1 and Γ_2) to identify the core and boundaries of vortical structures, respectively [see also §2.2.2]. Huang & Green [53] showed that Γ_1^{max} and Q^{max} lead to similar core locations in cases where the reference frame for Γ_1 was chosen appropriately, as indicated in figure 5.6(a) for a plate-fixed frame of reference. However, the location $r_c(t), z_c(t)$ of the vortex core is estimated based on the Galilean invariant Q^{max} throughout the present work to avoid any possible uncertainties resulting from reference-frame issues.

The Galilean invariant Γ_2-criterion is chosen to identify the boundaries of vortical structures for $\Gamma_2 = 2/\pi$. The core locations $r_c(t), z_c(t)$ are enclosed by one such boundary (see black line in figure 5.6a), which is referred to as vor-

tex core area A_{Γ_2}. The equivalent diameter d and corresponding circulation Γ_c of the vortex core are determined by

$$d = 2\sqrt{\frac{A_{\Gamma_2}}{\pi}} \qquad (5.4)$$

and

$$\Gamma_c = \int_{A_{\Gamma_2}} \omega_\varphi \mathrm{d}A, \qquad (5.5)$$

respectively.

An estimate of total vortex circulation Γ including the shear layer is derived from the integration of vorticity across a large control volume behind the plate, which is highlighted orange in figure 5.6(a). The lower boundary of the control volume is fixed at $r/D = 0.19$ to exclude the secondary vortex from the circulation budget. The secondary vortex occurs during the later stages of the flow and near the centre of the plate; see §5.3.

Recent reports on vortex formation evaluated the convective fluxes through a cut perpendicular to the propulsor and directly behind the flow separation to estimate the circulation flux $\dot{\Gamma}_{sl}$ from the shear layer into the vortex [26], [1]. The present work attempts to advance beyond this plate-oriented approach to overcome two shortcomings: First, the optical access to the shear layer is blocked in the immediate vicinity of the VFE for 12bot, since the plate is an obstruction in front of the light sheet due to radius changes; see (5.3). The velocity information in this region, therefore, remains unknown. Second, instabilities in the shear layer lead to a strong fluctuation of the circulation flux over time due to KHIs.

Consequently, the flux evaluation is shifted slightly leeward and away from the solid structure, and a spatial average of the shear layer is evaluated to smooth the effects of instabilities. This four-step approach is illustrated in figure 5.6. First, the average velocity of the shear layer is evaluated in the red dashed area behind the plate to determine the shear-layer orientation. This direction

is then aligned with the y'-axis of a (x',y') coordinate system. A close-up of this tilted (x',y') domain (solid red box) is shown in Figure 5.6(b). Profiles of spatially filtered velocity $\langle u_{y'} \rangle_{y'}$ and out-of-plane vorticity $\langle \omega_{\varphi} \rangle_{y'}$ along y' are shown in figure 5.6(c). The origin of x' is set to collapse with the maximum of $\langle \omega_{\varphi} \rangle_{y'}$. The spatial filter along y' minimises the influence of remaining PIV uncertainties and small-scale instabilities in the shear layer.

Despite slight shear-layer thickness variations, a band of $-0.025D < x' < 0.025D$ was found to be a reasonable and robust domain for the circulation-flux calculation, since $\omega_{\varphi} \approx 0$ in the vicinity of the shear layer:

$$\dot{\Gamma}_{sl} = \int_{x'=-0.025D}^{0.025D} \langle u_{y'} \rangle_{y'} \langle \omega_{\varphi} \rangle_{y'} \mathrm{d}x'. \tag{5.6}$$

Note that more accurate strategies to approximate the shear-layer thickness [12] do not apply for the present data, as only $\approx 5-6$ velocity vectors are found within the width of the shear layer itself." [Kaiser et al., 2020b]

5.3 Results

"First, the impact of edge undulations and Re_p scaling on the overall force histories is evaluated in §5.3.1. Complementary to force measurements, velocity and ensemble-averaged vorticity fields provide insight into the underlying flow patterns for varying VFE modifications and Re_p, as addressed in §5.3.2." [Kaiser et al., 2020b]

5.3.1 Forces

"The force histories of each run were temporally filtered with a least-squares estimator as per Savitzky & Golay [114] and ensemble-averaged across 20 runs. Subsequent normalisation of the force (drag) was performed as follows:

$$C_d = \frac{2|F_z|}{\rho A U_{\infty}^2}, \tag{5.7}$$

117

(a) $Re_p = 50\,000$

(b) $Re_p = 350\,000$
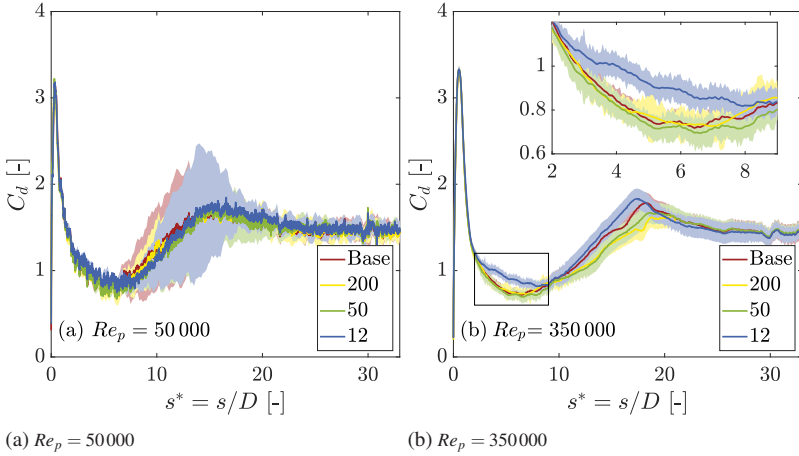
Figure 5.7: Force history $C_d(s^*)$ for all plate geometries and Re_p; the shaded area indicates the scatter through a 2σ uncertainty margin. Significant force deviations for the $n_p = 12$ plate are emphasised in the close-up of subfigure (b). Figure adapted from [Kaiser et al., 2020b].

as presented in figure 5.7. To further check the repeatability of the measurements and uncover significant case-to-case variations, two standard deviations ($\pm 2\sigma$) are added to the plots. The small uncertainty margins during acceleration, with its associated added-mass peak ($0.0 \leq s^* \leq 0.5$), relaxation stage ($0.5 < s^* < 2.5$) and the stable vortex-growth stage ($2.5 \leq s^* \leq 5$ for $Re_p = 50000$, $2.5 \leq s^* \leq 9$ for $Re_p = 350\,000$) indicate good repeatability. Once the flow destabilises and detaches from the plate, the run-to-run scatter increases by an order of magnitude, which indicates the sensitivity of this instability-triggered topology change. Finally, beyond $s^* > 20$ the fully separated and turbulent flow collapses to similar terminal values C_d, which implies that this stage is stable and highly repeatable again.

Interestingly, no significant variations of the drag coefficient are found between the circular reference plate and the small-scale modifications $n_p = 50$ and $n_p = 200$ for both Re_p - despite considerable changes in the perimeter.

Only the force history of the $n_p = 12$ plate deviates from the circular base case, which still lies within the uncertainty margin for $Re_p = 50\,000$ (see figure 5.7(a)). For $Re_p = 350\,000$, in contrast, the $n_p = 12$ plate generates a significantly higher force during the vortex-growth stage as compared to the reference and small-scale cases. A close-up of this difference is added to figure 5.7(b) so as to emphasise the 20% offset in relation to the small uncertainty margin. Note that the abscissa of the inset starts from $s^* = 2.0$, since the forces are significantly higher during the early acceleration ($s^* \leq 0.5$) and relaxation ($0.5 < s^* < 2.5$). During the acceleration, the forces collapse for identical plate cross-sections A.

The force deviation for the stable vortex-growth stage implies that the large-amplitude VFE modification of the $n_p = 12$ plate significantly influences the vortex formation process. However, the vortex topology remains similar in the wake. Consequently, the wavy shear layer still rolls up into a vortex, which remains attached to the plate for a comparable duration as with the circular reference case. To explore these differences we now turn to the flow fields." [Kaiser et al., 2020b]

5.3.2 Field data

"To compare the early vortex formation process ($1.25 \leq s^* \leq 2.25$) of the various plate geometries, the vorticity fields for all cases are shown in figures 5.8 and 5.9 for $Re_p = 50\,000$ and $Re_p = 350\,000$, respectively. Note that only selected vorticity fields are displayed here for the sake of brevity. The complete temporal evolution ($s^* < 2.3$) of all cases is provided in a supplementary movie (see Movie1.mp4) available at https://doi.org/10.1017/jfm.2019.908.

The circular plate (Base, $n_p = \infty$) and the high-wavenumber plates ($n_p = 50$ and $n_p = 200$) reveal similar results in the force measurements for both Re_p (see figure 5.7). The corresponding PIV measurements confirm these results, where the similarity of the extracted vorticity fields (see figure 5.7) indicates
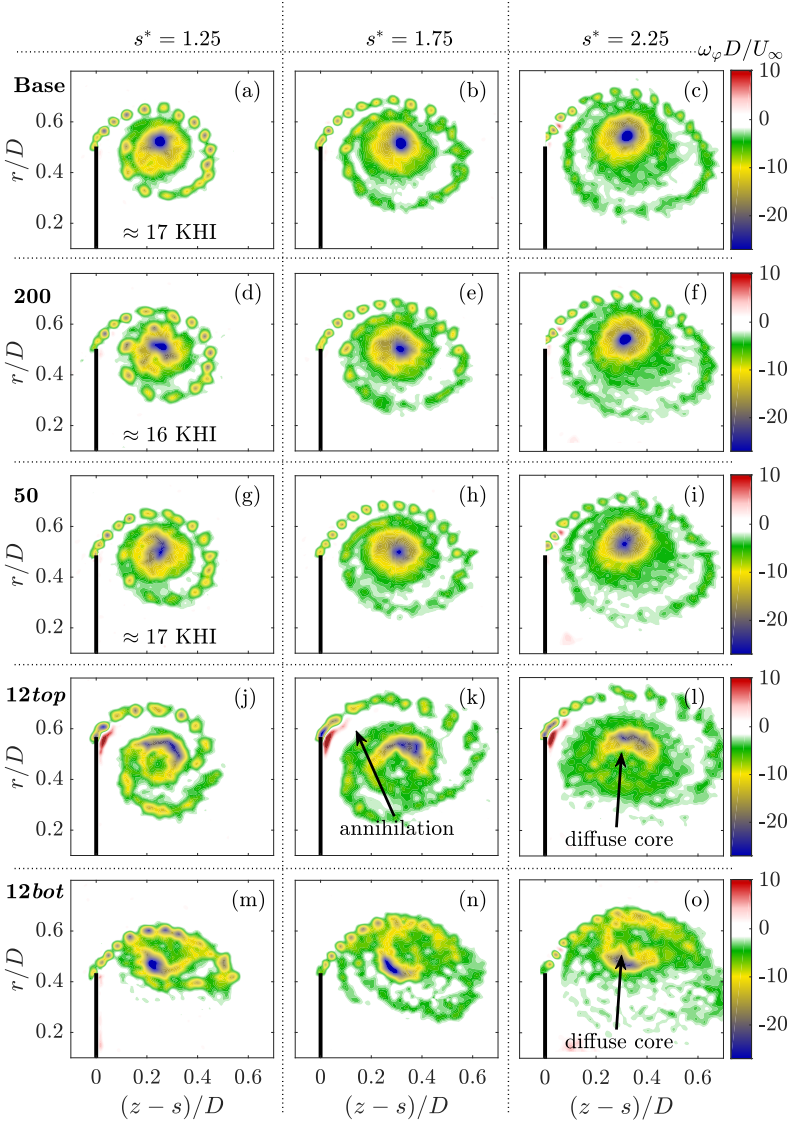
Figure 5.8: Early vortex formation at $Re_p = 50\,000$: Vorticity fields in the range of $1.25 \leq s^* \leq 2.25$ for all plate geometries. Similar results for no and small-scale VFE modifications ($n_p \in \{\infty, 200, 50\}$) - also applies for $Re_p = 350\,000$, cf. figure 5.9. KHI length-scale variation and convection of opposite-signed vorticity from the lee-ward boundary layer for large-scale VFE modifications ($n_p = 12$). Figure adapted from [Kaiser et al., 2020b].
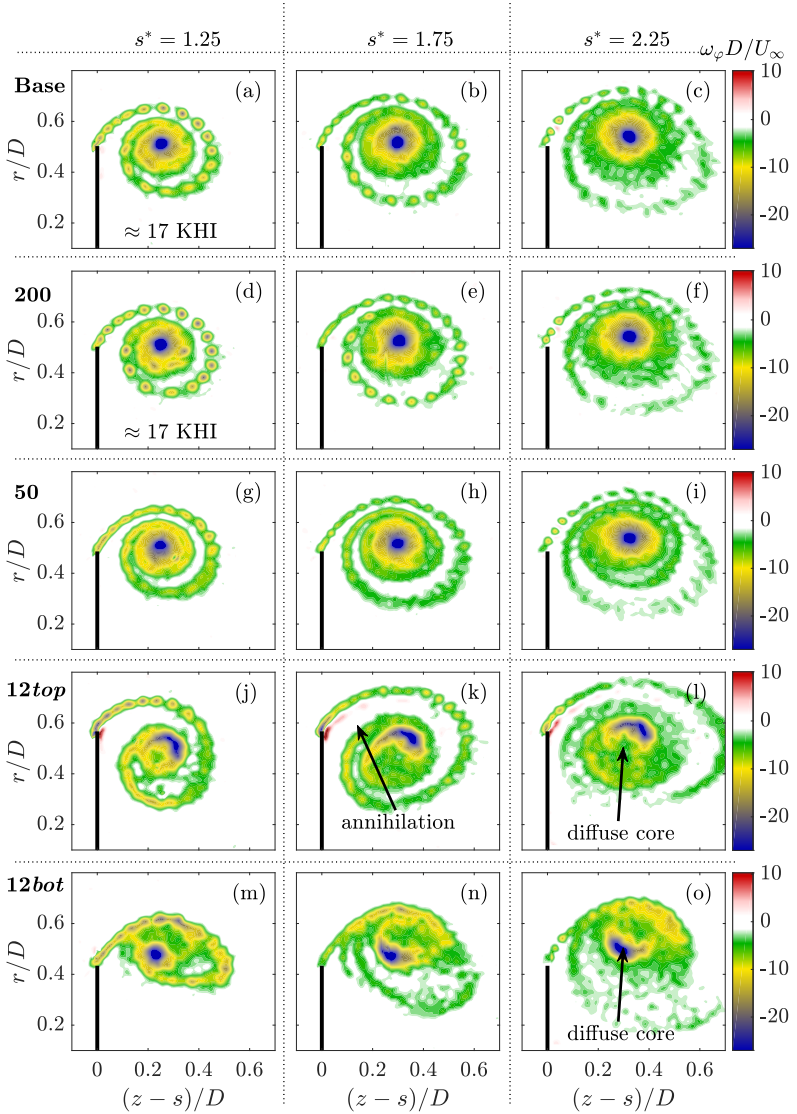
Figure 5.9: Early vortex formation at $Re_p = 350000$: Vorticity fields in the range of $1.25 \leq s^* \leq 2.25$ for all plate geometries. Similar results for no and small-scale VFE modifications ($n_p \in \{\infty, 200, 50\}$). Note that the KHI spacing remains constant for the small-scale VFE modifications ($n_p \in \{\infty, 200, 50\}$), but is reduced for $n_p = 12$ at $Re_p = 350000$ compared to $Re_p = 50000$, cf. figure 5.9. Figure adapted from [Kaiser et al., 2020b].

121
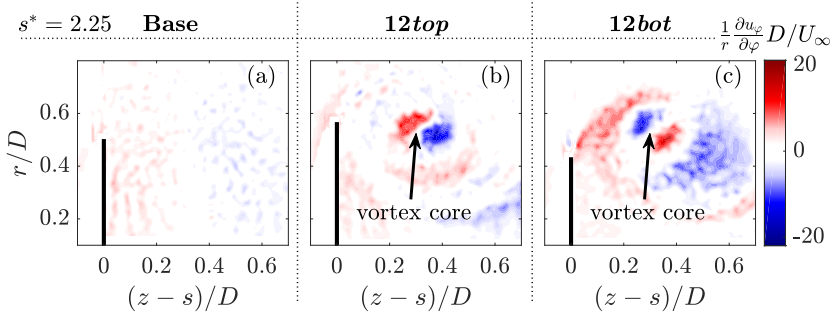
Figure 5.10: $Re_p = 350\,000$: $\frac{1}{r}\frac{\partial u_\varphi}{\partial \varphi} = -\frac{1}{r}\frac{\partial(ru_r)}{\partial r} - \frac{\partial u_z}{\partial z}$ calculated for the solenoidal velocity fields $(\mathrm{div}(u) = 0)$ at $s^* = 2.25$ for (a) the circular plate; (b) 12top; and (c) 12bot. Figure adapted from [Kaiser et al., 2020b].

that similar topologies during the early relaxation stage ($s^* = 1.25$) and during the late relaxation stage ($s^* = 2.25$) are equivalent for the three geometries ($n_p \in \{\infty, 200, 50\}$) and both Re_p. The strong repeatability of the measurements, furthermore, leads to clear visualisations of the dominant KHI. Neither disturbances smaller than the shear-layer thickness δ ($B < 1$, $n_p = 200$) nor disturbances of the same order of magnitude ($B \approx 1$, $n_p = 50$) affect the instability mechanism or lead to significant corruption of the KHI. Also, the influence of Re_p onto the instabilities is small, since the same spatial offsets of consecutive KHI structures are found in the shear layer for both Re_p; compare figures 5.8(a)-(i) and 5.9(a)-(i). It is important to mention at this point that this finding does not hold for the earlier stage of plate acceleration ($s^* < 0.5$) [110].

The similarity between the circular case and the small-scale VFE modifications ($n_p \in \{\infty, 200, 50\}$) indicates that the shear-layer formation smoothes the spanwise spatial disturbances smaller than or in the range of the shear-layer thickness ($B \leq 1$). The force histories (see § 5.3.1) and also the vorticity fields of the smallest tested wavenumber $n_p = 12$ lead to the observation that such geometrical disturbances become influential once their length scale λ exceeds the shear-layer thickness itself ($B \gg 1$).

Figures 5.8(j)-(o) and 5.9(j)-(o) present the early evolution of the vortex in the 12top and 12bot measurement plane, where the laser sheet cuts the vortex at the maximum and minimum radius of the plate, respectively. The non-circular shape of the vorticity maximum in the vortex core can be associated with significant vortex stretching. Figure 5.10 presents the out-of-plane gradient of the out-of-plane velocity $\frac{1}{r}\frac{\partial u_\varphi}{\partial \varphi}$. Furthermore, in contrast to the high-wavenumber geometries ($n_p \in \{\infty, 200, 50\}$), the main part of the vortical structure in the 12top plane is located at a smaller radius than the maximum radius of the undulated vortex edge at $R = D/2 + a$. Recent surface pressure measurements on wings by Eslam Panah *et al.* [26] and Akkala & Buchholz [1] provide evidence that this vortex position leads to an adverse pressure gradient in parts of the boundary layer between vortex and plate, which in turn results in a flux of (positive) vorticity from the plate into the vortex (see also [73]). While the positive vorticity in the boundary layer between the leeward side of the plate and the vortex wake is not sufficiently well resolved in the PIV measurements, the advected positive vorticity is clearly visible in figures 5.8(j)-(l) and 5.9(j)-(l). The advected vorticity cross-annihilates with the shear-layer vorticity and thus reduces the circulation growth of the vortex itself. In addition, this cross-annihilation also changes the wavelength of the KHI, which - in contrast to the geometries $n_p \in \{\infty, 200, 50\}$ - varies significantly between the low- and high-Re_p case. Interestingly, the 12top case comprises of significant amounts of engulfment from the irrotational outer region between the shear layer and the vortex.

Figures 5.8 and 5.9 reveal differences during the early stages of vortex formation between the high-wavenumber cases ($n_p \in \{\infty, 200, 50\}$) and the low-wavenumber case ($n_p = 12$). Despite the topological differences between these cases, the drag coefficient C_d is similar for all geometries and Re_p during the plates acceleration and the relaxation stage. Only for the high-Re_p case ($Re_p = 350\,000$) and for later stages ($s^* > 2.5$) do significant differences be-
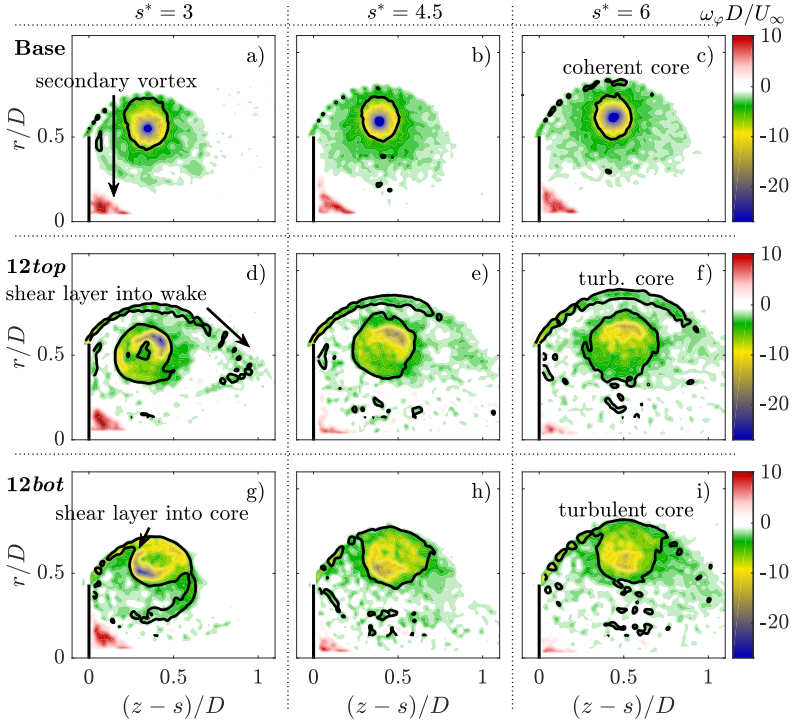
Figure 5.11: Differences in the long-term vortex formation for the circular plates and $n_p = 12$ at $Re_p = 350\,000$: Stronger shear layer, higher turbulence level and more diffuse vortex core for both $n_p = 12$ measurements compared to the circular case. Counter-rotating vortex near the axis for both cases. Black lines: vortex boundaries of $\Gamma_2 = 2/\pi$. The connected area A_{Γ_2} around the maximum vorticity core is defined as the vortex core (cf. § 5.2.3). Figure adapted from [Kaiser et al., 2020b].

tween the cases exist, which in turn motivated the additional PIV experiments for $2.3 \leq s^* \leq 6$ and $Re_p = 350\,000$; cf. § 5.2.2.

The resulting vorticity fields for the circular and $n_p = 12$ plates are shown in figure 5.11 and are available in a supplementary Movie (see Movie2.mp4). A secondary vortex appears near the plate centre in all measurements. In comparison with figure 5.9 the shear layer weakens for both cases. Yet the shear layer remains more pronounced for the non-circular plate ($n_p = 12$). However,

the interaction of shear layer and vortex core varies between the circular and the non-circular plate. At $s^* = 3$, the shear layer of the circular plate gets deflected by the vortex core, convects around the vortex center, and eventually merges with the low-vorticity region in the core vicinity. At the largest plate radius of the low-wavenumber plate (12top), the shear layer is furthest from the core, where parts of the shear layer even start to convect into the wake from $s^* = 3$; see figure 5.11(d) and supplementary movie Movie2.mp4. In contrast, the shear layer at the smallest plate radius (12bot) directly convects into the vortex core, as indicated in figure 5.11(g)-(i). The vortex core behind the circular plate remains coherent within the measured FOV $s^* < 6$. The vortex core boundaries – as introduced in § 5.2.3 – enclose a small area where rotation dominates shear. The corresponding core boundary for the $n_p = 12$ plate appears larger and accordingly comprises a more diffuse vortex core. Furthermore, the area of the overall vortex is larger, while its maximum vorticity is smaller due to turbulent mixing. The secondary vortex near the $n_p = 12$ plate centre is found to be corrupted and, therefore, less pronounced as compared to the circular plate." [Kaiser et al., 2020b]

5.4 Discussion

"This section focuses on a quantitative comparison between vortex formation on the plate with wavenumber $n_p = 12$ and the circular base case. Simple models are applied to elucidate the physics behind the most important observations stated in § 5.3 and the influence of the ratio B; see (5.2). First, the changes in shear layers for varying plate geometries, and their effects on the vortex circulation are analysed (§ 5.4.1). Second, a discussion on how the vortices stay attached to the plate for similar periods of time, even though the vortex wake behind the $n_p = 12$ plate is significantly less coherent (§ 5.4.2), is presented. Finally, the physical mechanism behind the changes in force is addressed (§ 5.4.3) by considering the momentum and size of the vortex wake and estimating the pressure in front of and behind the plates." [Kaiser et al., 2020b]
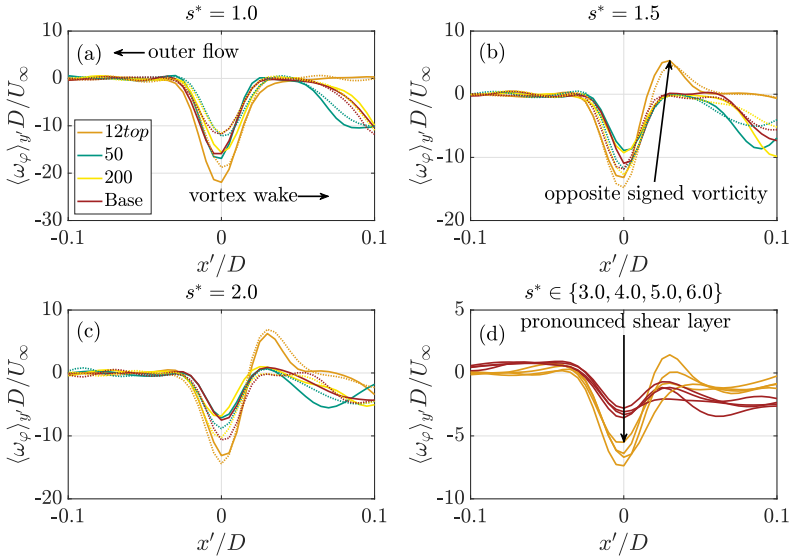
Figure 5.12: Vorticity distribution directly after the plate and perpendicular to the flow (see figure 5.6) for $Re_p = 50\,000$ (dotted line) and $Re_p = 350\,000$ (solid line) for different s^* and geometries. Left of the shear layer: vorticity free outer flow. Right of the shear layer: vortex wake

5.4.1 Feeding shear layer and vortex wake circulation

"When recalling the similar spacing of KHIs (figures 5.8 & 5.9), it was hypothesised that the shear-layer thicknesses δ for both Re_p under consideration would be similar. This is confirmed in figure 5.12. Applying the methods introduced in § 5.2.3, figure 5.12 presents the averaged vorticity distribution perpendicular to the shear layer. No significant influence of Re_p on the shear-layer thickness δ is observed.

The similarities between all high-wavenumber plates ($B \leq 1$, $n_p \in \{\infty, 50, 200\}$), as observed in §§ 5.3.1 and 5.3.2, are confirmed. In contrast, the maximal vorticity in the shear layer is consistently higher for the $n_p = 12$ plate ($B \gg 1$). However, with regards to the temporal change of circulation in the vortex, the

126
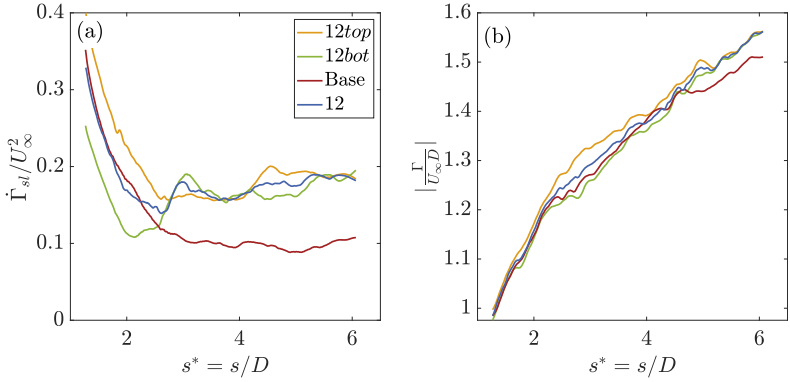
Figure 5.13: (a) Circulation flux through the feeding shear layer $\dot{\Gamma}_{sl}$ for $1 < s^* < 6$ for the varying cases at $Re_p = 350\,000$. Blue lines depict the average of 12top and 12bot. (b) Accumulated circulation in the vortex wake for $1 < s^* < 6$.

higher vorticity in the shear layer is balanced by a flux of oppositely signed vorticity from the leeward side of the plate during the early stages (figures 5.12b,c), as parts of the fed vorticity are directly annihilated. For the later stages of the vortex-formation process ($s^* > 2.5$) less vorticity diffuses from the leeward boundary layer (see figure 5.12d). Yet the shear layer is still more pronounced compared to the circular plate. As a consequence, the circulation fed through the shear layer is higher for $n_p = 12$ than for the other plates.

Applying (5.6), the circulation flux through the shear layer is evaluated. Figure 5.13(a) shows, as expected, high $\dot{\Gamma}_{sl}$ during the early stages, where the forces are also higher. During the stable vortex growth ($s^* > 2.5$), $\dot{\Gamma}_{sl}$ remains fairly constant for each geometry. However, the circulation flux of the low-wavenumber plate ($n_p = 12$) is higher than for the circular reference case. The overall circulation behind the plate, and as such in the vortex wake, is captured in figure 5.13(b). Despite the differing circulation flux through the feeding shear layers, the temporal development of overall circulation in the vortex is similar. A superposition of various circulation-reducing mechanisms in the vortex itself is hypothesised as mechanisms to limit the circulation growth:
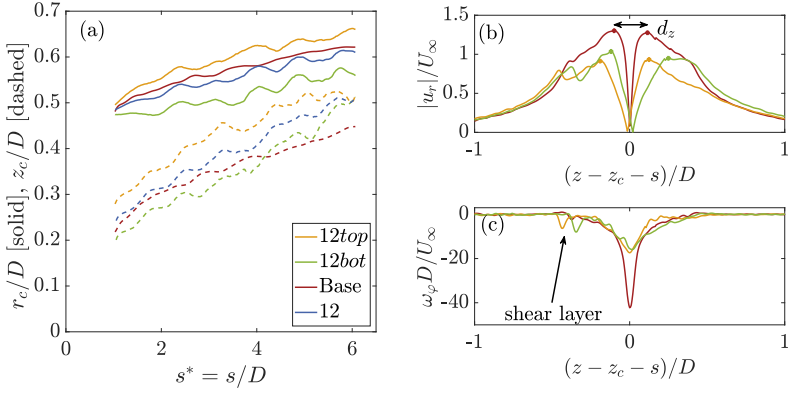
Figure 5.14: $Re_p = 350\,000$: (a) vortex-center position based on the maximum of the Q-criterion. The blue line depicts the average of 12top and 12bot. (b) $s^* = 5$: Magnitude of radial velocity along a horizontal cut through the vortex center estimated by the Q-criterion. The distance between the two maxima defined as the vortex-core diameter d_z. (c) $s^* = 5$: Vorticity along a horizontal cut through the vortex core.

- reorientation of vorticity, followed by cross-annihilation in the turbulent vortex wake;

- loss of circulation due to convection of vorticity into the wake;

- interaction and cross-annihilation of vorticity in the primary vortex with the vorticity in the secondary vortex; and

- interaction of the vortex with the boundary layer on the leeward side of the plate.

The above mechanisms are more pronounced in the highly turbulent wake of the non-circular geometry ($B \gg 1$, $n_p = 12$) and, as such, compensate for the higher $\dot{\Gamma}_{sl}$. As a consequence, there only remain small differences in the overall circulation budget (see figure 5.13b)." [Kaiser et al., 2020b]

5.4.2 Vortex core and its stability

"The position of the vortex centre is estimated by the maximum of the Q-criterion (see § 5.2.3) and is presented in figure 5.14(a). The undulatory shape of the low-wavenumber plate ($n_p = 12$) influences the vortex core radius r_c and its distance from the plate z_c. Relative to the circular plate (Base), r_c is either larger (12top) or smaller (12bot). Yet the average position (blue solid line) is similar to the radial position of the circular plate's vortex center. However, the axial position z_c increases more quickly for the low-wavenumber plate $n_p = 12$ than for the circular plate (dashed lines).

The distinct r_c values in the 12top and 12bot plane suggest an undulatory shape of the vortex wake, which most likely results in a significant radial vorticity component ω_r in between the measurement planes 12top and 12bot and induces stretching of the vortex core as depicted in figure 5.10. The stretching contributes to the qualitative differences between the different plates concerning the coherence, symmetry and size of the vortex core reported in § 5.3.2 and further discussed utilising figure 5.14(b) and (c). The magnitude of velocity ($|u_r|$) and the vorticity (ω_φ) are presented in a horizontal cut through the vortex centre (r_c, z_c) (see dashed blue line in figure 5.6). Note that while u_r is the radial velocity in the coordinate system introduced in § 5.2, it also represents the azimuthal velocity of the vortex wake itself.

Maxworthy [89] defines the horizontal distance between the velocity peaks on both sides of the vortex core as the core diameter d_z (see figure 5.14b). This d_z provides similar results as the reduced vortex core diameter d defined in § 5.2 (see figures 5.15a,b). The vorticity peak of the circular plate's vortex is higher, while its diameter d_z is significantly smaller as for the plate with $n_p = 12$.

As mentioned in § 5.1.2, Maxworthy [88] related the laminar-to-turbulent transition of a vortex ring with an azimuthal instability. The vortex core of diameter d develops a wavy structure along the ring with radius r_c (similar to the shape of the geometries in this study), which amplifies in time and finally
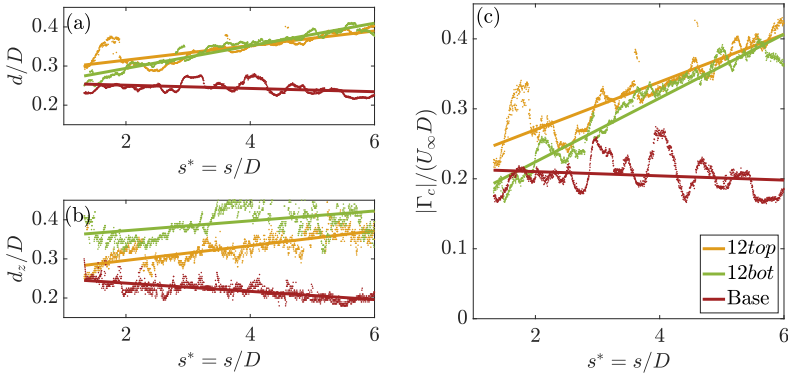
Figure 5.15: $Re_p = 350\,000$: (a) Reduced vortex-core diameter d estimates (based on Γ_2); and (b) d_z estimated by the distance of the maxima in figure 5.14(b). (c) Circulation in the vortex core as identified by the boundary $\Gamma_2 = 2/\pi$.

corrupts the vortex core itself. The onset and wavelength of the azimuthal instability depends on Re_p. Counter-intuitively, smaller Re_p lead to an earlier onset of the instability [89]. While the findings of Maxworthy are based on careful analysis of piston–cylinder vortex generators, Fernando & Rival [32] captured the same instability mechanism for the vortex formation on a circular plate and observed an earlier vortex pinch-off for smaller Re_p. Combining the earlier vortex pinch-off for smaller Re_p observed by Fernando & Rival [32] with the earlier onset of the instability for smaller Re_p observed by Maxworthy [89] suggests a causal relationship between the vortex core corruption and the vortex pinch-off. The core transition leads to reorientation of vorticity, followed by cross-annihilation and eventually a reduced circulation Γ_c in the vortex core. Furthermore, the additional mixing results in a more diffuse (and as such larger) vortex core.

Figure 5.14(b) supports modelling the vortex core as a Rankine vortex, and thus its core as a solid-body rotation. Applying this model, the pressure differ-

ence between the vortex centre $p(r_c, z_c)$ and the pressure at the core boundary $p(r_c, z_c + d/2)$ can be estimated by

$$p(r_c, z_c) - p\left(r_c, z_c + \frac{d}{2}\right) = -\frac{\rho \Gamma_c^2}{2\pi^2 d^2}, \tag{5.8}$$

where Γ_c is the circulation of the core. Equation (5.8) clarifies that both effects of transition, the reduction of $|\Gamma_c|$ as well as the increasing core diameter d, decrease the magnitude of the pressure minimum in the core. This leads to vortex pinch-off as the attracting forces from the vortex core towards the plate are eventually insufficient to avoid pinch-off.

While explaining the Re_p scaling of the vortex stability in the wake of a circular plate, the chain of events described above contradicts at first glance the fact that the vortex behind the $n_p = 12$ plate is stable. For this geometry, even before the onset of an azimuthal instability, the vortex core is already turbulent. This turbulence leads to a growth of the vortex core size: d and d_z (figure 5.15a,b). Hence, according to (5.8), a comparable core pressure minimum similar to the circular plate can only exist if the core circulation also grows in time. The magnitude of core circulation $|\Gamma_c|$ (see (5.5)) is shown in figure 5.15(c). While $|\Gamma_c|$ slightly decreases over time for the circular plate, $|\Gamma_c|$ increases in the vortex core of the $n_p = 12$ plate. The growth of $|\Gamma_c|$ results from the direct merging of shear layer and vortex core at the lowest plate radius (12bot, see § 5.3.2 and in particular figure 5.11(g-i). As a consequence, even though the vortex formation and as such the physics behind the stabilisation are distinct, the magnitude of the pressure minimum is similar for both plate geometries and both vortex cores stay attached to the plate."
[Kaiser et al., 2020b]

5.4.3 Propulsion force

"The quantitative evaluation of the vortex wake circulation Γ (figure 5.13(b)), the radial position of the vortex centre r_c (figure 5.14a), and the approximate
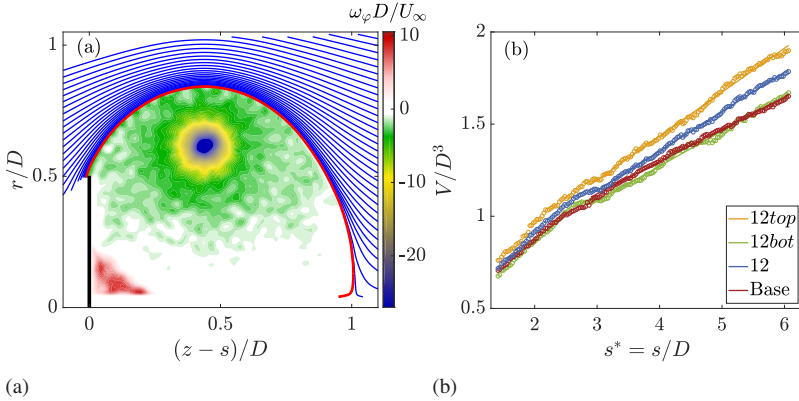
Figure 5.16: (a) Vortex-size estimation based on the outer streamlines of the vortex; here shown at $s^* = 6$ for the circular plate at $Re_p = 350\,000$. The red line denotes the estimated vortex boundary. (b) Vortex volumes shown for the varying cases at $Re_p = 350\,000$ over traveled distance of the plate s^*. Blue lines represent the average of 12top and 12bot.

pressure at the vortex centre (5.8) provide similar results. As such, the physical phenomenon behind the force enhancement up to 20% (see § 5.3.1) for the small-wavenumber plate ($n_p = 12$) as yet remains unclear and is addressed in the following. Two distinct approaches to reconstruct forces from the measured data are applied. First, the momentum of the flow is discussed. It provides an intuitive explanation for the force enhancement but does not resolve the measured propulsion force to its full extent. This is achieved by the second approach, i.e. the evaluation of the pressure at the plate's surface.

Motivated by the different observed vortex sizes during the later stages of the measurement (see figure 5.11), a simple model is applied to estimate the influence of vortex volume growth on the rate of change of momentum and as such the propulsion force. By assuming the vortex of growing volume V travels with approximately the same velocity as the plate U_∞, the momentum in the axial direction can be split into the contribution of the vortex momentum,
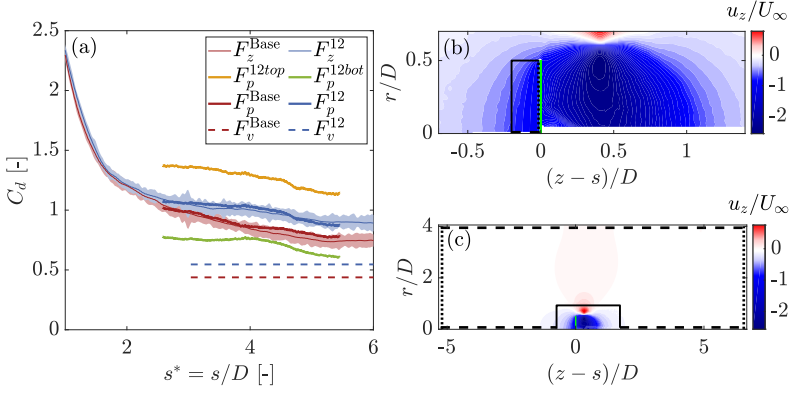
Figure 5.17: (a,b) Combined measured and reconstructed velocity data, which is utilised for the pressure evaluation: (a) shadowed area in front of the plate and (b) the far-field extending the FOV of the measurement. The areas of potential flow solution and their respective Neumann boundary conditions are highlighted: measured velocity data (solid lines), $u_r = 0$ (dashed lines), $u_z = 0$ (dotted lines). The plate is position is depicted in green. (c) Propulsion force at $Re_p = 350\,000$ measured by the force transducer (F_z; same as figure 5.7(b)), estimated by the plate's surface integral of the pressure (F_p) and by the rate of change of vortex momentum ($F_v = \rho \dot{V} U_\infty$). Figure adapted from [Kaiser et al., 2020b].

$I_v = \rho V U_\infty$, and the momentum of the also time-dependent flow outside of the vortex, I_o:

$$I_z = I_v + I_o = \rho V U_\infty + I_o. \qquad (5.9)$$

During the later stages of vortex formation ($s^* > 2.5$), where distinct forces were measured for the different geometries, the plate velocity U_∞ is constant. The approximated force results in

$$F_z = \dot{I}_z = F_v + F_o = \rho \dot{V} U_\infty + \dot{I}_o, \qquad (5.10)$$

where $F_v = \dot{I}_v = \rho \dot{V} U_\infty$ and $F_o = \dot{I}_o$.

The fluid mass ρV, which travels with the plate, and as such can be considered as part of the vortex, is analysed in the following. Multiple mechanisms

lead to a growing vortex mass ρV. The vorticity-containing shear layer feeds mass into the vortex volume [140]. In addition, turbulent entrainment [111], as well as engulfment of inviscid fluid (e.g. figure 5.9), adds additional mass to the vortex core. The additional fluid, which subsequently travels with the propulsor, also requires momentum. Similar to the findings of McPhaden & Rival [91], equation (5.10) suggests that the change of vortex volume influences the propulsion forces. To approximate the instantaneous vortex volume V, the topology of the flow is analysed. The streamline originating in the node behind the plate is identified (red line in figure 5.16a) and the underlying vortex volume is defined as V. Figure 5.16(b) shows the temporal evolution of the vortex volumes. The large disturbances due to the undulatory VFE of plate 12 result in a turbulent vortex wake and thus in additional entrainment. For the small-wavenumber plate ($n_p = 12$), the volume is estimated by linear interpolation between the results from 12top and 12bot. A linear fit on V (figure 5.16b) is utilised to estimate the force contribution F_v of the growing vortex wake of the respective geometries (F_v^{12} and F_v^{Base}) in the interval $3 \leq s^* \leq 6$; see figure 5.17(a). The trends of the reconstructed forces F_v are consistent with the trends of the forces measured by the force transducer F_z; i.e. $F_v^{12} > F_v^{Base}$. However, F_z is not reproduced to its full extent as the contribution of F_o is unknown and missing.

To obtain a more accurate force reconstruction, the pressure distribution at the plate is estimated. Multiple steps are performed for each dataset: the circular plate (Base), 12top and 12bot:

1. The area directly in front of the plate was not captured as the plate itself casts a shadow (see figure 5.4b). The flow field in the shadowed area is reconstructed by employing a two-dimensional potential flow solver. As presented in figure 5.17(b), the measured velocity data (solid lines), the impermeability of the plate (dotted line) and the symmetry of the flow (dashed line) are utilised as Neumann boundary conditions (NBC).
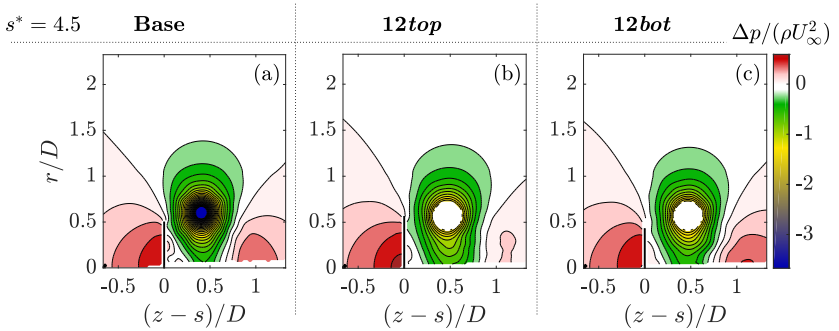
Figure 5.18: $Re_p = 350\,000$: Pressure fields evaluated by means of the ensemble-based approach of Kling *et al.* [64] at $s^* = 4.5$ for (a) the circular plate; (b) 12top; and (c) 12bot. The vortex wake of the circular plate shows steeper pressure gradients, resulting in a higher pressure at the leeward side of the plate and as such a smaller propulsion force. Due to the unknown out-of-plane velocity/gradients in the highly three-dimensional vortex core of the undulated plate (see figure 5.10), the core area is excluded from the pressure calculation for 12top and 12bot. Figure adapted from [Kaiser et al., 2020b].

2. In addition, the potential flow solver is used to extend the limited FOV of the measurement. NBC are applied at the boundaries of the flow area of interest (see figure 5.17c). While the measured velocity data provide NBC at the FOV boundaries (solid lines), the far-field NBC are estimated to be $u_r = 0$ at the upper and lower boundaries (dashed lines) and $u_z = 0$ at the windward and leeward boundaries (dotted lines). Note that these far-field NBC are only an approximation. To reduce the influence of these imperfect NBC a large area of $13D \times 4D$ is selected to reconstruct the far field.

3. The pressure field p is evaluated by applying the ensemble-based pressure estimation method of Kling *et al.* [64]. An ensemble-based Reynolds decomposition is applied on the divergence of the momentum equation. Kling *et al.* [64] calculate the Reynolds stresses by means of the variance and covariance of the ensemble-averaged data at a single time instant. As only 20 runs were performed in the present experiment, the method is extended by an additional moving temporal average in the

135

plate-fixed frame of reference over 100 time steps. Furthermore, due to the two-dimensional measurements in the present study, u_φ, $\partial u_r/\partial \varphi$ and $\partial u_z/\partial \varphi$ are unknown. Therefore, for the undulated plate the vortex core is excluded from the pressure reconstruction, as significant out-of-plane gradients exist in this region (see figure 5.10). The far-field solution estimated in the previous step of the calculation allows application of the required Dirichlet boundary condition $p_0 = const.$ far away from the plate, in particular at the upper boundary of the far-field solution. The NBC are derived from the momentum equations. The estimated pressure fields $\Delta p = p - p_0$ are presented in figure 5.18 for $s^* = 4.5$.

4. The reconstructed axial force resulting from the pressure field F_p is evaluated by integration of the pressure along the plate's front and back surfaces:

$$F_p = \int_{A_{front}} p\mathrm{d}A - \int_{A_{back}} p\mathrm{d}A. \qquad (5.11)$$

The net force on the undulatory plate ($n_p = 12$) is estimated by averaging between the two measurement planes $F_p^{12} = F_p^{12bot} + F_p^{12top}$.

Despite the limitations of the two-dimensional data and the limited number of measurement planes, the estimated forces F_p closely resemble the forces measured by the transducer F_z (see figure 5.17a). This good agreement of the integral value provides evidence to further interpret the instantaneous pressure fields presented in figure 5.18: The larger and more diffuse vortex core in the wake of the undulatory plate results in less steep pressure gradients and thus in a lower pressure at the leeward side of the plate, which in turn explains the higher propulsion force." [Kaiser et al., 2020b]

5.5 Summary

"The convergence of unsteady propulsion in nature for a broad range of Re_p at first glance suggests a minor impact of turbulence and small-scale structures

on vortex formation. Conversely, recent studies on free shear layers and the influence of Re_p on entrainment refute this argument. This study explores the impact of small-scale coherent structures on vortex formation. This problem is on the one hand addressed by performing measurements for a wide range of Re_p, where at higher Re_p it is expected that the size of the smallest structures in the flow will be reduced. On the other hand disturbances of distinct wavelengths λ are introduced into to flow. Motivated by varying undulations on propulsors of swimming animals, the disturbances are introduced into the flow by modifying the VFE of accelerating low-aspect-ratio plates. The relation $B = \lambda/2\delta$ (see (5.2)) hereby describes the height of the undulation $\lambda/2$ relative to the length scale of the shear-layer thickness δ. As such, this study explores the influence of varying edge undulation on vortex formation over a wide ranges of B and Re_p.

Conclusions relating to the scaling of B and Re_p are categorised below with regard to vortex stability and forces on the propulsor.

1. The influence of edge undulations strongly depends on the relation B. The shear layer and, as such, the forming vortex are found to be insensitive to VFE modifications smaller than similar to the shear-layer thickness δ. The vortex formation process is only affected significantly for large-scale VFE modifications ($B \gg 1$).

2. For $B \gg 1$, the force is increased during the stable vortex-growth stage. Up to 20% higher forces are measured in the present study. A change in vortex volume growth and a more diffuse vortex core are identified as the cause of these variations. This observed increase in force is likely one cause for the undulatory VFE modifications observed in nature.

3. For all geometries tested here, the wake vortices remain stable over an equivalent normalised distance. Yet a different mechanism stabilises the vortex for large λ ($B \gg 1$). The vortex wake for the circular base case depends on the coherence of its vortex core to remain stable. Transition due to azimuthal instabilities leads to vortex pinch-off. For larger

VFE modifications $B \gg 1$ the vortex core is turbulent from the start. However, the circulation of the turbulent and spatially expanding core grows continuously, preserving the magnitude of the required pressure minimum inside the core.

4. For small VFE modifications ($B \leq 1$) other than the known Re scaling associated with the azimuthal instability [32] no additional scaling was observed. In accordance with findings on quasi-steady free shear layers [50], neither the spacing of KHIs nor the shear-layer thickness δ vary within the available accuracy of the data and within the Re_p range under consideration. The existence and the effects of coherent structures that are significantly smaller than the observed KHIs, cannot be evaluated with the available data. Repeating the high-resolution particle-tracking experiments of [111] for the quasi-steady regime of the flow could provide insight if additional entrainment due to very small structures occurs at high Re_p. In contrast, for the case of $B \gg 1$, higher Re_p leads to smaller spacing of the KHIs. Following the model of [110], the smaller spacing could result in higher entrainment, a faster-growing vortex volume, and consequently a higher overall force. As such, the higher impact of coarse VFE modifications in cases of larger Re_p can be motivated by the observed smaller KHI spacing." [Kaiser et al., 2020b]

6 Conclusion and Outlook

This thesis focused on the influence of turbulence on vortex formation and decay. In particular, the interaction of vortical structures with solid boundaries is investigated in detail over a wide range of *Re*. With the vortex formation in bio-propulsion as a guiding example, a variety of mechanisms, that result from the interaction of a solid (propulsor) with a surrounding fluid, are identified in chapter 1. Subsequently, three studies are presented that isolate and simplify specific features. The simplifications allow for a detailed analysis of each respective mechanism without interactions with other aspects of the usually highly three-dimensional flow in the vicinity of a non-simplified propulsor.

The findings for each study are summarised at the end of the respective chapter. Thus, the present section reiterates only selected conclusions and synthesises the studies with regard to their implications for vortex formation and decay in more complex configurations such as vortices in bio-propulsion.

In chapter 3 the boundary layer between a vortex and a solid (e.g. a propulsor) is investigated numerically. In particular, its unique feature of oppositely-signed vorticity is addressed in detail by a spectral DNS of the vortex decay from SBR due to decelerated cylindrical walls at its boundary. The mechanism of transition to turbulence due to centrifugal instabilities is visualised by means of LCS. Furthermore, the effects on the transport of vorticity, turbulent kinetic energy and mean kinetic energy are evaluated throughout the five stages of the flow: laminar boundary-layer formation, transition to turbulence, turbulent state with intact vortex core, vortex-core corruption, and finally, the relaminarisation. As vorticity annihilation in bio-propulsion is limited to the time period of a stroke, the latest stages (IV and V) of vortex decay

are unlikely to become relevant in nature. However, the early stages (I-III) of the spin-down experiment provide insights into phenomena that are likely to occur in the suction-side boundary layer of a propulsor. The time scale of boundary-layer growth remains proportional to $\sqrt{\nu t}$ before and after transition to turbulence for all Re. However, the proportionality constant scales with the Reynolds number such that $a_{turb}/a_{lam} \sim Re^{1/3}$ (3.22). For increasing Re, the earlier transition $\theta_o \sim Re^{-4/3}$ in combination with larger a_{turb} in parts compensates for the reduced effects of viscosity, and leads to similar decay rates of the core circulation Γ_c and the core pressure for a wide range of Re (see § 3.6.6) during the early stages of the vortex decay.

As the Re range of the DNS in chapter 3 is limited ($Re \leq 2.8 \cdot 10^4$), in chapter 4 results from two experimental campaigns are reported, which were designed to achieve very high Re. The Re range of the experiments ($Re \leq 4 \cdot 10^6$) herby matches the scales of vortices produced by medium to large-sized swimmers in nature. Due to the expected scaling of the transition onset time, $\theta_o \sim Re^{-4/3}$, and the scaling of the length scale of the instabilities, $\lambda_c/R \sim Re^{-2/3}$, the experiments had to be performed at a large-scale facility. The one-of-a-kind, CORIOLIS II platform in Grenoble provided the required dimensions. Despite the diminishing effects of curvature (small δ_{99}/R) during transition to turbulence for very high Re, the centrifugal instability persists for very high Re and the expected scaling of θ_o is confirmed. As such, centrifugal instabilities are expected to occur in bio-propulsion also for only mildly curved streamlines and beyond the medium Re range, where Buchner *et al.* [14] reported their existence. Furthermore, it was shown that a saturated salt-water layer at the bottom of the cylinder reduces end-wall effects to such an extent that sensible information on the side-wall boundary layer could be measured up to stage III. As a result, this novel technique provided a means to confirm the scaling of a_{turb}/a_{lam} (see § 4.4.2).

Finally, chapter 5 presented the influence of different turbulent scales on the shear layer and the core of a forming vortex. The experimental cam-

paign, performed in a 15 m-long towing tank at Queen's University, captures the vortex evolution in the wake of circular and undulated plates, respectively. Hereby, the plate's Reynolds number (Re_p) is varied in the range $50\,000 \leq Re_p \leq 350\,000$. In addition, edge undulations of different wavelengths λ are tested, which introduce flow structures of varying size. After the plate has reached its final velocity, no influence of Re_p on the shear layer could be detected at the given accuracy of the measurements. KHIs of similar spacing and similar shear-layer thicknesses are observed. However, Re_p influences the spatial extent of the vortex core and as such the long-term stability of the vortex ring (see § 5.4.2). The effects of edge undulations are found to be negligible if the undulations are smaller than the shear-layer thickness ($B = \lambda/2\delta < 1$; cp. (5.2)). However, large-scale undulations ($B \gg 1$) introduce flow structures that influence the vortex core and also the entrainment rate through the shear layer. It is shown that edge undulation can increase entrainment and therefore the growth rate of the vortex itself. As a consequence, the plate with the largest tested undulations provides an up to 20% increase in the propulsion force (see § 5.4.3).

The work presented in this thesis took a fundamental approach to unravel some of the effects of turbulence on the unsteady phenomena of vortex formation and decay. However, by reducing the complex and three-dimensional problem of vortex formation in bio-propulsion to the canonical flows investigated in this thesis, many effects are neglected. Propulsor flexibility, more complex propulsor shapes and three-dimensional kinematics are known to impact vortex formation as well. Future work should address the interaction of such influences on the scaling of the suction-side boundary layer as well as on the effects of edge undulation.

On a final note, the author wishes to emphasise the potential of the spin-down problem for fundamental research on turbulence and transition. For example, its canonical nature as the equivalent of Stokes' first problem for curved walls (cp. § 2.3.1), the unique TNTI during spin-down with vorticity on both

sides, and its close relation to the Taylor-Couette problem provide merit for further investigations.

Bibliography

[1] J. M. Akkala and J. H. J. Buchholz. Vorticity transport mechanisms governing the development of leading-edge vortices. *J. Fluid Mech.*, 829:512–537, 2017.

[2] A. Babiano, C. Basdevant, B. Legras, and R. Sadourny. Vorticity and passive-scalar dynamics in two-dimensional turbulence. *J. Fluid Mech.*, 183:379–397, 1987.

[3] R. S. Barlow and J. P. Johnston. Structure of a turbulent boundary layer on a concave surface. *J. Fluid Mech.*, 191:137–176, 1988.

[4] G. K. Batchelor. *An introduction to fluid dynamics*. Cambridge Univ. Press, Cambridge, 1967.

[5] B. J. Bayly. Three-dimensional centrifugal-type instabilities in inviscid two-dimensional flows. *Phys. Fluids*, 31:56–64, 1988.

[6] E. R. Benton and A. Clark Jr. Spin-up. *Annu. Rev. Fluid Mech.*, 6:257–280, 1974.

[7] A. Bertram and R. Glüge. *Solid Mechanics: Theory, Modeling, and Problems*. Springer, Heidelberg, 2015.

[8] M. Bilson and K. Bremhorst. Direct numerical simulation of turbulent Taylor–Couette flow. *J. Fluid Mech.*, 579:227–270, 2007.

[9] H. Bippes. Experimentelle Untersuchung des laminar-turbulenten Umschlags an einer parallel angestroemten konkaven Wand. *Sitz. der Heidelberger Akad. Wiss. Math.-naturwiss. Klasse, Springer, Heidelberg*, 3:103–180, 1972.

[10] M. E. Brachet, M. Meneguzzi, H. Politano, and P. L. Sulem. The dynamics of freely decaying two-dimensional turbulence. *J. Fluid Mech.*, 194:333–349, 1988.

[11] H. J. Brauckmann and B. Eckhardt. Direct numerical simulations of local and global torque in Taylor–Couette flow up to Re= 30 000. *J. Fluid Mech.*, 718:398–427, 2013.

[12] G. L. Brown and A. Roshko. On density effects and large structure in turbulent mixing layers. *J. Fluid Mech.*, 64:775–816, 1974.

[13] S. L. Brunton and C. W. Rowley. Fast computation of finite-time Lyapunov exponent fields for unsteady flows. *Chaos*, 20:017503, 2010.

[14] A.-J. Buchner, D. Honnery, and J. Soria. Stability and three-dimensional evolution of a transitional dynamic stall vortex. *J. Fluid Mech.*, 823:166–197, 2017.

[15] M. J. Burin, H. Ji, E. Schartman, R. Cutler, P. Heitzenroeder, W. Liu, L. Morris, and S. Raftopolous. Reduction of Ekman circulation within Taylor-Couette flow. *Exp. Fluids*, 40:962–966, 2006.

[16] B. H. Carmichael. Low Reynolds number airfoil survey, volume 1. *NASA CR 165803*, 1981.

[17] K. Chauhan, J. Philip, and I. Marusic. Scaling of the turbulent/non-turbulent interface in boundary layers. *J. Fluid Mech.*, 751:298–328, 2014.

[18] D. D. Chin and D. Lentink. Flapping wing aerodynamics: from insects to vertebrates. *J. Exp. Biol.*, 219:920–932, 2016.

[19] M. S. Chong, A. E. Perry, and B. J. Cantwell. A general classification of three-dimensional flow fields. *Phys. Fluids*, 2:765–777, 1990.

[20] S. Corrsin and A. L. Kistler. Free-stream boundaries of turbulent flows. *NACA Report 1244*, 1955.

[21] C. Cossu and L. Brandt. Stabilization of Tollmien–Schlichting waves by finite amplitude optimal streaks in the Blasius boundary layer. *Phys. Fluids*, 14:L57–L60, 2002.

[22] W. R. Dean. Fluid motion in a curved channel. *Proc. R. Soc. Lond. A*, 121:402–420, 1928.

[23] P. W. Duck and M. R. Foster. Spin-up of homogeneous and stratified fluids. *Annu. Rev. Fluid Mech.*, 33:231–263, 2001.

[24] V. W. Ekman. On the influence of the earth's rotation on ocean currents. *Ark. Mat. Astron. Fys.*, 2:1–53, 1905.

[25] J. D. Eldredge and A. R. Jones. Leading-edge vortices: mechanics and modeling. *Annu. Rev. Fluid Mech.*, 51:75–104, 2019.

[26] A. Eslam Panah, J. M. Akkala, and J. H. J. Buchholz. Vorticity transport and the leading-edge vortex of a plunging airfoil. *Exp. Fluids*, 56:160, 2015.

[27] G.-A. Euteneuer. Störwellenlängen-Messung bei Längswirbeln in laminaren Grenzschichten an konkav gekrümmten Wänden. *Acta Mech.*, 7:161–168, 1969.

[28] G.-A. Euteneuer. Die Entwicklung von Längswirbeln in zeitlich anwachsenden Grenzschichten an konkaven Wänden. *Acta Mech.*, 13:215–223, 1972.

[29] N. Fabbiane. An innovative DNS code for high-Re turbulent pipe flow. Master's thesis, Politecnico di Milano, 12 2011. http://hdl.handle.net/10589/33202 (last accessed 2020-03-03).

[30] M. A. Fardin, C. Perge, and N. Taberlet. The hydrogen atom of fluid dynamics–introduction to the Taylor–Couette flow for soft matter scientists. *Soft Matter*, 10:3523–3535, 2014.

[31] J. N. Fernando and D. E. Rival. On vortex evolution in the wake of ax-isymmetric and non-axisymmetric low-aspect-ratio accelerating plates. *Phys. Fluids*, 28:017102, 2016.

[32] J. N. Fernando and D. E. Rival. Reynolds-number scaling of vortex pinch-off on low-aspect-ratio propulsors. *J. Fluid Mech.*, 799:R3, 2016.

[33] F. E. Fish and G. V. Lauder. Passive and active flow control by swim-ming fishes and mammals. *Annu. Rev. Fluid Mech.*, 38:193–224, 2006.

[34] J. J. M. Floryan and W. S. Saric. Stability of Görtler vortices in bound-ary layers. *AIAA J.*, 20:316–324, 1982.

[35] J. M. Floryan. On the Görtler instability of boundary layers. *Prog. Aerosp. Sci.*, 28:235–271, 1991.

[36] J. H. M. Fransson, L. Brandt, A. Talamelli, and C. Cossu. Experimental study of the stabilization of tollmien–schlichting waves by finite ampli-tude streaks. *Phys. Fluids*, 17:054110, 2005.

[37] M. Gazzola, M. Argentina, and L. Mahadevan. Scaling macroscopic aquatic locomotion. *Nat. Phys.*, 10:758–761, 2014.

[38] H. Görtler. Instabilität laminarer Grenzschichten an konkaven Wänden gegenüber gewissen dreidimensionalen Störungen. *Z. Angew. Math. Mech.*, 21:250–252, 1941.

[39] L. Graftieaux, M. Michard, and N. Grosjean. Combining PIV, POD and vortex identification algorithms for the study of unsteady turbulent swirling flows. *Meas. Sci. Technol.*, 12:1422–1429, 2001.

[40] K. O. Granlund, M. V. Ol, and L. P. Bernal. Unsteady pitching flat plates. *J. Fluid Mech.*, 733:R5, 2013.

[41] M. A. Green, C. W. Rowley, and G. Haller. Detection of lagrangian coherent structures in three-dimensional turbulence. *J. Fluid Mech.*, 572:111–120, 2007.

[42] S. Green. *Fluid vortices*. Kluwer Academic, Dordrecht, 1995.

[43] H. P. Greenspan and L. N. Howard. On a time-dependent motion of a rotating fluid. *J. Fluid Mech.*, 17:385–404, 1963.

[44] H. P. Greenspan and S. Weinbaum. On non-linear spin-up of a rotating fluid. *J. Math. Phys.*, 44:66–85, 1965.

[45] S. Grossmann, D. Lohse, and C. Sun. High–Reynolds number Taylor-Couette turbulence. *Annu. Rev. Fluid Mech.*, 48:53–80, 2016.

[46] P. Hall and N. J. Horseman. The linear inviscid secondary instability of longitudinal vortex structures in boundary layers. *J. Fluid Mech.*, 232:357–375, 1991.

[47] G. Haller. Lagrangian coherent structures. *Annu. Rev. Fluid Mech.*, 47:137–162, 2015.

[48] C. Hartloper and D. Rival. Vortex development on pitching plates with lunate and truncate planforms. *J. Fluid Mech.*, 732:332–344, 2013.

[49] H. Hertel. *Structure, form, movement*. Reinhold, New York, 1966.

[50] C.-M. Ho and P. Huerre. Perturbed free shear layers. *Annu. Rev. Fluid Mech.*, 16:365–422, 1984.

[51] P. H. Hoffmann, K. C. Muck, and P. Bradshaw. The effect of concave surface curvature on turbulent boundary layers. *J. Fluid Mech.*, 161:371–403, 1985.

[52] S. Hoyas and J. Jiménez. Reynolds number effects on the Reynolds-stress budgets in turbulent channels. *Phys. Fluids*, 20:101511, 2008.

[53] Y. Huang and M. A. Green. Detection and tracking of vortex phenomena using Lagrangian coherent structures. *Exp. Fluids*, 56:147, 2015.

[54] I. A. Hunt and P. N. Joubert. Effects of small streamline curvature on turbulent duct flow. *J. Fluid Mech.*, 91:633–659, 1979.

[55] J. C. R. Hunt, A. A. Wray, and P. Moin. Eddies, streams, and convergence zones in turbulent flows. *Proc. 1988 Summer Program Cent. Turbul. Res., Stanford*, pages 193–207, 1988.

[56] S. Ito. Aerodynamic influence of leading-edge serrations on an airfoil in a low Reynolds number. *J. Biomech. Sci. Eng.*, 4:117–123, 2009.

[57] J. Jeong and F. Hussain. On the identification of a vortex. *J. Fluid Mech.*, 285:69–94, 1995.

[58] J. Jiménez, S. Hoyas, M. P. Simens, and Y. Mizuno. Turbulent boundary layers and channels at moderate Reynolds numbers. *J. Fluid Mech.*, 657:335–360, 2010.

[59] L. C. Johansson and G. V. Lauder. Hydrodynamics of surface swimming in leopard frogs (rana pipiens). *J. Exp. Biol.*, 207:3945–3958, 2004.

[60] J. Kim, P. Moin, and R. Moser. Turbulence statistics in fully developed channel flow at low Reynolds number. *J. Fluid Mech.*, 177:133–166, 1987.

[61] M. C. Kim and C. K. Choi. The onset of Taylor–Görtler vortices during impulsive spin-down to rest. *Chem. Eng. Sci.*, 61:6478–6485, 2006.

[62] M. C. Kim, K. H. Song, and C. C. K. Energy stability analysis for impulsively decelerating swirl flows. *Phys. Fluids*, 20:064101, 2008.

[63] O. Kitoh. Experimental study of turbulent swirling flow in a straight pipe. *J. Fluid Mech.*, 225:445–479, 1991.

[64] N. H. Kling, J. Kriegseis, L. Opfer, and P. Rogler. Pressure evaluation of spray-induced flow in the framework of a statistical approach based on urans and ensemble averaging. *Meas. Sci. Technol.*, 30:084004, 2019.

[65] R. C. Kloosterziel and G. J. F. Van Heijst. An experimental study of unstable barotropic vortices in a rotating fluid. *J. Fluid Mech.*, 223:1–24, 1991.

[66] M. Kozul, D. Chung, and J. P. Monty. Direct numerical simulation of the incompressible temporally developing turbulent boundary layer. *J. Fluid Mech.*, 796:437–472, 2016.

[67] D. P. Lathrop, J. Fineberg, and H. L. Swinney. Transition to shear-driven turbulence in Couette-Taylor flow. *Phys. Review A*, 46:6390–6405, 1992.

[68] R. R. Leknys, M. Arjomandi, R. M. Kelso, and C. H. Birzer. Leading-edge vortex development on a pitching flat plate with multiple leading edge geometries. *Exp. Therm. Fluid*, 96:406–418, 2018.

[69] S. K. Lele. Compact finite difference schemes with spectral-like resolution. *J. Comput. Phys.*, 103:16–42, 1992.

[70] D. Lentink and M. H. Dickinson. Rotational accelerations stabilize leading edge vortices on revolving fly wings. *J. Exp. Biol.*, 212:2705–2719, 2009.

[71] H. Lewis and P. Bellan. Physical constraints on the coefficients of fourier expansions in cylindrical coordinates. *J. Math. Phys.*, 31:2592–2596, 1990.

[72] F. Li and M. R. Malik. Fundamental and subharmonic secondary instabilities of Görtler vortices. *J. Fluid Mech.*, 297:77–100, 1995.

[73] M. J. Lighthill. Boundary layer theory. In *Laminar Boundary Layers (ed. L. Rosenhead)*, pages 46–103. Oxford Univ. Press, Oxford, 1963.

[74] C. C. Lin. *The theory of hydrodynamic stability*. Cambridge Univ. Press, Cambridge, 1955.

[75] J. C. Lin. Review of research on low-profile vortex generators to control boundary-layer separation. *Prog. Aerosp. Sci.*, 38:389–420, 2002.

[76] P. F. Linden and G. J. F. Van Heijst. Two-layer spin-up and frontogenesis. *J. Fluid Mech.*, 143:69–94, 1984.

[77] W. W. Liou. Linear instability of curved free shear layers. *Phys. Fluids*, 6:541–549, 1994.

[78] P. B. S. Lissaman. Low-Reynolds-number airfoils. *Annu. Rev. Fluid Mech.*, 15:223–239, 1983.

[79] J. M. Lopez. Flow between a stationary and a rotating disk shrouded by a co-rotating cylinder. *Phys. Fluids*, 8:2605–2613, 1996.

[80] J. M. Lopez and P. D. Weidman. Stability of stationary endwall boundary layers during spin-down. *J. Fluid Mech*, 326:373–398, 1996.

[81] P. Luchini and A. Bottaro. Linear stability and receptivity analyses of the Stokes layer produced by an impulsively started plate. *Phys. Fluids*, 13:1668–1678, 2001.

[82] L. R. M. Maas. Nonlinear and free-surface effects on the spin-down of barotropic axisymmetric vortices. *J. Fluid Mech.*, 246:117–141, 1993.

[83] N. N. Mansour and P. Kim, J.and Moin. Reynolds-stress and dissipation-rate budgets in a turbulent channel flow. *J. Fluid Mech.*, 194:15–44, 1988.

[84] P. S. Marcus. Simulation of Taylor-Couette flow. part 2. numerical results for wavy-vortex flow with one travelling wave. *J. Fluid Mech.*, 146:65–113, 1984.

[85] L. Mascotelli. Direct numerical simulations of a turbulent pipe flow at high reynolds numbers. Master's thesis, Politecnico di Milano, 7 2016. http://hdl.handle.net/10589/123696 (last accessed 2020-03-03).

[86] D. M. Mathis and G. P. Neitzel. Experiments on impulsive spin-down to rest. *Phys. Fluids*, 28:449–454, 1985.

[87] T. Maxworthy. A simple observational technique for the investigation of boundary layer stability and turbulence. *Turb. Meas. in Liquids*, pages 32–37, 1971. Dept. Chem. Engineering, Univ. of Missouri-Rolla.

[88] T. Maxworthy. The structure and stability of vortex rings. *J. Fluid Mech.*, 51:15–32, 1972.

[89] T. Maxworthy. Some experimental studies of vortex rings. *J. Fluid Mech.*, 81:465–495, 1977.

[90] D. C. McCormick and J. C. Bennett. Vortical and turbulent structure of a lobed mixer free shear layer. *AIAA J.*, 32:1852–1859, 1994.

[91] C. J. McPhaden and D. E. Rival. Unsteady force estimation using a lagrangian drift-volume approach. *Exp. Fluids*, 59:64, 2018.

[92] R. N. Meroney and P. Bradshaw. Turbulent boundary-layer growth over a longitudinally curved surface. *AIAA J.*, 13:1448–1453, 1975.

[93] A. Michalke. On spatially growing disturbances in an inviscid shear layer. *Journal of Fluid Mechanics*, 23:521–544, 1965.

[94] B. R. Morton. The generation and decay of vorticity. *Geophys. Astrophys. Fluid Dyn.*, 28:277–308, 1984.

[95] R. D. Moser and P. Moin. The effects of curvature in wall-bounded turbulent flows. *J. Fluid Mech.*, 175:479–510, 1987.

[96] G. P. Neitzel. Marginal stability of impulsively initiated Couette flow and spin-decay. *Phys. Fluids*, 25:226–232, 1982.

[97] G. P. Neitzel and S. H. Davis. Centrifugal instabilities during spin-down to rest in finite cylinders. Numerical experiments. *J. Fluid Mech.*, 102:329–352, 1981.

[98] J. O'Donnell and P. F. Linden. Free-surface effects on the spin-up of fluid in a rotating cylinder. *J. Fluid Mech*, 232:439–453, 1991.

[99] J. O'Donnell and P. F. Linden. Spin-up of a two-layer fluid in a rotating cylinder. *Geophys. Astrophys. Fluid Dyn.*, 66:47–66, 1992.

151

[100] R. Ostilla-Mónico, R. J. A. M. Stevens, S. Grossmann, R. Verzicco, and D. Lohse. Optimal Taylor–Couette flow: direct numerical simulations. *J. Fluid Mech.*, 719:14–46, 2013.

[101] R. Ostilla-Mónico, R. Verzicco, S. Grossmann, and D. Lohse. The near-wall region of highly turbulent Taylor–Görtler flow. *J. Fluid Mech.*, 788:95–117, 2016.

[102] R. Ostilla-Mónico, Z. X., V. Spandan, R. Verzicco, and D. Lohse. Life stages of wall-bounded decay of Taylor–Görtler turbulence. *Phys. Rev. Fluids*, 2:114601, 2017.

[103] R. L. Panton. Scaling laws for the angular momentum of a completely turbulent couette flow. *C. R. Acad. Sci. Paris*, 2:1467–1473, 1991.

[104] J. Pedlosky. The spin up of a stratified fluid. *J. Fluid Mech*, 28:463–479, 1967.

[105] C. P. Pitt Ford and H. Babinsky. Lift and the leading-edge vortex. *J. Fluid Mech.*, 720:280–313, 2013.

[106] M. Raffel, J. Kompenhans, S. T. Wereley, and C. Willert. *Particle image velocimetry: a practical guide*. Springer, Heidelberg, 2007.

[107] L. Rayleigh. On the dynamics of revolving fluids. *Proc. R. Soc. Lond. A*, 93:148–154, 1917.

[108] J. Ren and S. Fu. Secondary instabilities of Görtler vortices in high-speed boundary layer flows. *J. Fluid Mech.*, 781:388–421, 2015.

[109] D. E. Rival, J. Kriegseis, P. Schaub, A. Widmann, and C. Tropea. Characteristic length scales for vortex detachment on plunging profiles with varying leading-edge geometry. *Exp. Fluids*, 55:1660, 2014.

[110] G. A. Rosi and D. E. Rival. Entrainment and topology of accelerating shear layers. *J. Fluid Mech.*, 811:37–50, 2017.

[111] G. A. Rosi and D. E. Rival. A Lagrangian perspective towards studying entrainment. *Exp. Fluids*, 59:19, 2018.

[112] W. S. Saric. Görtler vortices. *Annu. Rev. Fluid Mech.*, 26:379–409, 1994.

[113] Ö. Savaş. Stability of bödewadt flow. *J. Fluid Mech.*, 183:77–94, 1987.

[114] A. Savitzky and M. J. E. Golay. Smoothing and differentiation of data by simplified least squares procedures. *Anal. Chem.*, 36:1627–1639, 1964.

[115] E. K. Sawyer, E. C. Turner, and J. H. Kaas. Somatosensory brainstem, thalamus, and cortex of the california sea lion (zalophus californianus). *J. Comp. Neurol.*, 524:1957–1975, 2016.

[116] K. Schaal, A. Bauer, P. Chandrashekar, R. Pakmor, C. Klingenberg, and V. Springel. Astrophysical hydrodynamics with a high-order discontinuous galerkin scheme and adaptive mesh refinement. *Mon. Not. R. Astron. Soc*, 453:4278–4300, 2015.

[117] P. Schlatter, E. Deusebio, R. de Lange, and L. Brandt. Numerical study of the stabilisation of boundary-layer disturbances by finite amplitude streaks. *Intl J. Flow Control*, 2:259–288, 2010.

[118] P. Schlatter, R. Örlü, Q. Li, G. Brethouwer, J. H. M. Fransson, A. V. Johansson, P. H. Alfredsson, and D. S. Henningson. Turbulent boundary layers up to re θ= 2500 studied through simulation and experiment. *Phys. Fluids*, 21:051702, 2009.

[119] H. Schlichting. *Boundary Layer Theory*. McGraw-Hill, New York, 1979.

[120] L. U. Schrader, L. Brandt, and T. A. Zaki. Receptivity, instability and breakdown of Görtler flow. *J. Fluid Mech.*, 682:362–396, 2011.

[121] A. Sescu and M. Z. Afsar. Hampering Görtler vortices via optimal control in the framework of nonlinear boundary region equations. *J. Fluid Mech.*, 848:5–41, 2018.

[122] S. C. Shadden, F. Lekien, and J. E. Marsden. Definition and properties of Lagrangian coherent structures from finite-time Lyapunov exponents in two-dimensional aperiodic flows. *Physica D*, 212:271–304, 2005.

[123] J. A. Sillero, J. Jiménez, and R. D. Moser. One-point statistics for turbulent wall-bounded flows at reynolds numbers up to $\delta+\approx$ 2000. *Phys. Fluids*, 25:105102, 2013.

[124] D. Sipp and L. Jacquin. Three-dimensional centrifugal-type instabilities of two-dimensional flows in rotating systems. *Phys. Fluids*, 12:1740–1748, 2000.

[125] J. H. Spurk. *Fluid mechanics*. Springer, Heidelberg, 1997.

[126] J. D. Swearingen and R. F. Blackwelder. The growth and breakdown of streamwise vortices in the presence of a wall. *J. Fluid Mech.*, 182:255–290, 1987.

[127] K. Taira and T. Colonius. Three-dimensional flows around low-aspect-ratio flat-plate wings at low reynolds numbers. *J. Fluid Mech.*, 623:187–207, 2009.

[128] G. I. Taylor. Stability of a viscous liquid contained between two rotating cylinders. *Phil. Trans. R. Soc. Lond. A*, 223:289–334, 1923.

[129] G. K. Taylor, R. L. Nudds, and A. L. R. Thomas. Flying and swimming animals cruise at a strouhal number tuned for high power efficiency. *Nature*, 425:707–711, 2003.

[130] V. L. Thurmond, R. W. Potter II, and M. A. Clynne. The densities of saturated solutions of nacl and kcl from 10 degrees to 105 degrees c. Technical report, US Geological Survey, 1984.

[131] M. S. Triantafyllou, G. S. Triantafyllou, and R. Gopalkrishnan. Wake mechanics for thrust generation in oscillating foils. *Phys. Fluids*, 3:2835–2837, 1991.

[132] J. R. Usherwood and C. P. Ellington. The aerodynamics of revolving wings I. model hawkmoth wings. *J. Exp. Biol.*, 205:1547–1564, 2002.

[133] G. Venezian. Nonlinear spin-up. *Topics in ocean engineering*, 2:87–96, 1970.

[134] R. A. Verschoof, S. G. Huisman, R. C. A. van der Veen, C. Sun, and D. Lohse. Self-similar decay of high Reynolds number Taylor–Couette turbulence. *Phys. Rev. Fluids*, 1:062402, 2016.

[135] R. A. Verschoof, A. K. te Nijenhuis, S. G. Huisman, C. Sun, and D. Lohse. Periodically driven Taylor–Couette turbulence. *J. Fluid Mech.*, 846:834–845, 2018.

[136] U. T. von Bödewadt. Die Drehströmung über festem Grunde. *J. Appl. Math. Mech*, 20:241–253, 1940.

[137] E. H. Wedemeyer. The unsteady flow within a spinning cylinder. *J. Fluid Mech*, 20:383–399, 1964.

[138] P. D. Weidman. On the spin-up and spin-down of a rotating fluid. Part 1. Extending the Wedemeyer model. *J. Fluid Mech*, 77:685–708, 1976.

[139] M. Wolf, M. Holzner, B. Lüthi, D. Krug, W. Kinzelbach, and A. Tsinober. Effects of mean shear on the local turbulent entrainment process. *J. Fluid Mech.*, 731:95–116, 2013.

[140] J. G. Wong, J. Kriegseis, and D. E. Rival. An investigation into vortex growth and stabilization for two-dimensional plunging and flapping plates with varying sweep. *J. Fluids Struct.*, 43:231–243, 2013.

[141] J. G. Wong and D. E. Rival. Determining the relative stability of leading-edge vortices on nominally two-dimensional flapping profiles. *J. Fluid Mech.*, 766:611–625, 2015.

[142] J. G. Wong, G. A. Rosi, A. Rouhi, and D. E. Rival. Coupling temporal and spatial gradient information in high-density unstructured Lagrangian measurements. *Exp. Fluids*, 58:140, 2017.

[143] X. Wu and P. Moin. Direct numerical simulation of turbulence in a nominally zero-pressure-gradient flat-plate boundary layer. *J. Fluid Mech.*, 630:5–41, 2009.

[144] X. Wu, D. Zhao, and J. Luo. Excitation of steady and unsteady Görtler vortices by free-stream vortical disturbances. *J. Fluid Mech.*, 682:66–100, 2011.

[145] Y. Zhang, K. Liu, H. Xian, and X. Du. A review of methods for vortex identification in hydroturbines. *Renew. Sus. Energ. Rev.*, 81:1269–1285, 2018.

Publications
and Conference Contributions

[Kaiser et al., 2020a] Kaiser, F., Frohnapfel, B., Kriegseis, J., Ostilla-Monico, R., Rival, D. E., and Gatti, D. (2020a). On the stages of vortex decay in an impulsively-stopped, rotating cylinder. *Journal of Fluid Mechanics*. A6.

[Kaiser et al., 2019] Kaiser, F., Galler, J., Kriegseis, J., and Rival, D. E. (2019). Force estimates in turbulent vortex wakes of accelerating propulsors: The effects of edge undulation on vortex formation. In *The 13th International Symposium on Particle Image Velocimetry, Munich, Germany*.

[Kaiser et al., 2018] Kaiser, F., Kriegseis, J., and Rival, D. E. (2018). Scaling of vorticity annihilation during leading-edge vortex formation. In *QUBS – Conference on bio-propulsion of adaptive systems, Kingston, Canada*.

[Kaiser et al., 2020b] Kaiser, F., Kriegseis, J., and Rival, D. E. (2020b). The influence of edge undulation on vortex formation for low-aspect-ratio propulsors. *Journal of Fluid Mechanics*. A55.

[Kaiser et al., 2017] Kaiser, F., von der Burg, M., Viboud, S., Sommeria, J., Rival, D. E., and Kriegseis, J. (2017). High reynolds number measurements of vorticity generation and annihilation with rapidly changing boundary conditions. In *The 12th International Symposium on Particle Image Velocimetry, Busan, Korea*.

[Kaiser et al., 2016] Kaiser, F., Wahl, T., Gatti, D., Rival, D. E., and Kriegseis, J. (2016). Vorticity propagation for spin-up and spin-down in a rotating tank. In *18th International Symposium on the Application of Laser and Imaging Techniques to Fluid Mechanics, Lisbon, Portugal*.

[von der Burg et al., 2017] von der Burg, M., Kaiser, F., Gatti, D., Schmidt, B., Sommeria, J., Viboud, S., Rival, D., and J., K. (2017). Boundary layer characterization during impulsive spin-up and spin-down motions of high-reynolds number rotating flow. In *25. Fachtagung Lasermethoden in der Strömungsmesstechnik, Karlsruhe, Germany*. 25.

Student works

[Oßw18] Moritz Oßwald. *Experimental Investigation of Centrifugal Instabilities in then Near-Wall Region.* Bachelor's Thesis, 2018.

[Pel17] Seyedeh Pegah Pelasaeedi. *A Framework for Assessing Statistically Unsteady Turbulence in Rotating Cylinders.* Master's Thesis, 2017.

[Sch17] Björn Schmidt. *Reduktion des Einflusses der Ekman-Grenzschicht in beschleunigten rotierenden Systemen".* Bachelor's Thesis, 2017.

[vdB17] Malte von der Burg. *Acceleration of Curved Walls in Rotating Systems - An Instability Analysis.* Master's Thesis, 2017.

[Wah16] Tobias Wahl. *Propagation and Annihilation of Vorticity – Spin-up and Spin-down of a Rotating Tank.* Master's Thesis, 2016.

Nomenclature

All indices used (i,j,k...) run from $1 - 3$. The superscript * indicates that the quantity is scaled to be dimensionless. The superscripts $\langle . \rangle$ and $'$ used with flow quantities indicate the spatial average and the fluctuation, respectively. The superscripts $[.]$ describes the volume average. The superscript $^+$ marks quantities scaled in plus units.

Latin letters – Upper case

SYMBOL	SI UNIT	DESCRIPTION
A		aspect ratio
A_{back}	m^2	surface area of the back plate
A_{front}	m^2	surface area of the front plate
A_g	m^2	area where Γ_1 or Γ_2 is evaluated
A_p	m^2	cross section of the plate
B		ratio between shear layer thickness and edge undulation
C		Cauchy-Green tensor
C_d		drag coefficient
D	m	diameter
E	$\mathrm{m}^2\,\mathrm{s}^{-1}$	symmetric part of ∇u

Ek		Ekman number
Eu		Euler number
F_v	$\mathrm{kg\,m\,s^{-1}}$	force due to change in vortex momentum
F_o	$\mathrm{kg\,m\,s^{-1}}$	force due to change of momentum of fluid outside the vortex
F_z	$\mathrm{kg\,m\,s^{-1}}$	force due to a change of momentum in axial direction
F_p	$\mathrm{kg\,m\,s^{-1}}$	force estimated by surface pressures
Fr		Froude number
Fr_s		modified Froude number
Fr_s^c		critical modified Froude number
G	$\mathrm{kg\,m\,s^{-2}}$	body force
H	m	filling height of the cylinder
H_m	m	measurement height
H_s	m	filling height of salt water
H_s^{min}	m	minimum required filling height of salt water
I_v	$\mathrm{kg\,m\,s^{-1}}$	momentum of the vortex
I_o	$\mathrm{kg\,m\,s^{-1}}$	momentum of fluid outside vortex
I_z	$\mathrm{kg\,m\,s^{-1}}$	momentum in axial direction
K	$\mathrm{m^2\,s^{-2}}$	mean kinetic energy
K_{ran}	$\mathrm{m^2\,s^{-2}}$	kinetic energy distribution in Rankine vortex
K_{lam}	$\mathrm{m^2\,s^{-2}}$	mean kinetic energy of laminar solution
K_0	$\mathrm{m^2\,s^{-2}}$	mean kinetic energy at $t = 0$
L_{cyl}	m	cylinder length

L_0	m	characteristic length
L	m	length scale of propulsor
M		coefficient of logarithmic law
N		coefficient of logarithmic law
N_i		resolution in i-direction
P	$\mathrm{m^2\,s^{-3}}$	production of k
$P_0 - P_\infty$	$\mathrm{kg\,s^{-2}\,m^{-1}}$	reference pressure difference
P_p	m	perimeter of the plate
Q	$\mathrm{s^{-1}}$	Q-criterion
R	m	radius
R_c	m	radius of vortex core
R_{hs}	m	radial position of the HS camera
$\mathscr{R}$	$\mathrm{m^{-1}}$	local curvature
Re		Reynolds number
Re_{cor}		corrected Reynolds number
Re_p		plate Reynolds number
Re_τ		friction Reynolds number
Ro		Rossby number
St		Strouhal number
Ta		Taylor number
Ta_c		critical Taylor number
T_w	°C	water temperature
T_m	$\mathrm{m^2\,s^{-3}}$	turbulent transport of K
T_t	$\mathrm{m^2\,s^{-3}}$	turbulent transport of k

T_{int}	s	integration time of FTLE
T_0	s	characteristic time
U_0	$\mathrm{m\,s^{-1}}$	characteristic velocity
U_∞	$\mathrm{m\,s^{-1}}$	free-stream velocity
V_m	$\mathrm{m^2\,s^{-3}}$	viscous transport of K
V_t	$\mathrm{m^2\,s^{-3}}$	viscous transport of k
V	$\mathrm{m^3}$	volume
V_δ	$\mathrm{m^3}$	volume of the boundary layer
V_s	$\mathrm{m^3}$	salt-water volume

Latin letters – Lower case

SYMBOL	SI UNIT	DESCRIPTION
a	m	amplitude
a_{lam}		coefficient for laminar growth rate of the boundary layer
a_{turb}		coefficient for turbulent growth rate of the boundary layer
b	m	reference vector for Lagrangian description
d	m	equivalent vortex-core diameter
d_z	m	vortex-core diameter based on peak azimuthal velocities
d_p	m	particle diameter
f	$\mathrm{s^{-1}}$	frequency
$f_{[K]}^{III}$		logarithmic decay law for K
$f_{[K]}^{V}$		exponential decay law for K

$f_{[k]}^{III}$		exponential decay law for k
$g_{[K]}$		coefficient of logarithmic decay law for K
$h_{[K]}$		coefficient of logarithmic decay law for K
$g_{[k]}$		coefficient of logarithmic decay law for k
$h_{[k]}$		coefficient of logarithmic decay law for k
k	$\mathrm{m^2\,s^{-2}}$	turbulent kinetic energy
k_p	$\mathrm{m^{-1}}$	wavenumber of plate's edge undulations
k_0	$\mathrm{m^2\,s^{-2}}$	turbulent kinetic energy at $t = 0$
l	$\mathrm{m^2\,s^{-1}}$	angular momentum
n_p		number of plate's edge undulations
u	s	velocity vector
u_i	s	velocity vector component in i-direction
u_φ^{ran}	$\mathrm{m\,s^{-1}}$	azimuthal velocity in a Rankine vortex
u_φ^{lam}	$\mathrm{m\,s^{-1}}$	laminar azimuthal velocity profile during spin-down
u_φ^{rel}	$\mathrm{m\,s^{-1}}$	relative azimuthal velocity of fluid towards platform
u_τ	$\mathrm{m\,s^{-1}}$	friction velocity
p	$\mathrm{kg\,m^{-1}\,s^{-2}}$	pressure
p_w	$\mathrm{kg\,m^{-1}\,s^{-2}}$	pressure in water layer
p_{int}	$\mathrm{kg\,m^{-1}\,s^{-2}}$	pressure at the interface
p_{ran}	$\mathrm{kg\,m^{-1}\,s^{-2}}$	pressure distribution in Rankine vortex
p_{SBR}	$\mathrm{kg\,m^{-1}\,s^{-2}}$	pressure distribution in SBR
r	m	radial coordinate

r_c	m	radial position of the vortex core
z_c	m	axial position of the vortex core
s	m	travelled distance
t	s	time
t_c	s	critical time
t_o	s	onset time
t_o^{cor}		corrected onset time
t_{avg}	s	time span over which the a moving average is calculated
t_E	s	time scale of Ekman pumping
t_D	s	time scale of side-wall boundary layer
t_{SD}	s	spin-down time of platform
w	m	streamwise direction
x	m	position in space
x_m	m	center of area used for Γ_1 and Γ_2
y	m	wall-normal coordinate
z	m	axial coordinate
z_I	m	height in two-phase flow cylinder
z_{II}	m	height in two-phase flow cylinder
z_{III}	m	height in two-phase flow cylinder
z_{int}	m	height in two-phase flow interface

Greek letters – Upper case

SYMBOL	SI UNIT	DESCRIPTION
Γ	$\mathrm{m^2\,s^{-1}}$	circulation
Γ_c	$\mathrm{m^2\,s^{-1}}$	vortex-core circulation
Γ_1	$\mathrm{m^2\,s^{-1}}$	Galilean variant Graftieaux criterion
Γ_2	$\mathrm{m^2\,s^{-1}}$	Galilean invariant Graftieaux criterion
$\dot{\Gamma}_{sl}$	$\mathrm{m^2\,s^{-2}}$	flux of circulation into the vortex due to the shear layer
$\Delta\ldots$		spacing of $(\ldots)$
ΔT	s	time shift of turbulent towards laminar solution
Λ_{max}		maximum Eigenvalue of C
Ω	$\mathrm{s^{-1}}$	angular speed of the cylinder/platform
Ω_R	$\mathrm{s^{-1}}$	symmetric part of ∇u
Ω_C	$\mathrm{s^{-1}}$	angular speed of a rotating coordinate system
$\Phi_{u_i u_i}$	$\mathrm{m^3\,s^{-2}}$	axial energy spectra
Π^d	$\mathrm{m^2\,s^{-3}}$	pressure diffusion of k
Ξ	$\mathrm{m^2\,s^{-3}}$	sum of production and dissipation of k

Greek letters – Lower case

SYMBOL	SI UNIT	DESCRIPTION
δ	m	shear-layer thickness
δ_c	m	critical boundary-layer thickness
δ_{99}	m	boundary-layer thickness
ϵ_m	$\mathrm{m^2\,s^{-3}}$	dissipation of K

ϵ_t	$\mathrm{m^2\,s^{-3}}$	dissipation of k
ϵ_{tot}	$\mathrm{m^2\,s^{-3}}$	dissipation of kinetic energy
κ_c	$\mathrm{m^{-1}}$	wavenumber of critical mode
κ_δ	$\mathrm{m^{-1}}$	wavenumber of boundary-layer thickness
κ_z	$\mathrm{m^{-1}}$	wavenumber of axial modes
λ	m	wavelength
λ_c	m	critical wavelength
λ_T	m	currently dominating wavelength
μ	$\mathrm{kg\,m^{-1}\,s^{-1}}$	dynamic viscosity
ν	$\mathrm{m^2\,s^{-1}}$	kinematic viscosity
φ		angular coordinate
ρ	$\mathrm{kg\,m^{-3}}$	density
ρ_p	$\mathrm{kg\,m^{-3}}$	density of particles
ρ_s	$\mathrm{kg\,m^{-3}}$	density of salt water solution
ρ_w	$\mathrm{kg\,m^{-3}}$	density of water
$\sigma_{T_{int}}^b$	$\mathrm{s^{-1}}$	FTLE
τ_w	$\mathrm{kg\,m^{-1}\,s^{-2}}$	wall shear stress
θ		normalised (viscous) time
θ_c		normalised critical time
θ_o		normalised onset time
θ_v		normalised visual onset time
θ_{fit}		normalised fit to estimate onset time
θ_o^{cor}		normalised corrected onset time
θ_{SD}		normalised spin-down time

θ_{i-iii}		time instances at which cases $(i), (ii)$ or (iii) are measured
ξ_{ii}	$\mathrm{m^3\,s^{-2}}$	one-dimensional spectrum
ω	$\mathrm{s^{-1}}$	vorticity vector
ω_i	$\mathrm{s^{-1}}$	vorticity component in i-direction

Mathematical operators

SYMBOL	DESCRIPTION
$A(\dots)$	integrated temporal evolution of $(\dots)$
$\partial(\dots)$	partial derivative
$\frac{\mathrm{D}\dots)}{\mathrm{D}t}$	material derivative
∇	Nabla operator
$\int\int(\dots)\mathrm{d}A$	surface integral
$\int\int\int(\dots)\mathrm{d}V$	surface integral
$\mathfrak{R}$	real part of complex number

Abbreviations

Symbol	Description
DNS	direct numerical simulation
FOV	field of view
FTLE	Finite-time Lyapunov exponent
f.p.s.	frames per second
KHI	Kelvin-Helmholtz instabilities
LCS	Lagrangian coherent structures
LEV	leading-edge vortex
NBC	Neumann boundary conditions
PIV	particle image velocimetry
SBR	solid-body rotation
TC	Taylor-Couette flow
TS	Tollmien-Schlichting
TNTI	Turbulent-non turbulent interface
VFE	Vortex-forming edge

List of Figures

List of Tables

A Detailed derivation of equations

This appendix includes the extended derivations of various equations used throughout this manuscript and mainly in chapter 3. Pelasaeedi [Pel17] contributed to the derivation of the following equations during her Master Thesis.

A.1 Incompressible Navier-Stokes equations: cylindrical coordinates

For an incompressible flow, the continuity equation is given in Section 2.1 by (2.2)

$$\nabla u = 0,$$

which expressed in cylindrical coordinates is equal to

$$\frac{1}{r}\frac{\partial (r u_r)}{\partial r} + \frac{1}{r}\frac{\partial u_\varphi}{\partial \varphi} + \frac{\partial u_z}{\partial z}. \tag{A.1}$$

The momentum equations are given by (2.3)

$$\rho \underbrace{\left[\frac{\partial u}{\partial t} + (u \cdot \nabla)u\right]}_{\text{I}} = - \underbrace{\nabla p}_{\text{II}} + \underbrace{\mu \nabla^2 u}_{\text{III}} + \underbrace{\rho G}_{\text{IV}},$$

where I is the material derivative consisting of the temporal velocity change $\frac{\partial u}{\partial t}$ and the convection $(u \cdot \nabla)u$, II is the gradient of the pressure p, III are the viscous forces acting in the Newtonian fluid and IV is a body force G (e.g. gravity). Dividing by ρ and expanding the equation into cylindrical coordi-

nates leads to the following equations:

radial direction

$$
\frac{\partial u_r}{\partial t} + u_r \frac{\partial u_r}{\partial r} + \frac{u_\varphi}{r} \frac{\partial u_r}{\partial \varphi} - \frac{u_\varphi^2}{r} + u_z \frac{\partial u_r}{\partial z} =
$$
$$
- \frac{1}{\rho} \frac{\partial p}{\partial r} + \nu \left[\frac{1}{r} \frac{\partial}{\partial r} \left(r \frac{\partial u_r}{\partial r} \right) + \frac{1}{r^2} \frac{\partial^2 u_r}{\partial \varphi^2} + \frac{\partial^2 u_r}{\partial z^2} - \frac{u_r}{r^2} - \frac{2}{r^2} \frac{\partial u_\varphi}{\partial \varphi} \right] + G_r
$$

(A.2)

azimuthal direction

$$
\frac{\partial u_\varphi}{\partial t} + u_r \frac{\partial u_\varphi}{\partial r} + \frac{u_\varphi}{r} \frac{\partial u_\varphi}{\partial \varphi} + \frac{u_r u_\varphi}{r} + u_z \frac{\partial u_\varphi}{\partial z} =
$$
$$
- \frac{1}{\rho r} \frac{\partial p}{\partial \varphi} + \nu \left[\frac{1}{r} \frac{\partial}{\partial r} \left(r \frac{\partial u_\varphi}{\partial r} \right) + \frac{1}{r^2} \frac{\partial^2 u_\varphi}{\partial \varphi^2} + \frac{\partial^2 u_\varphi}{\partial z^2} - \frac{u_\varphi}{r^2} + \frac{2}{r^2} \frac{\partial u_r}{\partial \varphi} \right] + G_\varphi
$$

(A.3)

axial direction

$$
\frac{\partial u_z}{\partial t} + u_r \frac{\partial u_z}{\partial r} + \frac{u_\varphi}{r} \frac{\partial u_z}{\partial \varphi} + u_z \frac{\partial u_z}{\partial z} =
$$
$$
- \frac{1}{\rho} \frac{\partial p}{\partial z} + \nu \left[\frac{1}{r} \frac{\partial}{\partial r} \left(r \frac{\partial u_z}{\partial r} \right) + \frac{1}{r^2} \frac{\partial^2 u_z}{\partial \varphi^2} + \frac{\partial^2 u_z}{\partial z^2} \right] + G_z
$$

(A.4)

A.2 Reynolds decomposition and simplifications

Statistical analysis of the transitional flow is performed by means of spatial averaging. The spin-down discussed in chapter 3 is statistically homogeneous in axial and azimuthal direction. Thus, the decomposition

$$
u_i(r, \varphi, z, t) = \langle u_i \rangle_{\varphi, z}(r, t) + u_i'(r, \varphi, z, t), \tag{A.5}
$$

is applied in the following, where i is the direction in cylindrical coordinates (r, φ, z) and $\langle . \rangle_{\varphi, z}$ the spatial average in axial and azimuthal direction. In the following, the simplified notation $\langle u_i \rangle = \langle u_i \rangle_{\varphi, z}(r, t)$ and $u_i' = u_i'(r, \varphi, z, t)$ is ap-

plied. the In addition to the Reynolds decomposition, numerous features of the flow at hand are utilised in the following simplifications of transport equations:

a) no radial mean flow: $\langle u_r \rangle = 0$;

b) no axial mean flow: $\langle u_z \rangle = 0$;

c) statistical homogeneity in azimuthal direction: $\frac{\partial \langle . \rangle}{\partial \varphi} = 0$;

d) statistical homogeneity in axial direction: $\frac{\partial \langle . \rangle}{\partial z} = 0$;

e) features of averaging: $\langle \langle u_i \rangle u_i' \rangle = 0$ and $\langle u_i' \rangle = 0$.

A.2.1 Reynolds averaged Navier-Stokes equation: Azimuthal direction

In the following the momentum equation in azimuthal direction is simplified by means of the Reynolds decomposition and subsequent simplifications. Neglecting the body force G and rewriting the convective term of (A.3) leads to

$$
\begin{aligned}
&\frac{\partial u_\varphi}{\partial t} + \frac{\partial (u_r u_\varphi)}{\partial r} - u_\varphi \frac{\partial u_r}{\partial r} + \frac{1}{r} \frac{\partial (u_\varphi u_\varphi)}{\partial \varphi} \\
&- \frac{1}{r} u_\varphi \frac{\partial u_\varphi}{\partial \varphi} + \frac{u_r u_\varphi}{r} + \frac{\partial (u_x u_\varphi)}{\partial x} - u_\varphi \frac{\partial u_x}{\partial x} = \\
&- \frac{1}{r\rho} \frac{\partial p}{\partial \varphi} + \nu \left[\frac{1}{r} \frac{\partial}{\partial r} \left(r \frac{\partial u_\varphi}{\partial r} \right) + \frac{1}{r^2} \frac{\partial^2 u_\varphi}{\partial \varphi^2} + \frac{\partial^2 u_\varphi}{\partial x^2} - \frac{u_\varphi}{r^2} + \frac{2}{r^2} \frac{\partial u_r}{\partial \varphi} \right] \quad .
\end{aligned}
$$

$$(A.6)$$

The equation is expanded by adding and subtracting the term $\dfrac{u_\varphi u_r}{r}$, which allows to separate and eliminate the terms of the continuity equation (2.2)

$$
\frac{\partial u_\varphi}{\partial t} + \frac{\partial (u_r u_\varphi)}{\partial r} + \frac{1}{r}\frac{\partial (u_\varphi u_\varphi)}{\partial \varphi} + \frac{u_r u_\varphi}{r} + \frac{\partial (u_z u_\varphi)}{\partial z}
$$

$$
- u_\varphi \underbrace{\left(\frac{\partial u_r}{\partial r} + \frac{1}{r}\frac{\partial u_\varphi}{\partial \varphi} + \frac{\partial u_z}{\partial z} + \frac{u_r}{r} \right)}_{=0} + \frac{u_r u_\varphi}{r} =
$$

$$
- \frac{1}{r\rho}\frac{\partial p}{\partial \varphi} + \nu \left[\frac{1}{r}\frac{\partial}{\partial r}\left(r\frac{\partial u_\varphi}{\partial r} \right) + \frac{1}{r^2}\frac{\partial^2 u_\varphi}{\partial \varphi^2} + \frac{\partial^2 u_\varphi}{\partial z^2} - \frac{u_\varphi}{r^2} + \frac{2}{r^2}\frac{\partial u_r}{\partial \varphi} \right] \quad .
$$

$$
(A.7)
$$

Applying the Reynolds decomposition and simplifications a)-e) leads to

$$
\frac{\partial \langle u_\varphi \rangle}{\partial t} + \frac{\partial \left(\langle u_r' u_\varphi' \rangle \right)}{\partial r} + 2\frac{\langle u_r' u_\varphi' \rangle}{r} = \nu \left[\frac{1}{r}\frac{\partial}{\partial r}\left(r\frac{\partial \langle u_\varphi \rangle}{\partial r} \right) - \frac{\langle u_\varphi \rangle}{r^2} \right] \quad . \quad (A.8)
$$

A.3 Mean kinetic energy

The mean kinetic energy K is given by

$$
K = \frac{1}{2}\left(\langle u_r \rangle^2 + \langle u_\varphi \rangle^2 + \langle u_z \rangle^2 \right) = \frac{1}{2}\langle u_\varphi \rangle^2 \qquad (A.9)
$$

Its temporal derivative can be expressed as

$$
\frac{\partial K}{\partial t} = \frac{1}{2}\frac{\partial \langle u_\varphi \rangle^2}{\partial t} = \langle u_\varphi \rangle \frac{\partial \langle u_\varphi \rangle}{\partial t}, \qquad (A.10)
$$

where $\frac{\partial \langle u_\varphi \rangle}{\partial t}$ can be rewritten using (A.8). This yields the following budget (see (3.2)):

$$\frac{\partial K}{\partial t} = \underbrace{-\frac{\partial}{\partial r}\left(\langle u_\varphi \rangle \langle u_r' u_\varphi' \rangle\right) - \frac{\langle u_\varphi \rangle \langle u_r' u_\varphi' \rangle}{r}}_{T_m} + \underbrace{\frac{\partial}{\partial r}\left(\nu \langle u_\varphi \rangle \frac{\partial \langle u_\varphi \rangle}{\partial r}\right) + \frac{\nu}{2r}\frac{\partial \langle u_\varphi \rangle^2}{\partial r}}_{V_m} \cdots$$

$$\cdots + \underbrace{\langle u_r' u_\varphi' \rangle \left(\frac{\partial \langle u_\varphi \rangle}{\partial r} - \frac{\langle u_\varphi \rangle}{r}\right)}_{P} - \underbrace{\nu \left(\frac{\partial \langle u_\varphi \rangle}{\partial r}\right)^2 - \nu \frac{\langle u_\varphi \rangle^2}{r^2}}_{\epsilon_m}. \quad \text{(A.11)}$$

The turbulent transport terms of K are gathered in T_m. Fluctuations carry K from one radial position to another. In contrast, the viscous transport V_m does not include any fluctuations u_i'.

A.4 Vorticity transport equation

The vorticity transport equation can is derived by application of curl onto the momentum equation (2.3), leading to

$$\nabla \times \left[\frac{\partial u}{\partial t} + (u \cdot \nabla)u\right] = -\frac{1}{\rho}\nabla \times \nabla p + \nu \nabla \times \nabla^2 u + \nabla \times G. \quad \text{(A.12)}$$

For conservative body forces G with a potential $\mathfrak{G}$ ($G = \nabla \mathfrak{G}$) and incompressible fluids body forces as well as the pressure term immediately vanish as

$$\nabla \times \nabla \mathfrak{E} = 0 \quad \text{(A.13)}$$

where $\mathfrak{E}$ is an arbitrary scalar field. The convective term of the momentum equation can be expressed with the vector identity

$$(u \cdot \nabla)u = \nabla \left(\frac{1}{2}u \cdot u\right) - u \times \omega. \quad \text{(A.14)}$$

181

When the curl is applied, the first term on the right hand side can be neglected as $\nabla \times \nabla \left(\frac{1}{2} u \cdot u \right)$; see (A.13). The remaining terms are again rewritten as

$$\nabla \times (u \times \omega) = \underbrace{-\omega(\nabla \cdot u)}_{=0 \text{ as } (\nabla \cdot u)=0} +(\omega \cdot \nabla)u - (u \cdot \nabla)\omega. \tag{A.15}$$

Due to Youngs theorem, the viscous term simplifies to

$$\nu \nabla \times \nabla^2 u = \nu \nabla^2 (\nabla \times u) = \nu \nabla^2 \omega, \tag{A.16}$$

All terms combined, provide the vorticity transport equation (2.14)

$$\underbrace{\frac{\partial \omega}{\partial t}}_{I} + \underbrace{(u \cdot \nabla)\omega}_{II} = \underbrace{(\omega \cdot \nabla)u}_{III} + \underbrace{\nu \nabla^2 \omega}_{IV}$$

where I is the temporal change, II is the convection, III accounts for stretching and reorientation of vorticity and IV describes the diffusion of vorticity.

B   Boundary-layer scaling in stage III

For stage III, section 3.5.3 presents collapsing azimuthal velocity profiles $\langle u_\varphi^+ \rangle$ in the near-wall region and collapsing normalised angular momentum profiles l^+ in the vorticity-free region for $Re = 12\,000$. This appendix supplements the profiles by the data of the simulations with $Re \in \{3000, 6000, 28\,000\}$. Also here the profiles collapse. However, the constants M and N of the logarithmic fit as well as l^+ are a function of Re. A scaling law for l^+ is suggested in section 3.6.5.

(a) Mean velocity profile $\langle u_\varphi^+ \rangle$ presented in the form of the law of the wall. Dotted lines indicate the relationship $\langle u_\varphi^+ \rangle = y^+$ and (3.15).

(b) Angular momentum $l^+ = \langle u_\varphi^+ \rangle (r/R)$ in wall units. The dash-dotted vertical line marks the wall-normal distance up to which the angular momentum l^+ is approximately constant.
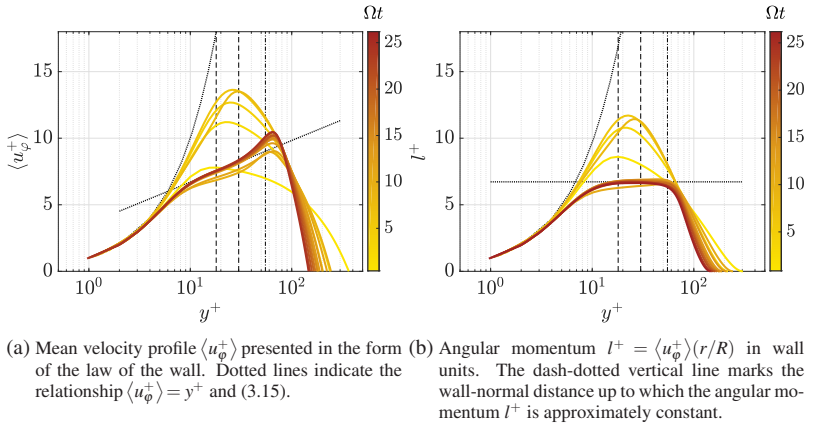
Figure B.1: Two vertical dashed lines enclose the region of approximately logarithmic behaviour of $\langle u_\varphi^+ \rangle$. Results refer to the spin-down process at $Re = 3000$. Figure adapted from [Kaiser et al., 2020a].

(a) Mean velocity profile $\langle u_\varphi^+ \rangle$

(b) Angular momentum $l^+ = \langle u_\varphi^+ \rangle (r/R)$
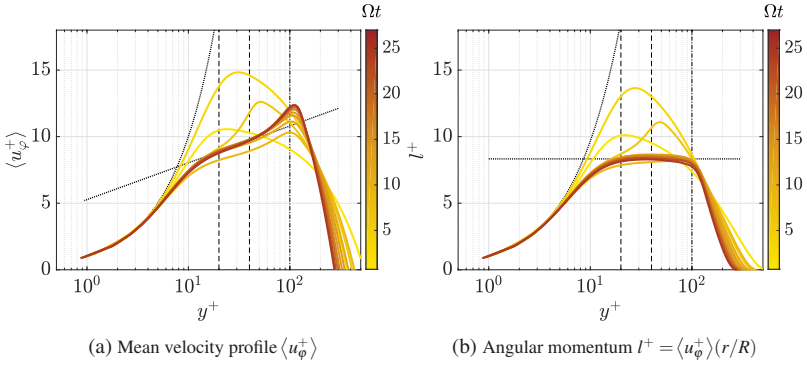
Figure B.2: Results refer to the spin-down process at $Re = 6000$. See figure B.1 fur detailed subcaptions. Figure adapted from [Kaiser et al., 2020a].

(a) Mean velocity profile $\langle u_\varphi^+ \rangle$

(b) Angular momentum $l^+ = \langle u_\varphi^+ \rangle (r/R)$
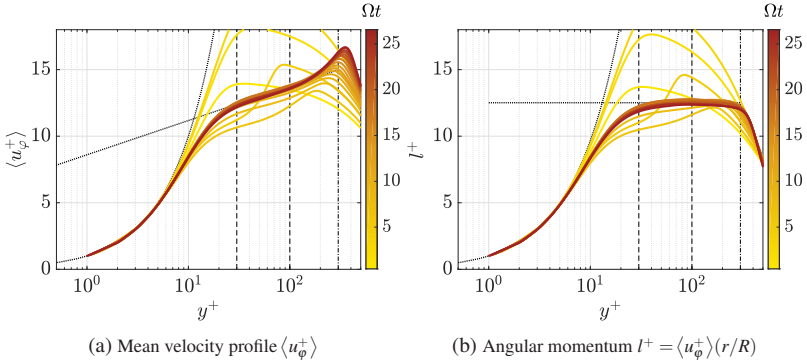
Figure B.3: Results refer to the spin-down process at $Re = 28\,000$. See figure B.1 fur detailed subcaptions. Figure adapted from [Kaiser et al., 2020a].

Acknowledgements

only help me to sharpen the scientific questions answered in this manuscript, but also taught me a lot about turbulence, budget equations and instabilities.

Thank you to the members of the workshop Siegfried Häcker, Heiko Bendler, Marcel Stotz, Kai Franzke, and Otto Vorreiter for their excellent work over the years.

In addition, I want to express a special thanks to my colleagues Andrea Codrignani, Andreas Güttler, Anna Daub, Alexander Stroh, Daniel Klauber, Erik Hansen, Franco Magagnato, Georg Fahland, Giacomo Cocconi, Kay Schäfer, Karin Fritsch-Kirchner, Marc Hehner, Nils Kling, Lars von Deyn, Pourya Forooghi, Sibela Hasecic, Tobias Schumm, Robin Leister and Verena Fink. I could list many of you as co-supervisors but more importantly I can list all of you as friends. The working environment at ISTM was incredible and this was mainly because of you.

This thesis would not have been possible without the contributions of my students Björn Schmidt, Nico Große, Malte von der Burg, Michael Laier, Moritz Oßwald, Seyedeh Pegah Pelasaeedi, Tobias Wahl and Tom Renner. I learned a lot working alongside you and I hope you can say the same.

On a final note, I want to express my gratitude towards my friends and family. I could not be more lucky. To my always curious parents Hiltraut and Martin, who have never stopped reading and learning and who keep on trying to teach me what really is important in life; to my siblings Anne, Jonas, and Ruth with their wonderful families; and to my second family Christine, Henning, Konstantin, Charlotte, and Friederike: Thank you for all the support and love you gave me!